Localised Variation of Magnetic Properties of Grain Oriented Electrical Steels

by

Xin Tong Xu

A thesis submitted to the Cardiff University in candidature for

the degree of Doctor of Philosophy

Wolfson Centre for Magnetics
Cardiff School of Engineering
Cardiff University

July 2014

DECLARATION

This work has not previously been accepted in substance for any degree and is not concurrently submitted in candidature for any degree.

Signed……………………………………….(candidate)   Date …………………………………..

STATEMENT 1

This thesis is being submitted in partial fulfillment of the requirements for the degree of PhD.

Signed……………………………………….(candidate)   Date …………………………………………

STATEMENT 2

This thesis is the result of my own independent work/investigation, except where otherwise stated. Other sources are acknowledged by explicit references.

Signed……………………………………….(candidate)   Date …………………………………………

STATEMENT 3

I hereby give consent for my thesis, if accepted, to be available for photocopying and for inter-library loan, and for the title and summary to be made available to outside organisations.

Signed…………………………………….…(candidate)   Date …………………………………..

Acknowledgements

Summary

Localised magnetic flux density, magnetising field and power loss are believed to distribute non-uniformly in grain oriented electrical steel. Understanding of the causes of their variation can help reduce the overall power loss of the material.

In this investigation, magnetic domain observation was often used in the study of domain configuration and crystal orientation of the test specimens. Methods of domain observation have been studied and compared in order to select the appropriate method for different parts of the investigation and to improve the understanding of the image observed.

A less destructive local loss measurement sensor has been built for the measurement of localised flux density, magnetising field and power loss. The sensor was tested and evaluated specifically for the measurement of localised magnetic power loss of the high permeability grain oriented electrical steel.

The results obtained from local loss scanning measurements indicated that localised flux density and magnetising field can vary substantially in grain oriented electrical steel under AC magnetisation of 50 Hz. The variation of localised flux density has been found mainly resulted by grain misorientation and local grain arrangement. The transverse component of flux density was detected and has been found increases with increasing grain misorientation. The variation of localised magnetising field has been found mainly influenced by the localised demagnetising field due to formation of free magnetic poles at grain boundaries. It has been proved that both flux density and magnetising field have strong influence on the distribution of localised power loss.

The study of the effect of domain refinement on distribution of localised flux density showed that domain refinement by means of ball scribing on one surface of grain oriented electrical steel can improve the uniformity of distribution of flux density. However, results also inferred that excessive scribing in a confined area can cause obvious uneven distribution of flux density in the direction of the specimen's thickness.

List of Contents

Chapter 1

Introduction

Grain oriented electrical steel is commonly used in power transformers and high performance rotating electrical machines; it is highly valuable product in electrical power industries. In the over 100 year's history of electrical steel, steel manufacturers have achieved outstanding improvement on magnetic properties of the steel. However, the power loss occurring in the material during magnetisation can be as much as 5% of all electrical power generated [1.1]. Therefore, the demand for better understanding of the causes of power loss grows accordingly.

Grain oriented electrical steel has a polycrystalline structure with a preferred crystal orientation; such a texture provides low power loss when the steel is magnetised along its rolling direction. However, it has been reported [1.2-1.8] that the variation of localised magnetic properties within the polycrystalline structure can cause increased total power loss.

The study of local magnetic field, magnetic flux density and power loss variation is essential for understanding the factors that contribute to power loss. Development of a reliable method for measurement of local magnetic properties is crucial for the investigation.

Considering the demand for greater understanding of effect of localised variation of magnetic properties on power loss, the main objectives of the investigation are set as follows:

- To study magnetic domain observation techniques and to compare domain images obtained on the surface of grain oriented electrical steel using these techniques.

- To develop a system for measurement of localised flux density, magnetising field and power loss of grain oriented electrical steel.

- To measure localised flux density, magnetising field and power loss and to determine factors that lead to their variation.

- To investigate the effect of domain refinement on distribution of localised magnetic flux density.

References

[1.1] A. J. Moses, "Characterisation of the Loss behaviour in electrical steels and other soft magnetic materials", Proceedings of Workshop on Metallurgy and Magnetism, Freiberg, Germany, (2004).

[1.2] K. J. Overshott and M. G. Blundell, "Power loss, domain wall motion and flux density of neighbouring grains in grain-oriented 3% silicon-iron". IEEE Transactions on Magnetics, vol. mag-20, pp. 1551 – 1553, (1984).

[1.3] S. Tumanski, "The application of permalloy magnetoresistive sensors for non-destructive testing of electrical steel sheets". Journal of Magnetism and Magnetic Materials, vol. 75, pp. 266 – 272, (1988).

[1.4] A. J. Moghaddam and A. J. Moses, "A non-destructive automated method of localised power loss measurement in grain oriented 3% silicon iron", Journal of Magnetism and Magnetic Materials, vol. 112, pp. 132 – 134, (1992).

[1.5] S. Tumanski and T. Winek, "Measurements of the local values of electrical steel parameters", Journal of Magnetism and Magnetic Materials, vol. 174, pp. 185 – 191, (1997).

[1.6] M. Enokizono, I. Tanabe and T. Kubota, "Localised distribution of two-dimensional magnetic properties and magnetic domain observation", Journal of Magnetism and Magnetic Materials, vol. 196 – 197, pp. 338 – 340, (1999).

[1.7] K. Senda, M. Kurosawa, M. Ishida, M. Komatsubara and T. Yamaguchi, "Local magnetic properties in grain-oriented electrical steel measured by the modified needle probe method", Journal of Magnetism and Magnetic Materials, vol. 215 – 216, pp. 136 – 139, (2000).

[1.8] K. Tone, H. Shimoji, S. Urata, M. Enokizono and T. Todaka, "Magnetic characteristic analysis considering the crystal grain of grain-oriented electrical steel sheet", IEEE Transactions on Magnetics, vol. 41, pp. 1704 – 1707, (2005).

Chapter 2

Introduction to Ferromagnetism and Grain Oriented Electrical Steels

2.1 Basic terms in magnetism

A magnetic field **H** is a region where magnetic material will experience a force; it can be produced by either electric currents or magnetic poles [2.1]. The response to the field in the medium is called magnetic induction **B**, also sometimes called magnetic flux density [2.2]. It exists in all media whenever there is a magnetic field. The effective permeability **μ** of a medium is used to link B and H. Thus, their relationship is expressed as

$$B = \mu H \tag{2.1}$$

where B has units of Tesla (T), H has units of Ampere per meter (A/m) and μ is measured in Henry per meter (H/m). If the media is free space, equation (2.1) can be written as

$$B = \mu_0 H \tag{2.2}$$

where $\mu_0 = 4\pi \times 10^{-7}$ H/m is the permeability of free space. For any other media, equation (2.1) can be written as

$$B = \mu_0 \mu_r H \qquad\qquad (2.3)$$

where μ_r is the relative permeability (dimensionless); it is the ratio of effective permeability μ to the permeability of free space μ_0, i.e.,

$$\mu = \mu_0 \mu_r \qquad\qquad (2.4)$$

According to the range of value of μ_r, magnetic materials are mainly classified into paramagnetic, diamagnetic, anti-ferromagnetic, ferromagnetic and ferrimagnetic. Ferromagnetic are those with μ_r much higher than unity. Thus, they have a far wider range of applications than the other classes. In addition, for paramagnetic and diamagnetic materials μ_r is constant over a substantial range of applied H. For ferromagnetic material, μ_r varies significantly with the applied H due to the hysteretic behaviour which is discussed in section 2.2. Typical μ_r values of some materials are shown in table 2.1.

Classification	Material	Relative Permeability μ_r
Paramagnetic	Air	1.000 000 37
Diamagnetic	Copper	0.999 990 00
Anti-ferromagentic	Ferrite (manganese zinc)	640
Ferromagnetic	Grain oriented electrical steel	2 000 (H=800 A/m)
Ferrimagnetic	Magnetite (e.g. Fe_3O4)	4

Table 2.1 Classification of magnetism [2.3].

2.2 Ferromagnetic materials and magnetism

Ferromagnetic materials, such as Ni, Fe, Co and some of their alloys, as mentioned in section 2.1, have very large μ_r. They are formed by regions of aligned atomic dipoles, even with no external magnetic field presence. The generation of atomic dipoles in ferromagnetic materials is explained by the band theory.

Electron spin in atoms may have energy level (band), and each energy level in an atom can contain a maximum of two electrons, and they must have opposite spin (spin up or spin down). Atoms in ferromagnetic materials have unfilled 3d energy level, thus leaving unpaired electrons in this level which gives them magnetic dipoles [2.1].

Regions of the aligned atomic dipoles are called magnetic domains, and are illustrated in figure 2.1. The domain theory was first proposed by Weiss in 1906, and later, Bitter confirmed their existence through observation. He observed domain patterns on a ferromagnetic material using fine iron powders under an optical microscope (see chapter 4). As displayed in figure 2.1, atomic dipoles are aligned parallel in domains where the magnetisation is saturated. The narrow region where the transformation of dipole alignment takes place is called a domain wall. The width of the domain wall depends on the equilibrium of exchange and anisotropy energy. For iron, the width of a 180° domain wall is approximately 160 lattice parameters or 46 nm [2.2].
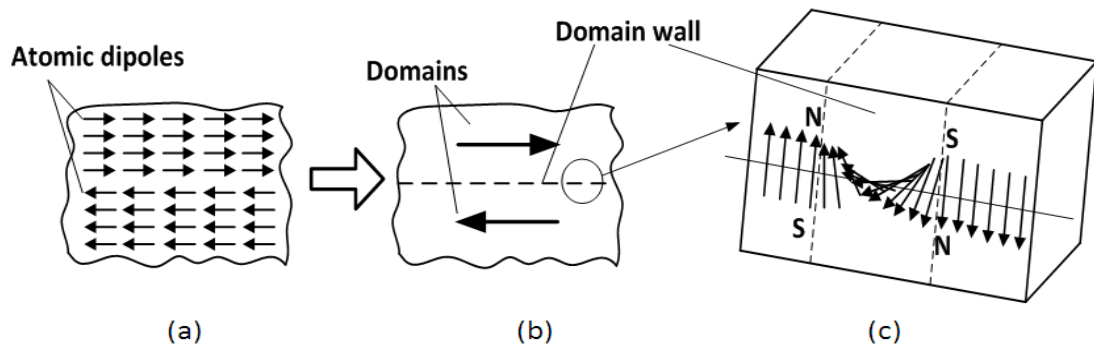
Figure 2.1 Illustration of the theory of magnetic domain (a) atomic dipoles are lined up to form domains, (b) domains with arrows inside them showing the direction of overall magnetisation and the domain wall which separates them, and (c) arrows showing the rotation of magnetisation at the domain wall [2.4].

In general, domain walls are categorised as **Bloch** walls and **Néel** walls according to the rotation of the dipoles. Figure 2.2 demonstrates how magnetisation rotates in the Bloch and Néel walls, and their definitions are given as:

Bloch wall - rotation of magnetisation is parallel to the wall plane; this type of domain wall is more energetically favourable since the path of rotation is along the crystal easy axis.

Néel wall - plane of rotation of magnetisation is perpendicular to the wall plane; the rotation is less energetically favourable and this type of domain wall usually exists in thin films with applied external magnetic field.

Néel walls commonly occur in thin film materials; most ferromagnetic materials (e.g. FeSi steel) contain only Bloch walls.
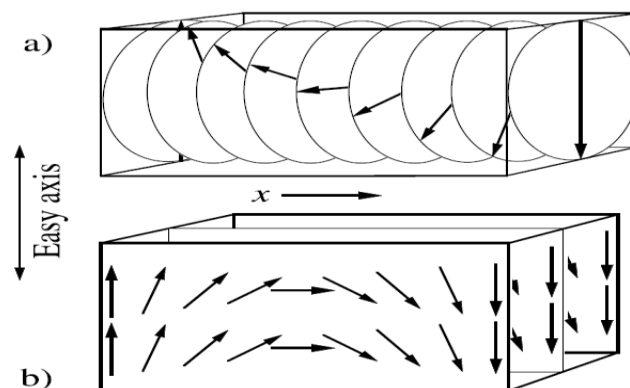
Figure 2.2 Illustration of rotation of magnetisation in (a) Bloch wall and (b) Néel wall [2.5].

Domains exist and arrange themselves to minimise the overall magnetic energy E, which can be divided into the following energy terms:

$$E = E_D + E_\lambda + E_{ex} + E_k + E_z \qquad (2.5)$$

Where,

E_D is Magnetostatic energy, which is the energy associated with the leakage field extending outside the domain.

E_λ is Magnetoelastic anisotropy energy, this is the energy associated with elastic strains in lattice caused by magnetostriction the magnetic phenomenon describing the slight change in material dimensions when magnetised.

E_{ex} is Exchange energy, which is the energy related to exchange interaction between magnetic dipoles; the energy is minimized when all dipoles are pointing in the same direction.

E_k is Magnetocrystalline anisotropy energy, which is the energy associated with easy and hard magnetisation direction of a magnetically anisotropy material; this energy is minimised when material is magnetized along its easy axis. For iron, this easy and hard axis is described at later context of this section.

E_z is Zeeman energy, which is the energy associated with the externally applied magnetic field; this energy is minimised when magnetisation of domains are parallel to the applied field.

Consider a ferromagnetic material containing only a single domain as seen in figure 2.3 (a). Atomic dipoles are lined up inside the materials and free poles form on the ends, this creates leakage field and increases magnetostatic energy. This energy can be reduced if the single domain splits into two domains as illustrated in figure 2.3 (b). Further reduction is possible by continuing domain division as illustrated in figure 2.3 (c). However, the process cannot carry on indefinitely since the exchange energy increases as domain walls are added. Therefore, energy minimisation accomplished by forming flux-closure domains on the ends as illustrated in (d) and zero magnetostatic energy is achieved since flux follows the closed path within the material.
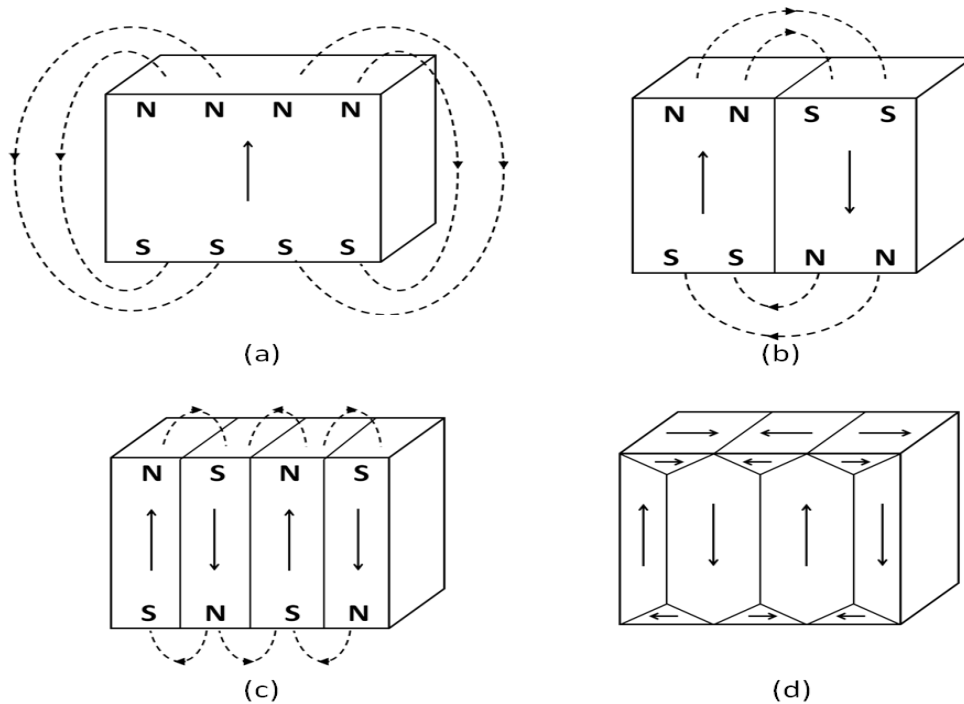
Figure 2.3 Illustration of division into magnetic domains.

For iron and silicon iron, walls between the anti-parallel domains are known as 180° domain walls, and walls between 180° domains and flux-closure domains are known as 90° walls.

Magnetisation **M** (A/m) indicates the alignment of magnetic dipoles in a given direction. When no external field is applied to a ferromagnetic material, complete saturation magnetisation **M$_0$** occurs at 0 K (-273°C). M reduces with increasing temperature because thermal energy distorts the alignment of diploes. The alignment of the dipoles disappears completely at the Curie temperature **T$_c$**, and the material becomes paramagnetic. The complete saturation magnetisation and the Curie temperature of basic ferromagnetic materials are shown in Table 2.2.

Material	M$_0$ (10^6 A/m)	T$_c$ (°C)
Iron	1.71	770
Cobalt	1.42	1130
Nickel	0.48	358

Table 2.2 Magnetisation and Curie temperature of ferromagnetic materials.

In most ferromagnetic materials, magnetisation M at room temperature is not much lower than the complete saturation magnetisation M_0, so saturation magnetisation M_s can be measured at room temperature.

In a magnetic material, as illustrated in figure 2.3 (a), the self-produced magnetic field H due to the formation of free poles is called the demagnetising field $\mathbf{H_d}$, M and H_d point in opposite directions inside the material. The strength of the demagnetising field depends on M and the material shape [2.2] and can be expressed as

$$H_d = -N_d M \tag{2.6}$$

where N_d is the demagnetising factor, which is related to sample geometry (E.g. for sphere N_d is ~ 0.3, for a thin plate with field perpendicular to surface N_d is ~ 0.9 and for a thin plate with field parallel to surface N_d is ~ 0.1). If an external field H_{app} is applied, the self-produced demagnetising field acts against the magnetisation M. Therefore, the resulting field inside the sample H_{in} is given by

$$H_{in} = H_{app} - N_d M \tag{2.7}$$

Both H and M contribute to the magnetic induction B. In free space, M is zero, and $B = \mu_0 H$. M in ferromagnetic materials is given by $\mu_0 M$, where the term $\mu_0 M$ is called the magnetic polarisation $\mathbf{J}$ (T). The magnetic induction B can be expressed as

$$B = \mu_0 H + \mu_0 M = \mu_0 (H + M) \tag{2.8}$$

The ratio between M and H is the magnetic susceptibility χ, which indicates the level of a material response to an applied field. χ is expressed as

$$\chi = \frac{M}{H} = \mu_r - 1 \tag{2.9}$$

For ferromagnetic materials, values of magnetic permeability μ and susceptibility χ vary according to the magnitude of the applied external field; they can be obtained from a B-H loop which is shown in figure 2.4.

If an external alternating field H is applied to a ferromagnetic material which is completely demagnetised so that the domains configure themselves to achieve the minimum energy stage (position **a** in figure 2.4), B increases as the domains respond to the changing field and is represented by equation 2.7. At a lower field, domains start to reconfigure by creating magnetostatic energy (the energy which associates with the demagnetising field) which counterbalances the external field. As a result, domains with dipole alignment near the field grow, and domains with opposite dipole alignment shrink (position **b**). At a higher field, dipole alignment switching occurs in the flux-closure domains (including other less energetically favourable domains), where dipoles will switch to the direction of the easy axis which is the preferred crystallographic axis (discussed in detail in figure 2.5 in section 2.3). Now the material contains only a single domain as dipoles inside it are all pointing along the easy axis, this is the one closest to the field direction (position **c**). At an even higher field where positive saturation magnetisation M_s is reached, the field energy overcomes the crystal anisotropy energy, leading to the rotation of dipoles in the domain to align along the field direction (position **d**).
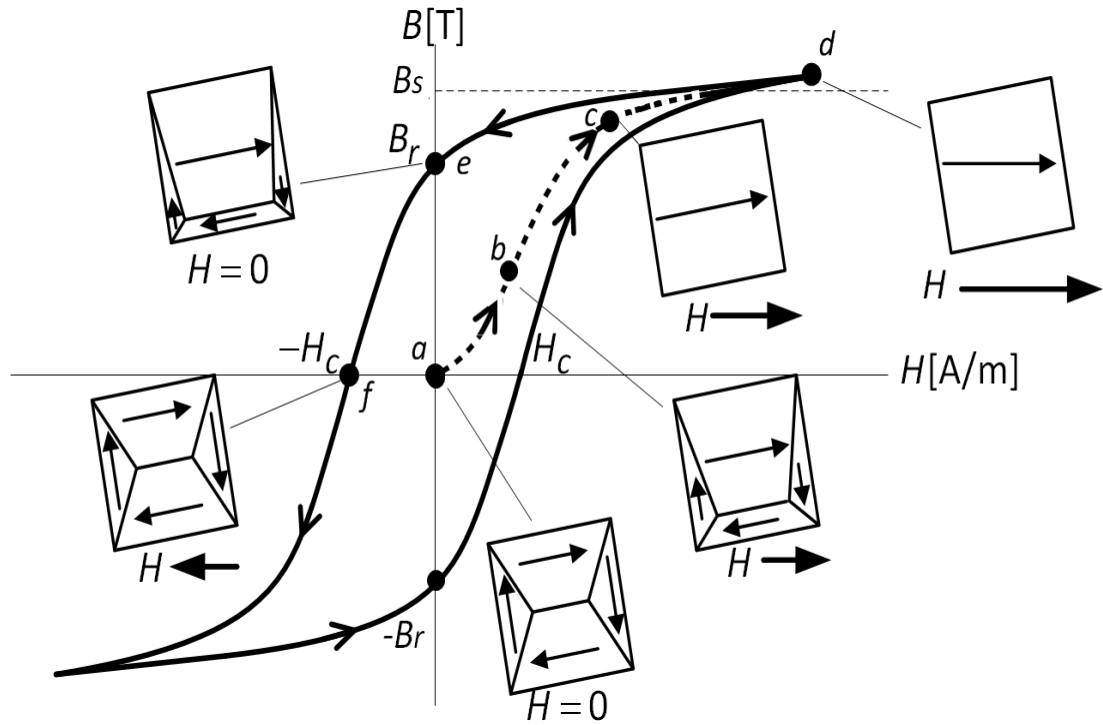
Figure 2.4 Domain process during a cycle of the ferromagnetic material [2.4].

Further increase of the external field will only lead to a slow increase in magnetic induction due to contribution of air flux ($\mu_0 H$) and a further alignment of imperfectly aligned dipoles caused by thermal activation energy. As a consequence, μ_r approaches unity. The process a-b-c-d is the initial magnetisation, and the dashed line is the initial magnetisation curve.

When the field is reduced to zero, magnetic induction drops to the remanence flux density **B$_r$** (position **e**), and the corresponding magnetisation is called remanence magnetisation **M$_r$**. This demonstrates the two characteristics when a ferromagnetic material is demagnetised, the **irreversible initial magnetisation** process and the remaining **residual magnetisation** after the removal of the applied external field. They are caused by domain wall pinning at obstacles, such as dislocations and precipitates [2.6][2.7]. To demagnetise a specimen, an additional and opposite field must be applied. The field that cancels the residual magnetisation is the coercive force **-H$_c$**. Further increase in the opposed field leads to negative saturation magnetisation. On reversing the field towards positive

saturation, the magnetising path passes the position **-B$_r$** and **H$_c$** on the x and y axis. This process repeats under the alternating field, and the enclosed loop is called the B – H loop or the hysteresis loop if the magnetising frequency of the external field is extremely low.

The area of the B–H loop is proportional to the energy dissipated in the material per magnetising cycle. Under a.c. magnetisation, the loop becomes frequency dependent, because additional energy losses can be added to the loop by rate-dependent eddy current losses and excess losses (discussed in detail in section 2.4).

Cubic crystalline material, for example iron, has magnetocrystalline anisotropy. This is sometimes referred to crystal anisotropy, which means that the material will consume less energy and be easier to magnetise in certain directions than in others. Therefore, it is important to know the crystallographic axis/axes that can give the easiest magnetisation. For iron, the easy magnetising axes are <100> family directions, and figure 2.5 shows the energy required to magnetise iron along the easy axis and two other important crystallographic axes. A low magnetising field is needed to reach M$_s$ when magnetising iron along its easy axis.
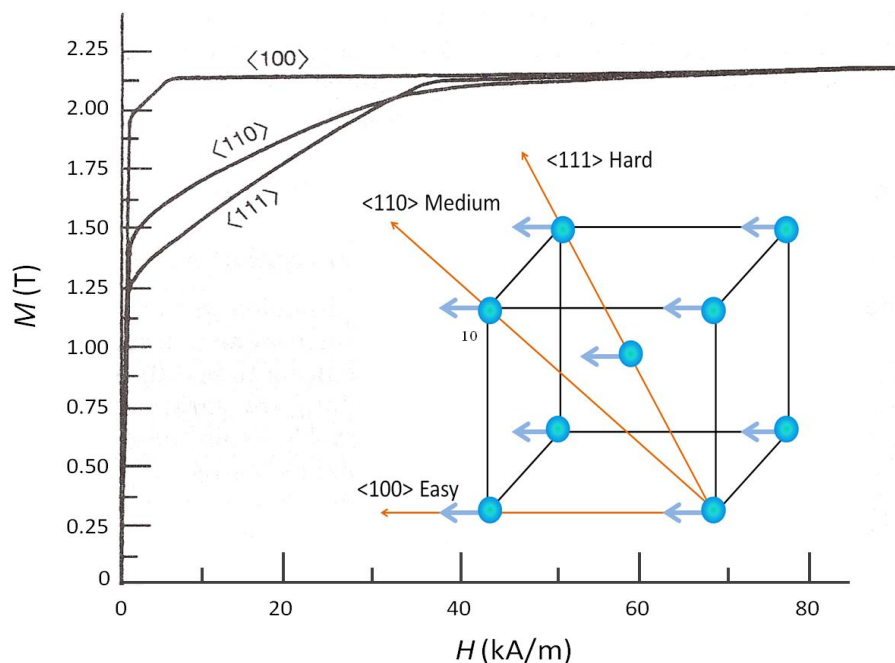
Figure 2.5 Magnetisation curve for the body centred iron [2.8].

As discussed in the domain process in an external field, dipole alignment switching occurs when the sample is magnetised from position b towards position c (figure 2.4), because the external field energy overcomes the crystal anisotropy force. The energy associated with the work done by the field is the **crystal anisotropy energy**. This can be calculated from equation 2.9 [2.9], from which the crystal easy axis can be determined for iron. For cubic crystals, the crystal anisotropy energy K_a is expressed as

$$E_a = K_1(a_1^2 a_2^2 + a_2^2 a_3^2 + a_3^2 a_1^2) + K_2 a_1^2 a_2^2 a_3^2 + K_3(a_1^2 a_2^2 + a_2^2 a_3^2 + a_3^2 a_1^2)^2 + ..., \qquad (2.10)$$

where a_1, a_2 and a_3 are the directional cosines of the magnetisation vector with respect to the three cube edges [100], [010] and [001], K_1, K_2 and K_3 are the magnetocrystalline anisotropy constants. Both α and K are dimensionless quantities. For iron, K_3 and further terms can be neglected since their values are much less than K_1. Table 2.3 shows how the easy, intermediate and hard magnetising axes are determined from anisotropy constants. For iron and iron silicon alloy, $K_1 > 0$ and $-9 < K_2/K_1 < \infty$, so that <100> becomes easy axis [2.10].

Anisotropy constants		Easy	Moderate	Hard
When K₁>0, $x = \dfrac{K_2}{K_1}$	$-\infty < x < -9$	<111>	<100>	<110>
	$-9 < x < -9/4$	<100>	<111>	<110>
	$-9/4 < x < +\infty$	<100>	<110>	<111>
When K₁<0 $x = \dfrac{K_2}{K_1}$	$-\infty < x < -9$	<111>	<110>	<100>
	$-9 < x < -9/4$	<110>	<111>	<100>
	$-9/4 < x < +\infty$	<110>	<100>	<111>

Table 2.3 Cubic crystal material anisotropy constants and the corresponding easy, moderate and hard magnetising axes [2.10].

2.3   Properties and production of grain oriented electrical steels

Grain-oriented electrical steel is an iron silicon alloy mostly used for assembling transformer cores. The steel is specially fabricated to have low power

loss (small B – H area) and high permeability. In addition, small amounts of silicon are added usually around 3 wt% for lower eddy current loss (see chapter 2.4) by increasing the electrical resistivity of the material.

Grain oriented steel is made in thin sheets (typical gauge 0.23 – 0.30 mm) containing grains (typical diameter 5 – 10 mm) which have a similar crystal orientation as shown in figure 2.6. Goss [2.11] in 1934 found that arranging the crystals easy axis (110)[001] of grains along the steel rolling direction could increase its magnetic permeability, thus helping to improve the efficiency of the transformer. This grain orientation is known as GOSS texture. The (110) plane lies in the sheet plane, and the [001] direction points approximately parallel to the rolling direction of the steel; thus, GOSS texture is also called the cube-on-edge structure. The texture has its highest magnetic permeability and a lower loss when magnetised in the rolling direction than that of other directions.
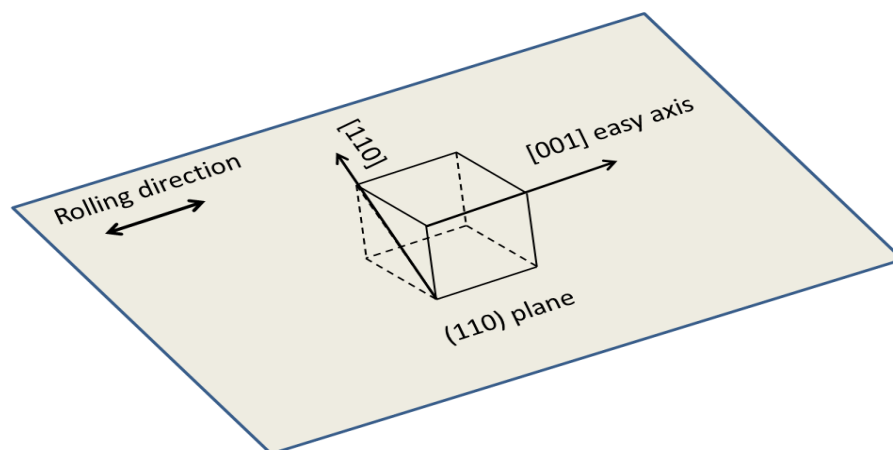
Figure 2.6 GOSS steel showing cube-on-edge orientation.

Grain oriented electrical steels are made from hot rolled coils usually containing 3 wt% Si and a certain amount of grain growth inhibitors. Figure 2.7 shows a schematic diagram of the processing route for making the grain oriented electrical steels used at Cogent Power Ltd [2.12], which is typical for this class of material.

The initial material is passed through a series of production processes during the manufacture of electrical steel as shown in figure 2.7, through which the final product is produced with the desired gauges, grain size and grain orientation.

The main production process is summarised as follows. The initial sheet's side is trimmed to remove any rough edges, and it is then annealed, pickled and oiled ready for cold rolling. The sheet gauge is reduced at the cold rolling mill and an anti-adhesion layer is coated on the sheet's surfaces prior anneal at the decarburising line. During decarburisation, the non-magnetic carbon, which can act as obstacles pinning domain wall movement and reduce material's magnetic permeability, is removed from the steel. Next is the high temperature coil anneal (HTCA) at around 1200°C, where with the help of restraining primary grain growth by pre-adopted inhibitors, the steel undergoes a secondary recrystalisation process for developing the GOSS texture grains. In addition, an electrically insulating coating known as forsterite is formed on the steel surface during the HTCA. This coating prevents inter-lamination eddy current from flowing when sheets are stacked in transformer cores. The steel is cooled after HTCA and goes through to the final production stage known as the thermal flattening line where a second coating known as phosphate is applied. The second coating acts primarily to apply beneficial tensile stress along the rolling direction of the steel. The application of the tensile stress helps reduce 180° domain wall spacing and lowers energy loss.

1. Side Trimming

2. Annealing & De-scaling

Anneal / Cool   De-scaling / Pickling

3. Cold Reduction

4. Decarburising Anneal

Preheat   Decarburising anneal   Coat & cure

5. High Temperature Coil Annealing

Furnace   Inner Cover   Coil   Stalk   Base Plate

6. Thermal Flattening

Clean   Pickle   Coat   Thermal flatten anneal / cool   Trim

7. Slitter

Slitter   Tension Unit
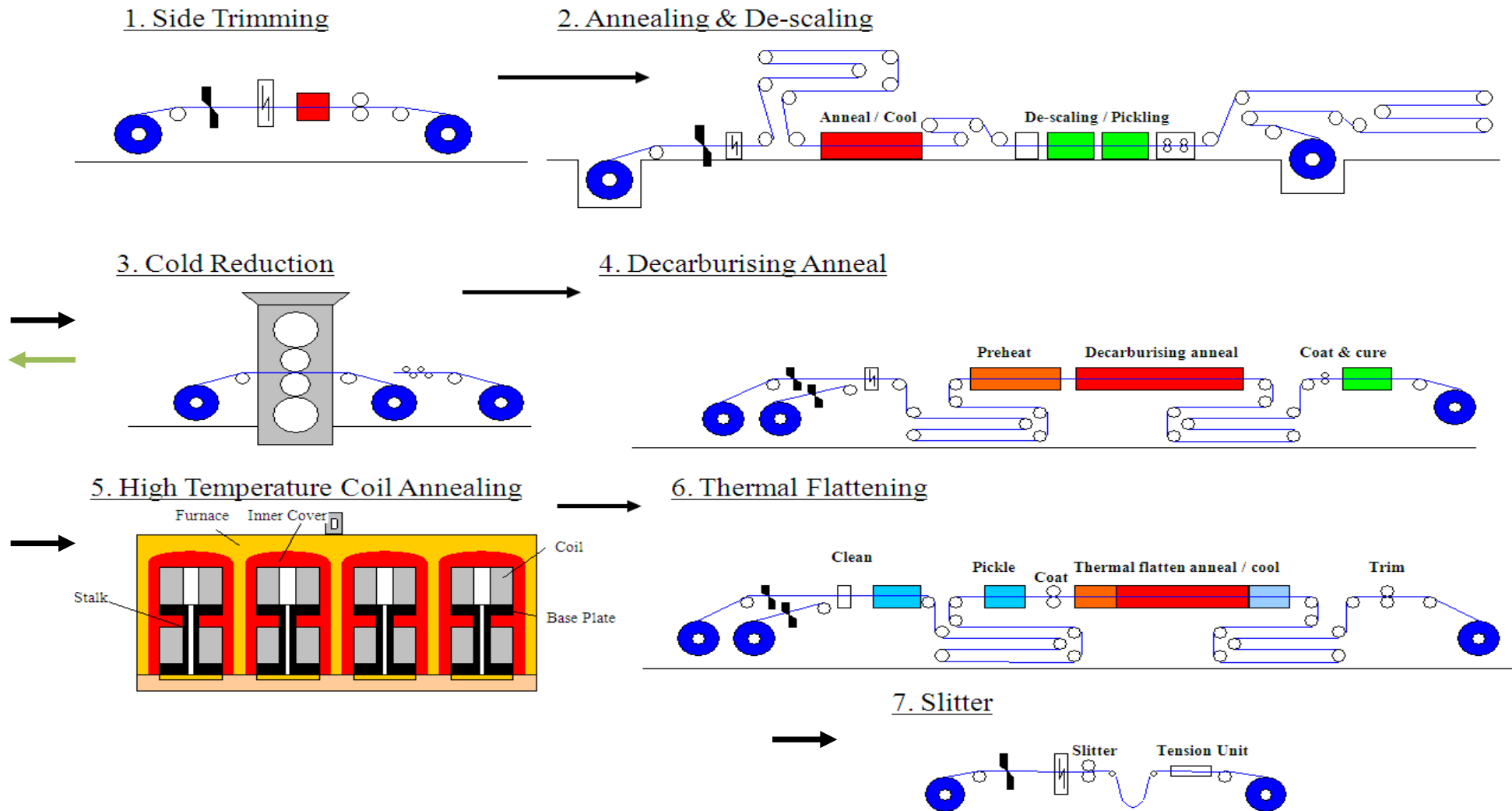
Figure 2.7 Diagram showing typical process route of making grain oriented electrical steels from the initial hot rolled steel coil [2.12].

Grain oriented steel is classified into two types according to the magnetic permeability; the comparably lower permeability **Conventional Grain Oriented steel** (CGO) and the **High-permeability Grain Oriented steel** (HiB). In general, the average deviation angle of the easy axis [001] from the rolling direction of the grains in HiB is less than CGO, approximately 3° for HiB and 7° for CGO. Therefore, less energy is consumed to magnetise HiB steels than that of CGO along the rolling direction. Detailed procedures for manufacturing CGO and HiB steels are shown in table 2.4 and table 2.5 respectively.

The main difference between CGO and HiB steel processing is the grain growth inhibitors used for obstructing the growth of grains other than GOSS texture. For CGO steels, manganese sulphide is used as a grain growth inhibitor whereas for HiB steel, additional aluminium nitride is added to further restrain the growth of other texture grains.

Grains of HiB steel are much larger that CGO and show wider domain wall spacing and increased total power loss due to increased eddy current loss [2.13]. Domain refinement, by means of scribing the surface of steel transverse to the rolling direction, is involved for the production of lower loss HiB steel. A typical method used in steel manufacture for domain refinement is laser scribing [2.15]. In this investigation, domain refined specimens were made by the ball scribing method (see section 8.8), because while the method has the same effect as laser scribing [2.16], it can be performed more easily in the laboratory environment. However, scratching damage the material surface and cause additional power loss. Hence, the optimal loss reduction is obtained by controlling the scribe spacing which varies depending on the sample condition and scribing parameters, usually between 4 and 6 mm [2.17][2.18].

Conventional Grain Oriented Steel

Initial Material: Hot rolled coil approximately 2 mm thick, 3% Si, specified amounts of manganese and sulphur (grain growth inhibitor: manganese sulphide).

Process Number (fig. 2.7)	Procedure	Purpose of Procedure
1, 2	Anneal at ~950°C, side trim, shot blast, pickle and oil.	To make material suitable for cold rolling and refine metallurgical structure of the hot rolled coil.
3	Cold roll to reduce thickness to ~0.6 mm	To flatten the steel and reduce gauge.
2	Intermediate Anneal at ~950°C	To recrystallise and soften the steel for final rolling.
3	Cold roll to final thickness 0.5 – 0.3 mm	To process the steel to finished gauge.
4	Decarburise at ~840°C in wet hydrogen and coat.	To remove remaining carbon from the steel; to further recrystalise and provide silica rich surface layer; to coat with magnesium oxide.
5	High temperature coil anneal at ~1200°C in very dry hydrogen.	To develop GOSS texture by secondary recrystalisation process; to form electrical insulation film; to purify the steel
6	Wash, thermally flatten and phosphate coat.	To remove remaining magnesium oxide; to apply second layer high tensile coating; to product flat and stress free material.
7	Side trim, slit and coil up	To get ready for sale.

Table 2.4 Corresponding CGO steel process details shown in fig. 2.7 [2.14].

High Permeability Grain Oriented Steel

Initial Material: Hot rolled coil approximately 2.3 mm thick, 3.2 – 3.5% Si, specified amounts of aluminium and other subsidiary elements (grain growth inhibitor: aluminium nitride and manganese sulphide).

Process Number (fig. 2.7)	Procedure	Purpose of Procedure
1, 2	Side trim, pickle, shot blast, anneal at ~1100°C in controlled atmosphere to avoid oxidation, water spray and oil.	To refine metallurgical structure by water quenching after high temperature annealing; to control distribution of aluminium nitride (grain growth inhibitor); to prepare steel for cold rolling.
3	Cold roll to finial thickness	To process the steel to finished gauge.
4	Decarburise at ~840°C in wet hydrogen and coat.	To remove remaining carbon from the steel; to further recrystalise and provide silica rich surface layer; to coat with magnesium oxide.
5	High temperature coil anneal at ~1200°C in very dry hydrogen.	To develop GOSS texture by secondary recrystalisation process; to form electrical insulation film; to purify the steel
6	Wash, thermally flatten and phosphate coat.	To remove remaining magnesium oxide; to apply second layer high tensile coating; to product flat and stress free material.
7	Side trim, slit and coil up	To get ready for sale.

Table 2.5 Corresponding HiB steel process details shown in fig. 2.7 [2.14]

2.4   Power losses in electrical steels

When electrical steels are operating under alternating current (AC) magnetisation, the total power loss P of the material can be divided into three components: the hysteresis loss P_h, the classical eddy current loss P_{cl} and the excess loss P_e [2.19], so that

$$P = P_h + P_{cl} + P_e \qquad (2.11)$$

The total power loss in each magnetisation cycle equals the area enclosed by the B –H loop. When magnetising frequency f→0, the loop contains mostly static P_h component. Increasing f broadens the loop due to the added dynamic P_{cl} and P_e components. Thus, each component plays a vital role in contributing to power loss at AC magnetisation.

The hysteresis loss is believed to be caused by the pinning of the domain walls due to the presence of defects (imperfection of the crystal lattice and impurities) in the material. It can be assumed to be frequency independent (at each magnetisation cycle) and mainly dependent on the material.

The classical eddy current loss is produced as a result of the changing magnetic flux density in the laminations of the electrical steel. Assume there is no skin effect so that flux densities at the surface and within the sheet are the same. The classical eddy current loss can be calculated using the equation below [2.19]

$$P_{cl} = \frac{\pi^2 B_p{}^2 d^2}{4\rho} f \times \frac{B_p}{B_{max}} \qquad (2.12)$$

where P_{cl} is classical eddy current loss in units of Joule per cubic meter per cycle (J/m^3 per cycle), B_p is the peak flux density, f is the frequency of the magnetisation in units of Hertz (Hz), d is the material thickness, ρ is the electrical resistivity of the material and B_{max} is the saturation magnetisation. The P_{cl} loss

component can be decreased by reducing the material gauge and increasing the material electrical resistivity.

The excess loss is the difference between the measured loss and the sum of the static hysteresis loss P$_h$ and the dynamic classical eddy current loss P$_{cl}$. The causes of this excess loss have not been fully understood, but some sources of the excess loss are widely agreed upon. For example, the micro-eddy current induced by moving domain walls [2.20], the excess eddy current generated by the unpinning of the domain walls and the non-uniformity distribution of the local magnetic flux density.

For electrical steels, when magnetised at peak flux density B, peak magnetising field H and magnetising waveform frequency f, the total power loss can be obtained by calculating the B – H loop area. Therefore, the total power loss P_t in units of Watt per kilogram (W/kg) is given by

$$P_t = \frac{1}{\rho T} \int_0^T H \frac{dB}{dt} dt \qquad (2.13)$$

where ρ is the material density and T is the period of magnetisation ($T = 1/f$).

References

[2.1]   B. D. Cullity, "Introduction to magnetic materials", Addison-Wesley, Reading, (1972).

[2.2]   D. C. Jiles, "Introduction to magnetism and magnetic materials", Second edition, Chapman & Hall, London, (1998).

[2.3]   Z, Lan, "Physics of Ferromagnetism", University of Electronic Technology Press, (1998).

[2.4]   S. Somkun, "Magnetostriction and magnetic anisotropy in non-oriented electrical steels and stator core laminations", Ph.D. thesis, Cardiff University, (2010).

[2.5]   A. Hubert and R. Schäfer, "Magnetic domains", Springer, pp. 25 – 26, (1998).

[2.6]   R. Comes, M. Gu, M. Khokhlov, J. Lu and S. A. Wolf "Microstructural and domain effects in epitaxial $CoFe_2O_4$ films on MgO with perpendicular magnetic anisotropy", Journal of Magnetism and Magnetic Materials, vol. 324, pp. 524-527, (2012).

[2.7]   S. Turner, A. Moses, J. Hall and K. Jenkins, "The effect of precipitate size on magnetic domain behaviour in grain-oriented electrical steels", Journal of Applied Physics, vol. 107, p. 09A307, (2010).

[2.8]   K. Honda and S. Kaya, "On the magnetization of single crystals of iron", Sci. Reports Tohoku Univ., 15, pp.721-753, (1926).

[2.9]   S. Chikazumi, "Physics of ferromagnetism", Oxford University Press Inc., New York, (1997).

[2.10] G. Bertotti, "Hysteresis in Magnetism: For physicists, Materials scientists, and Engineers", Academic Press, San Diego, (1998).

[2.11] N. P. Goss, "New development in electrical strip steels characterized by fine grain structure approaching the properties of a single crystal", Transactions of the American Society for metals, vol. 23, pp. 511-531, (1935).

[2.12] http://www.orb.gb.com/downloads/cogent_brochure.pdf. Last accessed on 20th June 2013.

[2.13] J. Shilling, "Magnetic properties and domain structure in grain-oriented 3% Si-Fe", IEEE Transactions on Magnetics, vol. 10, pp. 195-222, (1974).

[2.14] P. Beckley, "Electrical steels", European Electrical Steels, Newport, (2000).

[2.15] T. Luchi, S. Yamaguchi, T. Ichiyama, M. Nakamura, T. Ishimoto and K. Kuroki, "Laser processing for reducing core loss of grain oriented silicon steel", Journal of Applied Physics, vol. 53, pp. 2410-2412, (1982).

[2.16] P. Beckley and D. Snell, "Low-cost, high-speed domain refinement without damage to insulative coatings", Journal of Materials Engineering and Performance, vol. 3, pp. 209-213, (1994).

[2.17] S. V. Ponnaluri, R. Cherukuri and P. A. Molian, "Core loss reduction in grain-oriented silicon steels by excimer laser scribing Part I: experimental work", Journal of Materials Processing Technology, vol. 112, pp. 199-204, (2001).

[2.18] R. F. Krause, G. C. Rauch, W. H. Kasner and R. A. Miller, "Effect of laser scribing on the magnetic properties and domain structure of high-permeability 3% Si-Fe", Journal of Applied Physics, vol. 55, pp. 2121-2123, (1984).

[2.19] S. E. Zirka, Y. I. Moroz, P. Marketos and A. J. Moses et al, "Loss separation in nonoriented electrical steels", IEEE Transactions on Magnetics, vol. 46, pp. 286-289, (2010).

[2.20] S. Flohrer, R. Schafer, J. McCord, S. Roth, L. Schultz, F. Fiorillo, W. Gunther and G. Herzer, "Dynamic magnetization process of nanocrystalline tape wound cores with transverse field-induced anisotropy", Acta Materialia, vol. 54, pp. 4693 – 4698, (2006).

Chapter 3

Previous Related Work

This chapter summarises the previous dynamic domain behaviour, localised flux density, localised magnetic field and localised power loss studies which are most relevant to this investigation in the variation of localised magnetic properties of grain oriented electrical steels.

3.1 Dynamic domain behaviour and non-uniform magnetisation.

Localised variation of magnetic properties can influence the quality of grain oriented electrical steels, steel with uniform magnetisation is thought to have lower loss than those with non-uniform magnetisation; thus, it is ideal to have all domain walls of grain oriented electrical steels move smoothly and at the same speed under AC magnetisation. In reality, when electrical steel is magnetised at 50 Hz, domain walls move inhomogeneously at different velocities, resulting non-uniform magnetisation. This inhomogeneity in domain wall movement is thought to be mainly due to a number of reasons [3.1-3.3] summarised below:

3.1.1 Domain wall refinement

The number of domain walls increases accordingly with the magnetising frequency and magnetic induction, which is known as domain refinement and was first proposed by Polivanow [3.4]. By creating additional domain walls can reduce the speed of individual domain walls in the process of AC magnetisation and

consequently decrease power loss due to the reduction of the eddy current component. The relationship between domain wall spacing and magnetising frequency has been studied by Haller [3.5] and Sharp [3.6]; their experimental results showed that above the frequency of 40 Hz and flux density of 1.2 T, the relationship between domain wall spacing D and frequency f of sinusoidal magnetisation can be written as

$$D \propto \frac{1}{f^{(\frac{1}{2})}} \qquad \qquad 3.1$$

3.1.2 Grain to grain variation of magnetic permeability.

Grain oriented electrical steels are polycrystalline material containing grains that are slightly deviated from the rolling direction. The deviation angle varies from grain to grain. Therefore, when the steel is magnetised under a uniform magnetising field in the rolling direction of the sheet, domain walls in grains having smaller deviation angle are more mobile than that of larger deviation angle as result of the crystal anisotropy.

3.1.3 Creation and annihilation of 90° surface closure domains.

The creation of surface closure domains (or lancet domains) reduces the magnetostatic energy produced by surface free poles. A small inclination angle between the easy magnetisation axis of grains and the sheet plane is expected to develop during coil annealing process (or secondary crystallisation), which leads to free magnetic poles on either surfaces of the steel. The number of surface closure domains increases with an increasing inclination angle. These surface closure domains do not appear at a low magnetisation condition with strong surface tension and at inclination angles less than 0.5° [3.1]. They appear at high magnetisation and disappear when magnetisation is low. The process is repeated under AC magnetisation.

3.1.4   Pinning of the 180° domain wall movement.

The 180° main domain walls are pinned by defects when moving in electrical steel. Such defects could be impurities, surfaces roughness, residual stresses and precipitates. Since pinning activity increases with an increasing number of closure domains, it is also expected that the pinning effect is caused by interactions between 90° closure domains and 180° main domains [3.1].

Ushigami [3.2] observed dynamic domain patterns of a grain oriented electrical steel using Kerr microscopy. Result of his observations showed that some 180° domain walls were not straight and moving inhomogeneously due to the pinning effect. Moses [3.7] observed real-time domain wall movement using the stroboscopic method at different field frequencies. Non-repeatable wall motion was frequently observed at power frequencies, which indicates that domain wall pinning occurs irregularly from cycle to cycle magnetisation.

3.2   Variation of localised magnetic flux density, magnetising field and power loss in grain oriented electrical steels.

Tumanski [3.8-3.9] studied the correlation between power loss and distribution of localised magnetising field in grain oriented electrical steels. He found that electrical steel sheets with higher losses also showed broader distribution of local magnetic field values and higher average field strength values. Therefore, loss assessment of grain oriented steels can be achieved by analysing characteristics of the distribution of local magnetic field. In addition, he measured localised power loss over an area of 10 x 10 mm on a conventional grain oriented specimen at overall peak flux density of 1.0 T. The result showed that localised power loss varies as much as 30 %.

Moses [3.10] studied the effects of grain boundaries on the field distribution of grain oriented steels. He found that the surface fields on two sides of the steel were similar but not equal since grain boundaries may not at the same position of the two surfaces. A range of inclination angles of grain boundaries from sheet

surfaces was observed and varying from 89° to 26°. As a result, if the sheet is 0.35 mm thick, grain boundaries could be dislocated at the opposite surface by as much as 1 mm.

Tone [3.11] analysed magnetic characteristic of grain oriented electrical steel by using computer modelling. The local flux density and magnetic field was analysed using Finite Element Method (FEM) by taking consideration of the grain deviation angle, the grain boundary effect and the direction of external field. Local power losses were calculated from the flux density and magnetic field vectors at an overall flux density of 1.0 T. The results indicated that the local power loss value is strongly influenced by the in-plane deviation angle and the relative mismatch angle between adjacent grains. Higher loss values were found at nearby grain boundary regions and particularly at high angle grain boundaries, since the magnetostatic energy is high in those regions.

Overshott [3.12] studied power loss and flux density between neighbouring grains in grain oriented steel under the overall flux density range from 0.4 to 1.4 T and external field frequency range from 20 to 120 Hz. The results showed that over this range of magnetisation, the local flux density can differ by up to 20 % with respect to overall flux density. Relatively higher flux density and power loss were measured in well oriented grains in comparison with deviated grains. This is because flux tends to avoid distribution on the relatively deviated grains by sharing more flux density between the relatively well oriented grains.

Senda [3.13] and [3.14] studied the distribution of localised magnetic flux density and power loss in HiB steel at the overall flux densities of 0.5, 1.0, 1.3 and 1.7 T. Localised power loss showed a similar distribution trend as those of localised flux density. This shows that power loss is strongly influenced by flux density distribution. An investigation into variation of localised flux density was carried out by the author, and as shown in Figure 3.1, these maps show distributions of localised flux density at different levels of peak overall flux density B_m. The showing grain in figure 3.1 has relative large deviation angle (8°), and the rest of the grains with deviation angles less than 4° are ignored.

At a lower B_m (0.5 T), flux tends to distribute itself along the rolling direction and avoid the highly mis-oriented grain, resulting elongated flux density patterns as seen in figure 3.1 (a). At a higher B_m (1.0 and 1.3 T), flux density tends to distribute more corresponding to the grain structures. Regions of higher flux density appear at both pole ends of the mis-oriented grain. This is because flux distributed to reduce the magnetostatic energy generated by magnetic poles at grain boundaries. Therefore, it was concluded that magnetic poles at grain boundaries affect the non-uniform distribution of flux density. At an even higher B_m (1.7 T), change in the domain structures occur, the band domain walls [3.15] start to replace a small portion of the 180° domains, and magnetostatic energy profile will not be the same as that of a lower B_m.
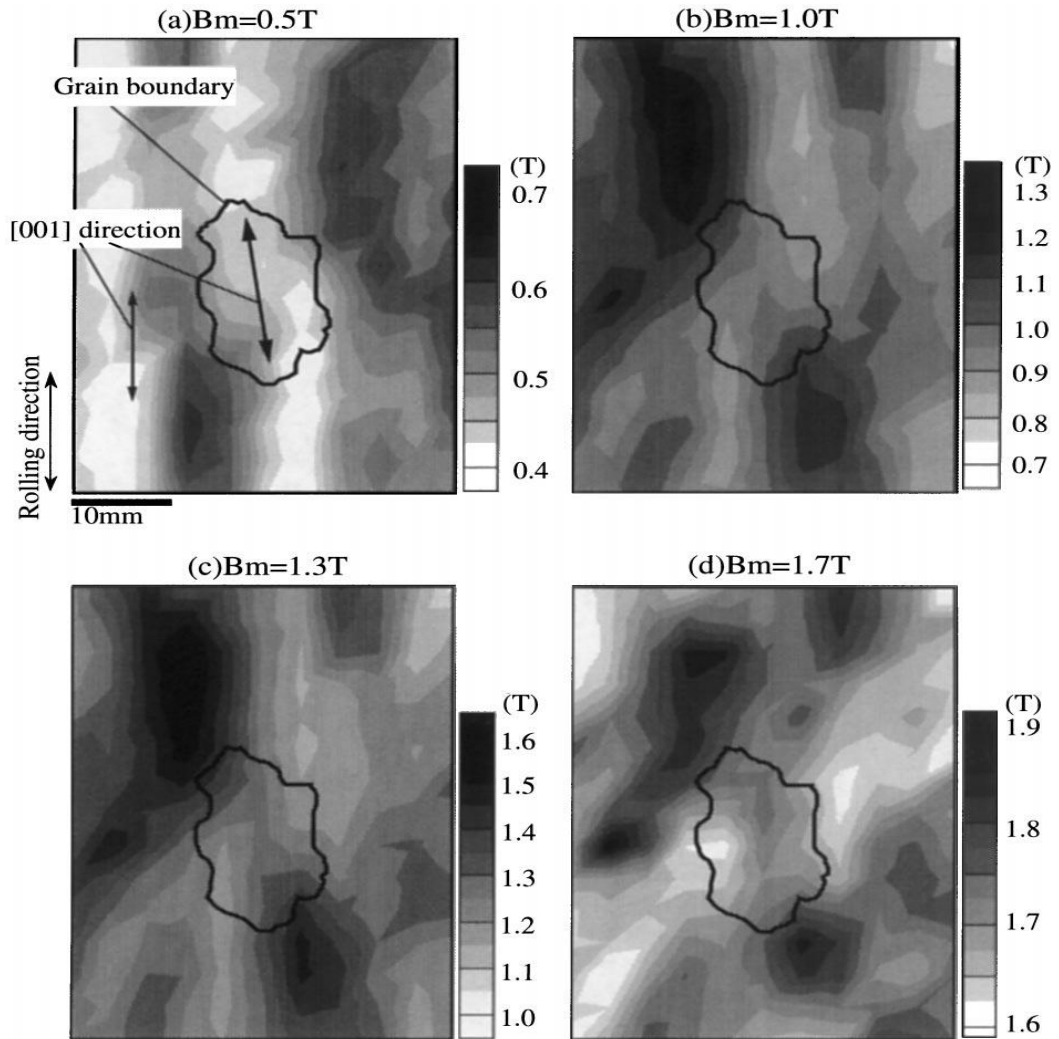
Figure 3.1 Contour maps showing distribution of local flux density measured by needle probe at B_m = 0.5, 1.0, 1.3 and 1.7 T [3.14].

References

[3.1]   T. Nozawa, M. Mizogami, H. Mogi and Y. Matsue, "Magnetic properties and dynamic domain behaviour in grain-oriented 3 % Si-Fe", IEEE Transactions on Magnetics, vol. 32, pp. 572 – 589", (1996).

[3.2]   Y. Ushigami, M. Mizokami, M. Fujikura, T. Kubota, H. Fuji and K. Murakami, "Recent development of low-loss grain-oriented silicon steel", Journal of Magnetism and Magnetic Materials, vol. 254 – 255, pp. 307 – 314, (2003).

[3.3]   Z. Xia, Y. Kang and Q. Wang, "Developments in the production of grain-oriented electrical steel". Journal of Magnetism and Magnetic Materials, vol. 320, pp. 3229 – 3233, (2008).

[3.4]   K. M. Polivanov, "Dynamic characteristics of ferromagnetic materials", Lzv. Akad. Nauk SSSR Ser Fiz, vol. 16, pp. 449 – 464, (1952).

[3.5]   T. R. Haller and J. J. Kramer, "Observation of dynamic domain size variation in a silicon-iron alloy", Journal of Applied Physics, vol. 41, pp. 1034 – 1035, (1970).

[3.6]   M. R. G. Sharp, R. Phillips and K. J. Overshott, "Dependence of loss on domain-wall spacing in polycrystalline material", Electrical Engineers, Proceedings of the institution of, vol. 120, pp. 822 – 824, (1973).

[3.7]   A. J. Moses, P. I. Williams and O. A. Hoshtanar, "Real time dynamic domain observation in bulk materials", Journal of Magnetism and Magnetic Materials, vol. 304, pp. 150 – 154, (2006).

[3.8]   S. Tumanski, "The application of permalloy magnetoresistive sensors for non-destructive testing of electrical steel sheets". Journal of Magnetism and Magnetic Materials, vol. 75, pp. 266 – 272, (1988).

[3.9]   S. Tumanski and T. Winek, "Measurements of the local values of electrical steel parameters", Journal of Magnetism and Magnetic Materials, vol. 174, pp. 185 – 191, (1997)

[3.10] A. J. Moses and S. N. Konadu, "Some effects of grain boundaries on the field distribution on the surface of grain oriented electrical steels", International Journal of Applied Electromagnetic and Mechanics, vol. 13, pp. 339 – 342, (2002).

[3.11] K. Tone, H. Shimoji, S. Urata, M. Enokizono and T. Todaka. "Magnetic characteristic analysis considering the crystal grain of grain-oriented electrical steel sheet", IEEE Transactions on Magnetics, vol. 41, pp. 1704 – 1707, (2005).

[3.12] K. J. Overshott and M. G. Blundell, "Power loss, domain wall motion and flux density of neighbouring grains in grain-oriented 3% silicon-iron". IEEE Transactions on Magnetics, vol. mag-20, pp. 1551 – 1553, (1984).

[3.13] K. Senda, M. Ishida, K. Sato, M. Komatsubara and T. Yamaguchi, "Localized magnetic properties in grain-oriented electrical steel measured by needle probe method", Electrical Engineering in Japan, Vol. 126, No. 4, pp. 942 – 949, (1999).

[3.14] K. Senda, M. Kurasawa, M. Ishida, M. Komatsubara and T. Yamaguchi, "Local magnetic properties in grain-oriented electrical steel measured by the modified needle probe method", Journal of Magnetism and Magnetic Materials, vol. 215 – 216, pp. 136 – 139, (2000).

[3.15] J. W. Shilling, "Grain boundary demagnetising field in 3% Si-Fe", Journal of Applied Physics, vol. 41, pp. 1165 – 1166, (1970).

Chapter 4

Review of Techniques for Observation of Magnetic Domains in Electrical Steels

4.1   Introduction to magnetic domain observation techniques.

Magnetic domain structures can reflect the metallurgical and magnetic properties of electrical steels. For example, the crystal orientation of grains in grain oriented electrical steel can be determined from the alignment of the 180° domain walls and the amount of the lancet domains distributed on the surface of the steel.

Bitter [4.1] made the first attempt to observe domain structures on the surfaces of iron, nickel and cobalt crystals using a magnetic powder technique. However, the initial pattern he observed using the technique was not clear and could not be fully interpreted at the time until Landau and Lifshitz developed their free energy theory of magnetism and made the correct theoretical predictions of domain structure in ferromagnetic material (cited in [4.2]).

Williams [4.3] used electrolytic polishing and observed clear domain patterns on the surface of single crystal silicon iron showing strong agreement with Landau and Lifshitz's predictive model. Thereafter, domain observation has been frequently used for the study of magnetic materials.

In general, techniques for observation of magnetic domains of electrical steels can be classified into three methods based on their observation mechanism. They are:

(1) Magnetic stray field sensitivity methods

   - *Bitter pattern*

   - *Magnetic force microscope (MFM)*

(2) Magnetic polarisation sensitivity methods

   - *Magneto-optical Kerr microscope*

   - *Transmission electron microscope (TEM)*

   - *Scanning electron microscope (SEM)*

(3) Crystal lattice distortion sensitivity methods

   - *Neutron diffraction*

   - *X-ray*

Each technique has unique advantages and limitations as outlined in the following sections. The aim of this chapter is to study techniques for observation of electrical steels and to compare and select the suitable techniques for this investigation.

4.2   Bitter Patterns

In 1932, Francis Bitter [4.1] demonstrated a technique for the observation of magnetic structures on iron, nickel and cobalt materials using 1µm diameter Fe_2O_3 particles suspended in ethyl acetate. The technique was a development based on the "old magnetic powder method" (cited in [4.1]), but with a much smaller particle size to reveal details, and the use of low viscosity ethyl acetate as a solution to improve the particle mobility so that they can settle quickly in the stray field. Although there was no definite explanation of the observed pattern at that time due to a lack of understanding of the domain concept, the historical significance of the technique's development is very important.

The Bitter method senses a stray field formed by the free poles on the sample surfaces. Thus, the contrast of the image relies on the interaction between the field and the ferromagnetic particles. Poor image contrast is often obtained using the Bitter method, thus the demand for improvement of the technique grows accordingly [4.4] (see modified Bitter technique outlined in chapter 6).

4.3   Magnetic Force Microscope

A magnetic force microscope (MFM) is a high-resolution scanning probe microscope which is designed for viewing micro and nano sized structures. In 1986, based on the concept of a scanning tunnelling microscope [4.5], Binnig et al. [4.6] developed the atomic force microscope (AFM). The microscope allows the surface topography of a sample to be imaged through a non-conductive method. During the scanning, an AFM probe, which consists of a force detective tip and force sensitive cantilever, is used to detect near-surface atomic forces. The cantilever deflects as the tip moves across the scanning surface, and the angle of deflection is sensed by a laser beam and a photo-detector so that the topograpic image can be plotted.

Later, based on the success of the AFM, Sáenz [4.7] and Martin [4.8] individually developed the MFM microscope for the observation of magnetic patterns. In the MFM, magnetic images are obtained by using an MFM tip which is typically made from an AFM tip and coated with a thin layer of magnetic material. During the scanning, the MFM tip interacts with the leakage field above the surface of the magnetic material to produce an image showing stray field profile of the scanning area. The highest spatial resolution of the MFM is reported at less than 10nm [4.9]. This enables micro and nano magnetic structures (e.g. domain walls) to be studied easily. Moses [4.10] made an attempt to observe grain boundary in grain oriented electrical steel using the MFM. A fine finger print pattern was found which has not yet been understood, but it has shown that the technique could provide useful information relating to the micro magnetism of electrical steels.

MFM is a near-surface raster scanning microscope, so a moderate sample preparation is necessary to obtain a reasonable smooth surface for preventing

contact damage and improving signal to noise ratio. The microscope offers typical scanning area of up to 100 x 100 µm, which is rather small compared to the magnetic features of grain oriented electrical steels.

4.4   Magneto-optical Kerr Microscopy

The observation principle of magneto-optical Kerr microscopy is based on the Kerr Effect [4.11], which was discovered by John Kerr in 1877 following the discovery of the well known Faraday Effect. The Faraday Effect occurs when the polarisation angle of a plane polarised light, propagating through a medium containing a magnetic field, changes because of the presence of the field. The Kerr effect describes the same concept but is a reflection effect rather than transmission, that is, a change in the polarisation angle of plane polarised light when the light is reflected from surface of a magnetic material.

To observe domain patterns using a Kerr microscope, the concept of Lorentz force is applied and an example is shown in figure 4.1. When a beam of plane polarised light is projected on a sample containing magnetic domains, a secondary light wave is induced by the Lorentz moment $vLor$ as stated in Huygens' Principle (cited in [4.12]). This secondary light is polarised perpendicular to the normal reflected light rotated by an angle of θ_k. If the observed sample contains anti-parallel domains such as on the surface of grain oriented steel, then $-\theta_k$ is obtained for light reflected from the neighbouring domains, thus, by using an analyser to block the entry of light with either $+\theta_k$ or $-\theta_k$, a image contrast showing the direction of the magnetisation of the observation area is formed. As a result, the domain pattern on the surface of a sheet of electrical steel can be revealed as in figure 4.1 using the Kerr microscope.
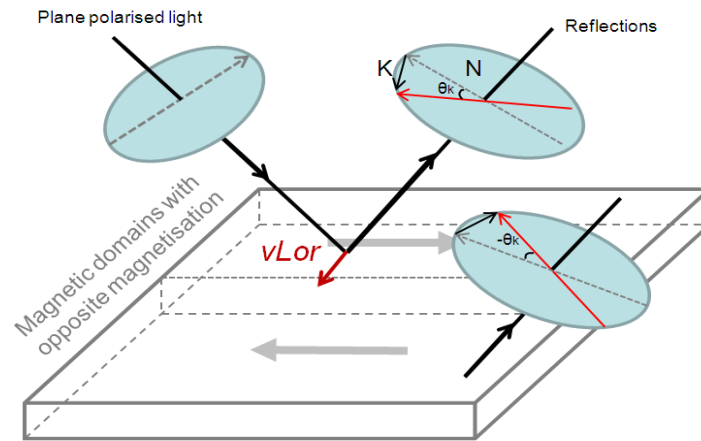
Figure 4.1 Illustration of the longitudinal Kerr Effect.

Since the Kerr microscope is an optical based apparatus, its resolution is limited by the wavelength of light (~200 nm). Takezawa [4.13] demonstrated that a higher resolution of 150 nm can be obtained by utilising UV light source in the Kerr microscope.

The main drawback of this method is that the technique involves time-consuming metallurgical sample preparation (see section 7.2). Thereafter the metallurgical preparation, a stress relief anneal is required to remove residual stress that added during the preparation for restoring domain pattern.

The Kerr microscope is a real time direct magnetisation observation apparatus. For this reason, Kerr microscopy has been intensively used for the study of domain wall movements in electrical steels [4.14 - 4.19].

Following the development of high speed cameras such as a charge-coupled device (CCD) or complementary metal oxide semiconductor (CMOS) cameras, dynamic domain images at or above power frequencies (≥50Hz) can be captured. These cameras can provide an improved recording speed and resolution in comparison to conventional cameras, such as Newicon tube cameras.

Moses [4.16] described an instrument for real time dynamic domain observation on the surface of electrical steels using the Kerr microscope and a CMOS camera (with recording speed of up to 1800 frames per second) at

magnetisation frequencies of up to 50 Hz. Such real time observation provides useful information for study of non-uniform wall mobility from grain to grain.

4.5   Transmission Electron Microscopy

Thin film samples of a thickness of up to 200 nm [4.20] are eligible for observation by transmission electron microscopy (TEM). In TEM, a beam of electrons with energies of up to 1000 keV impinges on the magnetic sample. The path of electrons is then deflected due to the Lorentz force. Diffracted electrons form a distorted pattern on a photographic film, which indicates domain configuration within the impinged region. This is known as Lorentz force microscopy.

High resolution is an advantage that makes TEM a viable method for observation of fine magnetic structures. The scanning differential phase TEM is reported to have a spatial resolution of 10 nm, which enables lattice defects and domain wall to be viewed simultaneously. For example, Akase [4.21] utilised TEM to study the interactions between domain walls and the strain field around precipitates and dislocations in non-oriented electrical steel sheets.

On the downside, samples for TEM examination demand a smooth and uniform thickness, thus specimen preparation is critical and time-consuming. In addition, TEM is very expensive and needs special training to operate.

4.6   Scanning Electron Microscopy

Domain observation by electron backscatter diffraction (EBSD) can be carried out using a scanning electron microscope (SEM). In EBSD, an electron beam with energies much lower than TEM (up to 100 keV) impinges the sample surface at a high incident angle, usually larger than 70°. The scattered electrons, including the higher energy scattered primary electrons that are reflected from the nuclei and the lower energy excited secondary electrons that are emitted from the atoms, are collected by the diffraction camera. If back scattering occurs on a magnetic material, both types of electrons will be deflected, in which the primary electrons are most sensitive to the sample internal magnetisation and the secondary electrons are

most sensitive to the stray field over the sample surface. In addition, in order to image magnetic domains using backscattered electrons, a direction and energy sensitive collector is also needed to extract the magnetic information.

The other worth to mention, direct domain observation method that uses SEM is the scanning electron microscopy with polarisation analysis (SEMPA). It is known that the secondary electrons emitted from magnetic sample have a spin polarisation which reflects the net spin density in the material [4.22]. The spin density, in turn, is directly related to the magnetisation of the material. In a similar way as the EBSD, by measuring secondary electron spin polarization, magnetic domains of magnetic samples can be reviewed using SEMPA.

The SEM method has a higher penetration depth and is less sensitive to surface roughness than that of TEM; thus, it is considered to be more bulk representative. Endo [4.23] observed domain patterns at about a depth of 10 μm from surface of grain oriented steel using the EBSD that was carried out at 160 kV.

4.7 X-ray and Neutron diffraction

The radiation sources of X-ray and neutron diffraction can be unique and distinguished from the TEM and SEM techniques. Synchrotrons (a combination of electromagnetic radiations that are accelerated by synchrotrons) and thermal neutrons are used respectively. The imaging method requires radiation to pass through the specimen, and on the other side, diffraction patterns are formed on the screen containing information with respect to the structure of crystal lattice. If the specimen is magnetic, then a distorted lattice structure is observed due to the presence of magnetostrictive strains. The domain image can be obtained by scanning the area of interest. There is a distinct difference between X-ray and neutrons that arises from the spin-orbit interaction of neutrons with magnetic materials, this results in additional Bragg peaks that allow identification of magnetic state (antiferromagnetic or ferromagnetic).

Both the X-ray and neutron diffraction techniques can reach a higher penetration depth than that of TEM and SEM due to the application of higher energy particles. Thus, the magnetic structure within electrical steels can be easily revealed. Withers studied [4.24] the penetration depth of synchrotron and neutron diffraction, for an iron based substrate. It was estimated that the penetration depth of synchrotron is up to 9 mm and neutron is up to 30 mm.

The main drawback of the X-ray and neutron diffraction technique is the safety concern. High radiation may damage the sample, and a radiation-proof shield is necessary.

4.8   Comparison of magnetic domain observation techniques

The techniques for observing static and dynamic domain structures on the surface or within electrical steels are compared in table 4.1. In summary, the stray field sensitive, low resolution Bitter technique is most suitable for imaging relatively large domain patterns on the surface of grain oriented steels, both with or without insulation coatings. The high magnification, high resolution, stray field sensitive MFM is suitable for revealing the fine domains of non-oriented steels with and without coatings. For dynamic domain observation on electrical steel, magneto-optical Kerr microscopy is the most appropriate method due to real time recording characteristic. TEM and SEM are direct magnetisation sensing techniques for observing micro and nano magnetic features and therefore the specimen must be prepared to a high finishing condition. X-rays and neutrons are powerful methods for the study of the magnetisation of a bulk sample; however care must be taken due to the high risk of radiation.

In this investigation, the static domain patterns of HiB steel specimens were observed using the Bitter technique because the method enables grain boundary and domain pattern to be revealed simultaneously across the entire loss scanning area on Epstein specimens outlined in chapter 8. Dynamic domain patterns of HiB steel at 50 Hz magnetisation were studied using the Magneto-optical Kerr

microscope. The real time direct magnetisation observation characteristic enables surface domain wall movement to be imaged at power frequency.

In addition, a detailed study of the Bitter technique and the magneto-optical Kerr miscroscope for observation of domains in HiB specimen is carried out in chapter 8 and 9, in which inconsistency in domain patterns obtained using the Bitter technique and the Magneto-optical Kerr microscope on the same HiB specimen is discussed. Therefore, improved understanding in observation mechanism of both techniques is achieved.

Observation techniques	Level of Sample preparation	Assessment on direction of magnetisation	Observation through coatings of steels	Sensitivity to change in magnetisation	Spatial resolution	Dynamic observation	Recording time	Used in this study
Bitter	very low	indirect	yes	excellent	Low (1μm)	no	Few secs	yes
MFM	Low - moderate	indirect	yes	good	High (10 nm)	no	Tens of mins	no
Kerr	moderate	direct	no	fair	Moderate (0.1 μm)	yes	Real-time	yes
TEM	very high	direct	no	good	Very high (1 nm)	possible	Few secs	no
SEM	high	direct	no	good	High (10 nm)	possible	Few secs	no
X-ray, Neutron	low	indirect	no	poor	Very low (5 μm)	no	Few mins	no

Table 4.1 Comparison of magnetic domain observation techniques. (adapted from [4.12])

References

[4.1]   F. Bitter, "Experiments on the nature of ferromagnetism", Physical Review, Vol. 41, pp. 507 – 515, (1932).

[4.2]   R. Carey and E. D. Isaac, "Magnetic domains and techniques for their observation, The English University Press Ltd, London, (1966).

[4.3]   H. J. Williams, R. M. Bozorth and W. Shockley, "Magnetic domain patterns on single crystals of silicon iron", Physical Review, vol. 75, pp.155-171, (1949).

[4.4]   R. J. Taylor, A. De Fisica, Serie B, Vol. 86, p. 126, (1990).

[4.5]   P. W. Epperlein, H. Seifert and R. P. Huebener, "Two-dimensional imaging of the current-density distribution in superconducting tunnel junctions", Physics Letters A, vol. 92, pp. 146 – 150, (1982).

[4.6]   G. Binning and C. F. Quate, "Atomic Force Microscope", Physical Review Letters, vol. 56, pp. 930 – 933, (1986).

[4.7]   J. J. Sáenz, N. Garcia, P. Grutter and E. Meyer, "Observation of magnetic forces by the atomic force microscope", Journal of Applied Physics, vol. 62, pp. 4293 – 4295, (1987).

[4.8]   Y. Martin and H. K. Wickramasinghe, "Magnetic imaging by "force microscopy" with 1000 Å resolution", Applied Physics Letters, vol. 50, pp. 1455 – 1457, (1987).

[4.9]   M. Ohtake, K. Soneta and M. Futamoto, "Influence of magnetic material composition of Fe $_{100-x}$B $_x$ coated tip on the spatial resolution of magnetic force microscopy", Journal of Applied Physics, vol. 111, pp. 07E339-1 – 07E339-3, (2012).

[4.10] A. J. Moses, P. I. Anderson, N. Chukwuchekwa, J. P. Hall, P. I. Williams and X. T. Xu, "Analysis of magnetic fields on the surface of grain oriented electrical steel", MEASUREMENT 2011, Proceeding of the 8th International Conference, pp. 107 -110, (2011).

[4.11] J. Kerr, "On rotation of the plane of polarization by reflection from the pole of a magnet", Philosophical Magazine, Vol. 3, p. 321, (1877).

[4.12] A. Hubert and R. Schäfer, "Magnetic domains", Springer, pp. 25 – 26, (1998).

[4.13] M. Takezawa, "Magnetic domain observation of Nd-Fe-B magnets with submicron-sized grains by high-resolution Kerr microscopy", Journal of Applied Physics, vol. 109, pp. 07A709-1 – 07A709-3, (2011).

[4.14] K. Kawahara, Y. Yagyu, S. Tsurekawa and T. Watanabe, "Observations of interaction between magnetic domain wall and grain boundaries in Fe-3wt%Si alloy by Kerr microscopy", Materials Research Society Symposium, vol. 586, pp. 169 – 174, (2000).

[4.15] M. Takezawa, K. Kitajima, Y. Morimoto and J. Yamasaki, "Dynamic and wide field domain observation of amorphous ribbons with longitudinal Kerr effect microscopy", Journal of Applied Physics, vol. 97, pp. 10F701-1 – 10F701-3, (2005).

[4.16] A. J. Moses, P. I. Williams and O. A. Hoshtanar, "A novel instrument for real-time dynamic domain observation in bulk and micromagnetic materials", IEEE Transactions on Magnetics, vol. 41, pp. 3736 – 3738, (2005).

[4.17] S. Flohrer, R. Shafer, J. McCord, S. Roth, L. Schultz and G. Herzer, "Magnetization loss and domain refinement in nanocrystalline tape wound cores", Acta Materialia, vol. 54, pp. 3253 – 3259, (2006).

[4.18] O. Hoshtanar, "Dynamic domain observation in grain-oriented electrical steel using magneto-optical techniques", PHD thesis, Cardiff University, (2006).

[4.19] R. Schäfer, "Investigation of domain and dynamics of domain walls by the magneto-optical Kerr-effect", Handbook of Magnetism and Advanced Magnetic Materials, vol.3, (2007).

[4.20] http://www.fei.com/uploadedfiles/documentsprivate/content/tem_sample, accessed on 16th Aug. 2012.

[4.21] Z. Akase, D. Shindo, M. Inoue and A. Taniyama, "Lorentz microscopic observations of electrical steel sheets under an alternation current magnetic field", Materials Transections, vol. 48, pp. 2626 – 2630, (2007).

[4.22] J. Unguris, "Scanning electron microscopy with polarization analysis (SEMPA) and its applications", National Institute of Standards and Technology, Gaithersburg, Maryland, p1 of Chapter 6, (2000).

[4.23] H. Endo, S. Hayano, Y. Saito, M. Fujikura and C. Kaido, "Magnetisation curve plotting from the magnetic domain images", IEEE Transactions on Magnetics, vol. 37, pp. 2727 – 2730, (2001).

[4.24] P. J. Withers, "Depth capabilities of neutron and synchrotron diffraction strain measurement instruments. II. Practical implications", Journal of Applied Crystallography, vol. 37, pp. 607 – 612, (2004).

Chapter 5

Review of Localised Magnetic Flux Density, Magnetising Field and Power Loss Measurement Methods

5.1   Localised magnetic flux density measurement techniques

Search coil and needle probe techniques are often employed for the measurement of localised magnetic flux density on electrical steel specimens. In this section, both techniques are reviewed with regards to related theories and previous related work in order to select the appropriate technique of flux density measurement in this investigation.

5.1.1   Search coil method

A search coil measures the magnetic flux density by applying Faraday's law of induction. The law is defined as follows: "the induced emf in an electrical circuit is proportional to the rate of change of magnetic flux enclosed by the circuit" [5.1]. For a path of flux at an angle θ to the plane of an enclosed circuit the emf is related to the change in magnetic flux by

$$emf = -\frac{d\phi}{dt} \bullet \sin\theta \qquad (5.1)$$

If the flux ∅ is perpendicular to the plane of the circuit, $\theta = 90^o$, then

$$emf = -\frac{d\phi}{dt} \qquad (5.2)$$

where emf is the induced electron motive force in the circuit with a unit of volt (V), and ϕ is the magnetic flux with a unit of Weber (Wb). The negative sign is included because Lenz's law states that "the current produced in a circuit by the induced emf will always generate a magnetic field that is against the original magnetic flux" [5.2].

If the circuit is made of an N-turn coil, then the induced emf in the circuit can be written as

$$emf = -N\frac{d\phi}{dt} \qquad (5.3)$$

The above equation can be re-written as a function of magnetic flux density by substituting $\phi = AB$, where A is the cross sectional area of the circuit, and is given by

$$emf = -NA\frac{dB}{dt} \qquad (5.4)$$

In an alternating field, an instantaneous flux density value B_i of a sinusoidal waveform of frequency f and peak flux density B_{peak} is given by

$$B_i = B_{peak} \sin \omega t \qquad (5.5)$$

where $\omega = 2\pi f$ is the angular frequency, t is the time. Differentiating equation (5.5) with respect to time t gives

$$\frac{dB_i}{dt} = \omega B_{peak} \cos \omega t \qquad (5.6)$$

Now, substituting equation (5.6) into (5.4) gives

$$emf = -NA\omega B_{peak}\cos\omega t \qquad (5.7)$$

The average emf in the circuit can be obtained by integrating equation (5.7) over a half cycle of the cosine wave (from $\pi/2$ to $3\pi/2$) and is expressed as

$$emf_{avg} = \frac{1}{\pi}\int_{\pi/2}^{3\pi/2} NA\omega B_{peak}\cos\omega t d\omega t$$

$$= \frac{2}{\pi}NA\omega B_{peak} \qquad (5.8)$$

Equation (5.8) can be simplified by substituting $\omega = 2\pi f$ and is expressed as

$$emf_{avg} = 4B_{peak}ANf \qquad (5.9)$$

Thus, equation (5.9) can be used to calculate B_{peak} of a sinusoidal flux density wave. Figure 5.1 shows the configuration of a single turn search coil method for measurement of local magnetic flux density. An enamelled insulated copper wire is wound on the sample through two drilled holes to form an enclosed loop; the excess lead wires at the exit are twisted in order to reduce the influence of air flux. If a magnetic field is applied to the sample, then the relationship between the induced V_{avg} and B_{peak} is expressed by equation (5.9).
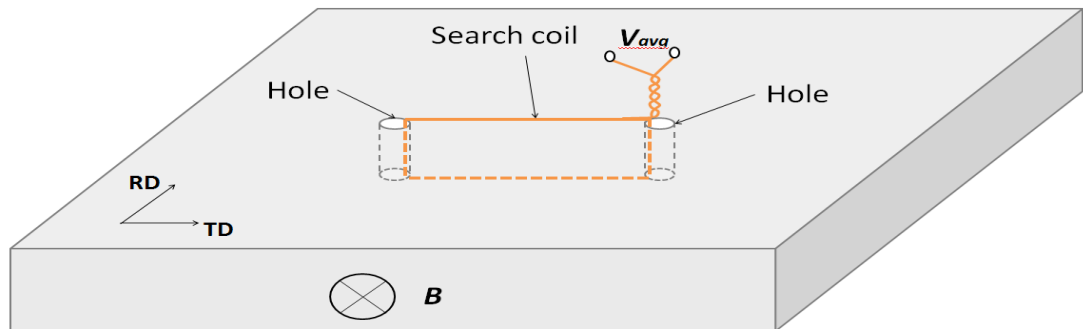

Figure 5.1 Illustration of a single turn search coil.

Some possible sources of error in the search coil method are outlined below:

- The influence of air flux [5.3]. An air gap could be enclosed when winding the coil on the sample; this could result a higher measurement.

- The effect of stress on local magnetic structure. Drilling-induced residual stress and magnetostatic energy can cause reconfiguration of local magnetic domain structures. An example of how domain structure is changed after drilling is shown in figure 5.2. Distorted domain pattern is observed around the edges of the hole, they indicate the damaged region caused by drilling. Domain reconfiguration could cause a slight change in the magnetisation process, thus leading to an inconsistent flux density measurement before and after drill search coil holes.
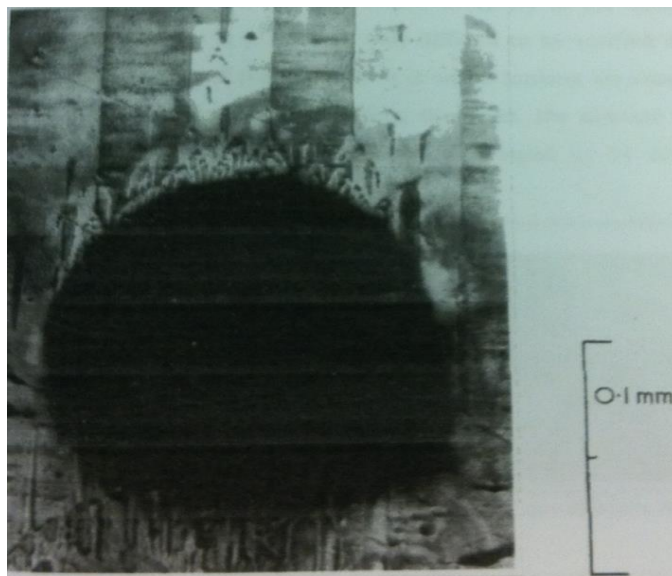
Figure 5.2 Distorted magnetic domain pattern around drilled hole in grain oriented electrical steel [5.4].

- Error due to the measurement of the area enclosed by the search coil. Care must be taken when calculating the area of the search coil to use in equation 5.9. It is shown in figure 5.3 that a deformed flux path is predicted near the search coil holes. Total flux enclosed by the coil is equivalent to the flux shown in the effective area. As a result, the effective distance should be taken into calculation of the search coil enclose area; that is, the distance

between the two centres of the drill holes multiplies the thickness of the specimen.
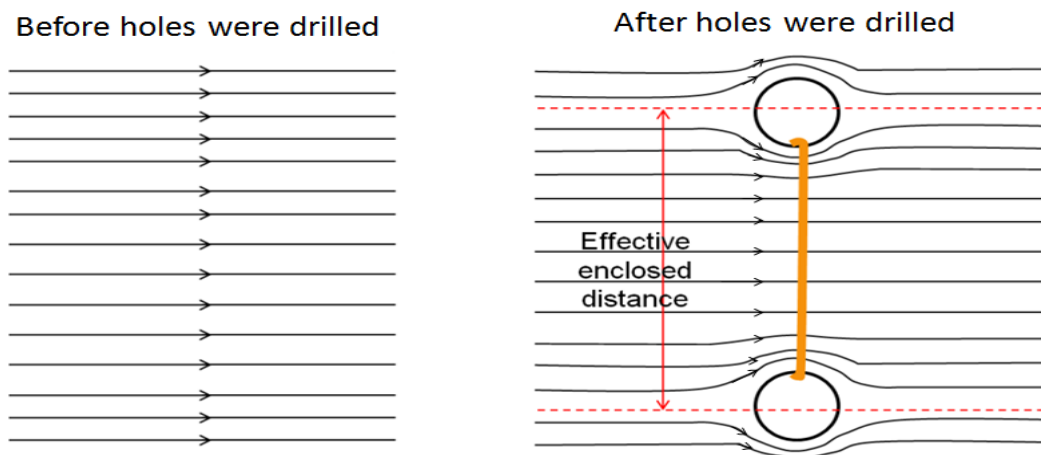
Figure 5.3 Illustration of change in flux distribution before and after holes were drilled for installation of the search coil.

- Short circuits due to burrs cut. The enamelled insulated wire is usually used to prevent direct contact between the coil and the test specimen. However, the insulation coating could be damaged by sharp burrs around the drill holes and lead to a short circuit of the search coil.

- Magnetic degradation caused by drilling. Drilled holes are occupied by air whose magnetic permeability is much lower than that of the electrical steel specimen. Localised intense application increases the volume fraction of air, leading to a significant decline of the magnetic permeability of the test specimen.

Some of the drawbacks discussed above could be minimised by reducing the hole diameter to reduce the damaged region, covering the burrs with non-magnetic coating (e.g. nail varnish) to prevent short circuits, and stress relief annealing to remove some of the drill induced stress.

Some history and previous related investigations of the search coil method are summarised below:

The search coil method for the measurement of local flux density in electrical steels was first developed by Brailsford and Mazza [5.5]. They drilled holes in a steel specimen and coated the sides with insulation material. A single turn coil was wrapped through the holes and flux density was determined from the induced voltage signal.

Later, Mapps [5.4] studied the effect of drill holes on local domain structures of grain oriented steels. Distorted domain patterns were observed around all drill holes, and he found that the holes that were drilled on grain boundaries has less effect on domain configuration compared to those within the grains.

Tumanski [5.6] and [5.7] carried out an investigation to study the effect of drilling on the magnetic properties of electrical steels. His experimental results showed that annealing cannot completely remove the damage caused by drilling as closure domains were created around the holes to reduce flux leakage and the remaining plastic stress will continue to cause change in domain structure as seen in figure 5.2.

Zurek [5.8] analysed the effect of twisting lead wire on the accuracy of search coil measurements. A 0.1 mm diameter enamelled wire was used for making search coil in the investigation; the experimental results showed that a tight and uniformly twisted lead wire can reduce the influence of stray fields by up to 60% on flux density measurement compared to a loosely twisted wire.

5.1.2   Needle probe method

The needle probe method detects magnetic flux density by means of measuring the electrical potential difference between two points on one surface of a specimen where needles are applied as shown in figure 5.4.

Two assumptions must be made in order to satisfy the needle probe theory which shows that the potential difference V_N (as shown in figure 5.4) between the needles is in proportion to the rate of change of flux in the area 12341. Firstly, it is assumed that the magnetic flux density is symmetrically distributed with respect to the centre line (dash line) of the cross sectional area of the test specimen shown in figure 5.4; thus, an equal amount of flux travels through the top and bottom sections of the specimen. Secondly, it is assumed that the ratio of the needle separation spacing to the specimen thickness is high so that the thickness of the specimen can be neglected when compared to the needle separation spacing.
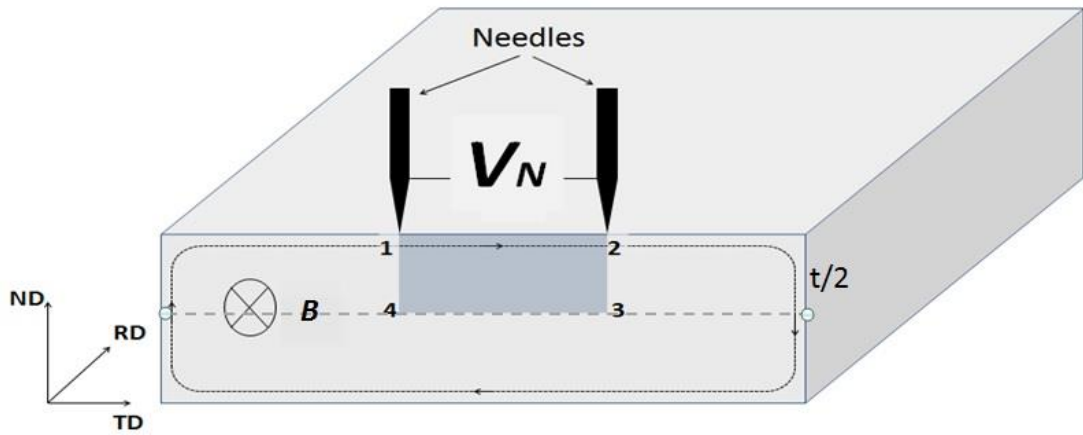
Figure 5.4 Illustration of needle probe method.

From the Maxwell-Faraday equation, the electric field created by a changing magnetic field within the area 12341 in figure 5.4 can be written as the closed loop integral shown below

$$\oint_C \vec{E} \bullet d\vec{l} = -\int_S \frac{d\vec{B}}{dt} \bullet d\vec{S} \qquad (5.10)$$

where C denotes the closed contour 12341, E denotes the induced electric field intensity and S denotes the area of the contour. By considering the components of the induced electrical field, equation (5.10) can be re-written as

$$\vec{V}_{12} + \vec{V}_{23} + \vec{V}_{34} + \vec{V}_{41} = \int_S \frac{d\vec{B}}{dt} \bullet d\vec{S} \qquad (5.11)$$

If the flux is distributed uniformly within the contour, then $V_{23} = V_{41}$ and $\vec{V}_{23} + \vec{V}_{41} = 0$ since they have opposite signs. $\vec{V}_{34} = 0$ since it is at the central line of the symmetrical shape, so equation (5.11) can be simplified as

$$\vec{V}_{12} = \int_S \frac{d\vec{B}}{dt} \bullet d\vec{S} \qquad (5.12)$$

Because $S = A/2$. Now, combining equation (5.12) with (5.8) gives the following equation for the average voltage between needles V_{12}:

$$V_{12} = 2B_{peak}Af \qquad (5.13)$$

For a single-turn search coil, the voltage induced in the coil is expressed as

$$V = 4B_{peak}Af \qquad (5.14)$$

Thus, from a computational perspective, the needle probe method is also considered as a half turn search coil. No holes are necessary so several of the drawbacks of the search coil method are not present and also the technique is less time-consuming than the search coil method.

However, the technique is susceptible to various errors [5.3][5.8][5.9] and [5.10] that may reduce the accuracy of the measurement, which are outlined below:

- The influence of air flux. Like the search coil method, the needle probe also suffers from the interference of air flux that is enclosed by the lead wire and needles. The important difference is that the enclosed air flux will lead to reduction of flux density measurement rather than increasing it.

- Systematic errors due to the remaining components of vertical electric fields [5.9]. The theory assumes that $V_{23} = V_{41}$ and $\vec{V}_{23} + \vec{V}_{41} = 0$. In practice, the test material probably contains different degrees of local anisotropy which

leads to $V_{23} \neq V_{41}$. Due to the second assumption made in the needle technique, this error is restricted to a minimum by assuming the component of the vertical electric field is neglected compared to the main horizontal electric field.

- Systematic errors due to the edge effect [5.10]. The application of the needle technique could fail at the specimen's near edge, where V_{34} (the centre line) is not zero. Thus, needle measurement must be conducted at a distance away from the edges of the specimen, usually a distance of 1/2 specimen thickness is recommended [5.11].

- The effect of the inhomogeneous nature of the material. It is important for the test material to be homogeneous throughout its thickness. The method assumes the same flux density should be present in the top and bottom sections of the test specimen; thus, the needle measurement obtained over one surface can be used to represent the flux density of the entire cross sectional area. However, the test materials may contain different degrees of inhomogeneity due to the manufacturing process and distribution of inclusions.

- The effect of insulation coating on needle measurement. The needle technique has been used for measurement of flux density of electrical steels without removing the insulation coating. Users apply sharp needles to pierce through the insulation and make an electrical contact with the specimen underneath. Poor contact may occur and will lead to a possible loss of the needle signals.

There are some useful methods which can be used to scale down the influence of these errors on needle measurement. Examples include increasing the ratio between needle separation spacing and specimen thickness, removing the insulation coating of test specimens and avoiding edge measurement by placing the probe at least ½ sample thickness away from the edges.

Some history and previous related investigations of the needle probe method are summarised below:

In 1949, Werner proposed a method for the measurement of magnetic flux density by means of measuring the potential difference between two needles placed on the test sample (cited [5.3] and [5.8]). Later, the method was patented separately by Czeija [5.12] and Stauffer [5.13].

The earliest work regarding the measurement of magnetic flux density in electrical steel samples using the needle probe technique was carried out by Tompkins [5.14]. In his experiment, local magnetic properties of a single sheet sample were measured by a probe which consisted of a pair of metal needles and a magnetic potentiometer (Chattock coil) element as shown in figure 5.5. The design allowed flux density and magnetising field to be measured locally, and the hysteresis loop of the test point could be plotted from flux density and magnetising field signals. In addition, power loss could be derived by integrating the product of BdH. The resolution of the probe was reported at 25.4 x 50.8 mm^2.
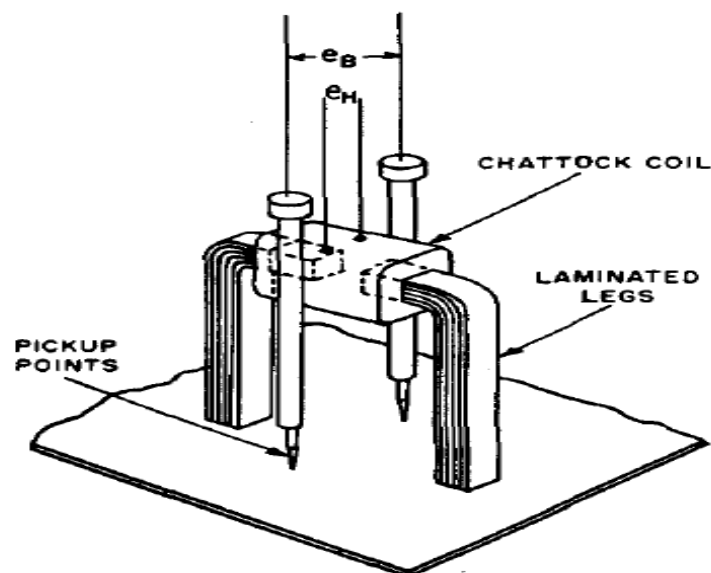

Figure 5.5 Illustration of the comparator probe [5.14].

Wilkins [5.15] set up an experiment to compare the needle probe technique with the search coil method on strips of grain-oriented electrical steels. A pair of brass needles was used for the elimination of the extraneous signals and was

placed, in turn, next to the 0.25 mm diameter search coil holes which were 6.35 mm apart. A single turn coil was wound through the holes to measure the flux density of the same region. The result showed that the output signals of both techniques were agreed well with each other across all measurement points.

Brix [5.16] designed an instrument for the measurement of rotational magnetisation, in which the flux density was detected utilising the needle probe technique. Probe needles were spring loaded to ensure successive contact during magnetisation. A similar experiment [5.17] was conducted using the search coil method; the flux densities at the identical locations agreed well with the measurements obtained using the needle probe technique.

Senda [5.18] studied the effect of the experimental set-up on the accuracy of the needle probe technique. Two tungsten needles with 50 μm tip diameters were placed 10 mm apart on 0.23 mm thick electrical steel specimen. The first experiment was conducted to investigate the effect of loading stress on the measurement. The results showed that the loading effect on local flux density value was less than 0.2 % for a 50 g / needle loading and was less than 1.5 % for loading which does not exceed 300 g / needle. The second experiment was conducted to investigate the influence of the symmetry of the in-plane eddy current on the needle probe measurement. The test specimen was magnetised in turn by two types of magnetising systems shown in figure 5.6. The type A configuration was one side contact and the type B configuration was two sides contact. In type A configuration, a maximum difference of 13 % was measured between measurements obtained using needle probe and search coil at induction of 1.7 T. Whereas in type B configuration, the maximum difference was only 0.9 %.

The differences in the type A configuration are caused by the non-symmetrical distribution of the eddy current and are explained by Nakata [5.19]. For the single-sided contact magnetising system, the generation of in-plane eddy current distorts the profile of the surface electric field and affects the accuracy of the needle probe measurement. However, for the double-sided contact magnetising system, the in-plane eddy currents generated on the two sides of the

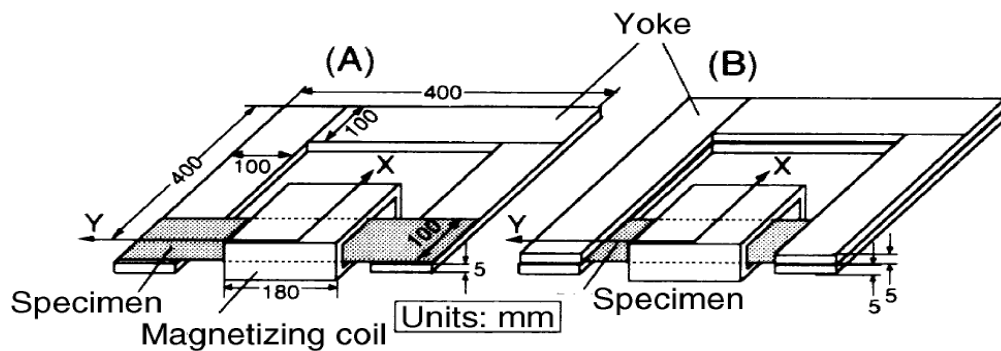specimen should cancel each other out since the rotation of the current are in the opposite directions.

Figure 5.6 Illustration of two different types of yoke configuration [5.18].

Loisos [5.9] carried out a critical evaluation of local magnetic flux density measurement methods. In the investigation, three techniques namely search coil, needle probe and modified needle probe were compared using a 0.5 mm thick non-oriented specimen, magnetised at 50 Hz and peak flux density range from 0.6 T to 1.4 T. The authors described the so called modified needle probe method which is demonstrated in figure 5.7. The method requires very precise needle positioning control; the two pairs of needles must be placed at identical locations on both sides of the specimen. Voltage V_A is induced by flux travelling in the area S_2 and voltage V_B is induced by flux travelling in the area $(S_1 + S_2)$. Therefore, the overall voltage induced in the measurement area BAA'B' equals $V_B - V_A$ and is equivalent to the voltage induced in a one turn search coil placed on the same area. During the experiment, the needle-separation-distance of both the needle probe method and the modified needle probe method were set to the same 25 mm, 11.5 mm and 4 mm. Single turn enamelled wire search coils were place at identical locations wound through the pre-drilled 0.5 mm diameter holes next to each needle point. Errors due to the vertical field in the needle probe method were studied by analysing the ratio between the needle separation and the specimen thickness. The highest percentage error occurred in the conventional needle probe measurement where the needle-separation distance was the lowest. This was found to be about 12.5 % for the 4 mm needle-separation and it reduced to 2 % for the 25 mm needle-separation. Whereas the modified needle probe showed less influence on the

vertical field since V_A and V_B cancelled out each other, a higher spread of measurements was observed.

The author stated that, for the considerable less homogenised grain oriented steel specimens, the use of the modified needle probe can provide improved accuracy. However, its application is often restricted because of the wiring connection and the demand for a precise positioning system.
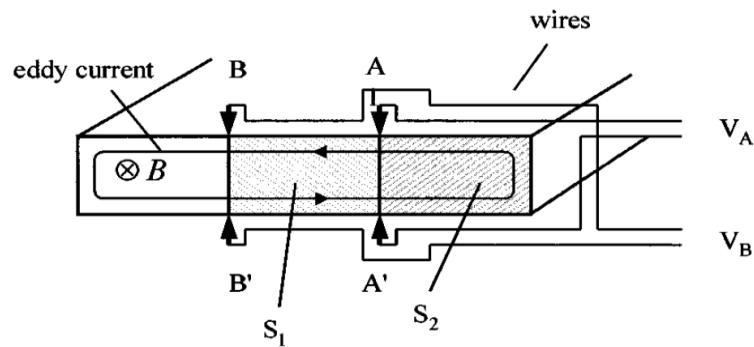

Figure 5.7 Illustration of the modified needle probe technique [5.9].

The latest use of the needle probe technique for flux density measurement was carried out by Crevecoeur [5.20]. A non-destructive investigation of the effect of cutting on the magnetic hysteresis properties of electrical steel specimens was carried out. The experimental technique applies a needle probe sensor that was described in the authors' earlier work [5.21] and is shown in figure 5.8 (a). The path of the eddy current is distorted as it approaches the cut edge as shown in figure 5.8 (b), the area $S_a \neq S_b \neq S_c$. Therefore, in order to obtain accurate results, S_b and S_c must be calculated numerically using the method described in [5.20] and [5.21]. The specimen under test was a laser cut non-oriented steel sheet, the test probe was made of 15 needles arranged transversely along the width of the sheet, the probe was placed with one end at the cut edge (degraded region) and the other end close to the centre of the sheet (non degraded region). The result showed that needle signals collected at the cut edge were higher than in the centre because the induction area S is larger at the edge. In addition, at the centre of the sheet where it was considered to be deformation free, the needle signal was found to be smaller.
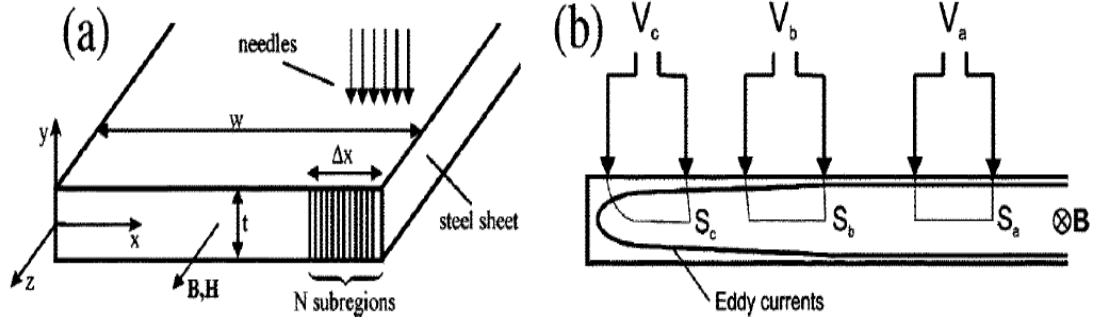
Figure 5.8 (a) Needle sensors. (b) Illustration of eddy current flow at sample edge and surfaces of induced voltage covered by needle sensors [5.20].

5.2 Local magnetic field measurement techniques

The magnetic field on the surface of electrical steel can be measured by a variety of techniques. In this section, two commonly used techniques, known as the air-cored induction coil sensor and the Hall Effect sensor, are discussed and commented on in order to help the selection of a suitable technique for this investigation.

5.2.1 Air-cored induction coil sensor

The air-cored induction coil is also known as the H-coil. It is one of the simplest methods for an accurate measurement of the surface magnetic field of an electrical steel specimen [5.22]. The principle of the method is based on Faraday's law which is described in section 5.1.1.

A typical H-coil sensor is made by winding an on a non-magnetic former having $\mu_r \approx 1$. The induced emf in the coil is proportional to the time varying magnetic flux density dB/dt since there is a linear relation between B and H in the air, from equation 5.3 the induced emf in the coil can be expressed as

$$emf = -\mu_0 NA \frac{dH}{dt} \tag{5.14}$$

where N is the number of identical turns on the H-coil. Thus, rearranging the above equation and giving the magnetic field H inside the coil as

$$H = -\frac{1}{\mu_0 NA} \int (emf) \bullet dt \qquad (5.15)$$

An example of the use of an H-coil is shown in figure 5.9. The H-coil sensor, which is made by winding enamelled copper wire on a thin polymer sheet, is placed on the test specimen. The magnetic boundary conditions [5.23] states that at the interface between two materials of different magnetic permeabilities ($\mu_{polymer}$ and μ_{steel}), the tangential component of the field continuous across the boundary. Therefore, the field measured by the H-coil placed at near surface of the specimen can be assumed to be equal to the tangential component of field within the test specimen.
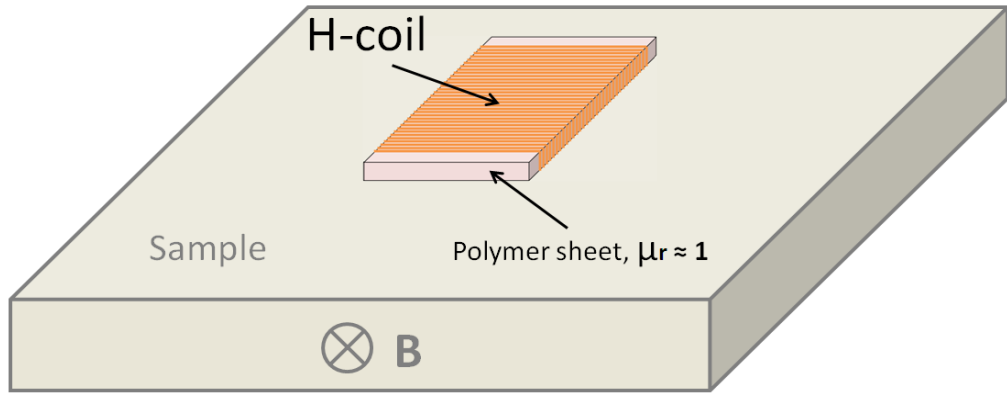
Figure 5.9 Illustration of H coil on an electrical steel sample.

5.2.1.1 Previous related investigation using the H- coil method

Pfützner [5.24] proposed a lift coil method to improve the accuracy of the H-coil sensor. The author stated that the magnetic field above any grain oriented electrical steel specimens is inhomogeneous and varying by distance due to the influence of the local demagnetising field (first proposed by Moses [5.25]). An experiment was set up to study the variation of the surface magnetic field on electrical steels. The magnetic field was measured at 1.5 mm and 3.0 mm above the test specimen by lifting an H-coil sensor. The lift coil method as described in this paper has improved consistency over the two H-coil method mentioned by Nakata [5.26]. Results showed that the field increased by a maximum of 7% at 3.0 mm

compared to that measured at 1.5 mm. This agreed with the proposal [5.27] made earlier by the authors. In addition, by using linear mathematical extrapolation, the lift coil method can be using for the calculation of the magnetic field within any test specimen.

Later, Tumanski [5.28] also studied the variation of the magnetic field as a function of distance above a grain oriented electrical steel strip. His study consists of both numerical and experimental investigations, in which the experimental result was obtained through averaging local field strength using a magnetovision map [5.29]. The test strip were magnetised in turn by single yoke and double yoke systems. Figure 5.10 shows the distribution of the magnetic field as a function of distance above the test specimen. The double yoke system for magnetising specimens was strongly recommended by the authors (as discussed in 5.1.2). For the double yoke system, the authors explained the sudden increase in magnetic field strength at the near surface was caused by the distortion of a stray field from domains and grain boundaries. As a result, when the double yoke construction is used for magnetising the specimen, the field sensor should be placed at approximately 1 mm above the test specimen to avoid the influence of the stray field. (No further explanation was given by the authors on the significance of the effect).
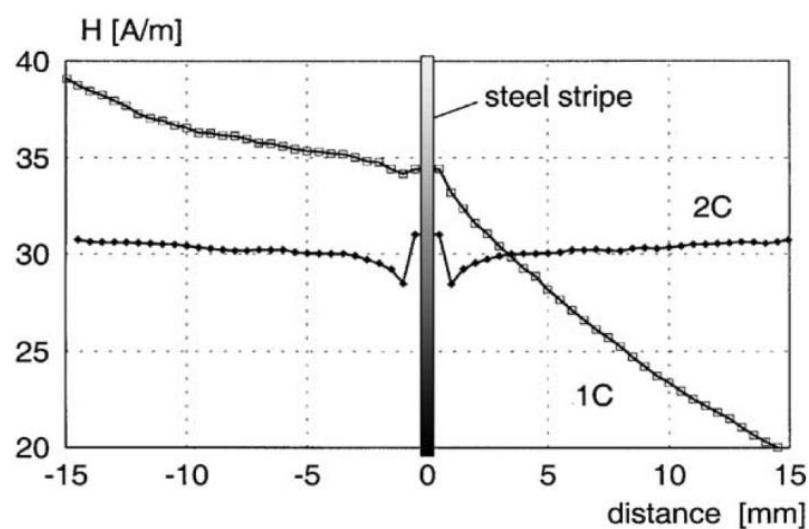

Figure 5.10 The dependence of the magnetic field above the sample surface versus distance from the sample magnetised by single yoke system 1C and double yoke system 2C [5.28].

5.2.2 Hall effect sensor

The Hall Effect sensor measures the magnetic field by applying the Hall Effect which was discovered by Edwin Herbert Hall In 1879. The Hall Effect states that when a plane of a current carrying conductor is placed perpendicular to the direction of a magnetic field, an electric potential V_H (as shown in figure 5.11) will arise in the plane of the current carrying conductor and perpendicular to the direction of the current. Figure 5.11 displays the configuration of the vectors of the Hall Effect.
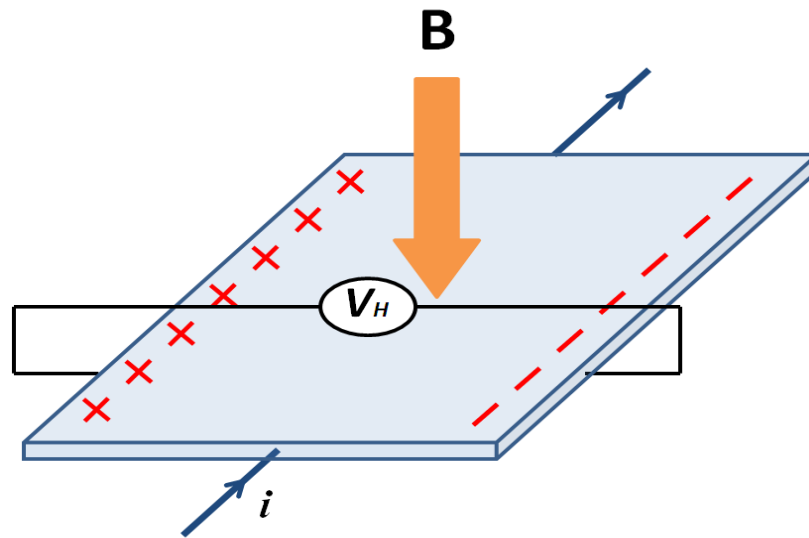
Figure 5.11 Illustration of the Hall Effect.

A typical Hall Effect sensor consists of a rectangular semiconducting plate with two pairs of electrical contacts at right angle to each other [5.22]. During the measurement, a DC current is conducted via one pair of the contacts. If the magnetic field perpendicular to the semiconducting plate is not zero, then the movement of electrons is distorted (left hand rule and Lorentz force law). As a result, an electrical potential is formed transverse to the current direction. The induced Hall voltage is proportional to the product of magnetic field strength and the current.

To improve the sensor sensitivity, Hall sensors made of thin plate of low-carrier-concentration semiconductor are usually preferred since the Hall voltage is inversely proportional to the thickness and carrier concentration of the plate.

Conductors such as Cu may be used, but compared with semiconductors such as indium arsenide (InAs), Cu has lower Hall coefficients. In addition, InAs has low temperature sensitivity therefore is less influenced by the surrounding environment.

In terms of the fabrication, modern Hall sensors are made of integrated circuits [5.30] for reduced capital cost and improved product quality. Commercial sensors are relatively cheap compared with H-coil sensors and their geometries and size are designed for specific applications.

5.2.2.1 Previous related investigation using Hall sensor

The earliest examples utilising the Hall sensor for magnetic field measurement on a steel sample were conducted by Evans and Peeve [5.31]. In the study, by assuming the magnetising field distributes uniformly across the entire specimen, the magnetic field applied to the specimen was measured by a Hall Effect sensor which was placed in the pre-drilled hole in the test specimen.

Moses [5.32] conducted an experiment to study the distribution of the surface field on a grain oriented steel sample using a Hall effect integrated circuit sensor. The sensor was calibrated in a uniform magnetic field, which was created by a DC current carrying solenoid, a sensor sensitivity of 0.03 mV/Am^{-1} was found. In the measurement, the magnetic field of the specimen was sensed by placing the Hall Effect sensor 0.25 mm above the specimen.

Stupakov [5.33] measured surface field strength of an electrical steel sample using Hall Effect sensors with build in high-gain amplifier. Such sensors allow a localised magnetic field to be measured at a very low strength. Figure 5.12 shows the B-H loop obtained from the Hall sensor measurement. The author explained that the distortion appearing on the loop is due to the thermal noise which influences the stability of the sensors. The presence of the thermal distortion can directly affect the accuracy of the measurement and must be improved. One of the more useful methods for the removal of the thermal distortion seen on the B-H loop was by averaging over a high number of cycles. An example of a noise

improved B-H loop is seen by the red dash line in figure 5.12. The loop is obtained by averaging out 30 continuous magnetisation cycles.

The author also claimed that the Hall sensor was not the best choice for magnetic field measurement because of its high-noise output, but it is capable of obtaining a result and could encourage further research on producing low-noise and low-field sensors in the future. Despite its disadvantages, the use of the Hall sensor over the classical sensors such as the H-coil and the Rogowski-Chattock potentiometer [5.34] are due to the simplicity and the variety in geometry. Furthermore, Hall Effect sensors in general have a small sensing area which makes them capable of sensing localised field, the use of the Hall Effect sensors could improve the overall resolution of the localised measurements.
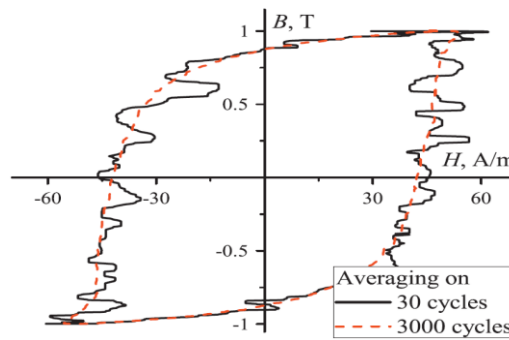
Figure 5.12 B-H loops of a non-oriented steel sample measured by the Hall sensor on cycles averaging 30 and 3000 [5.33].

5.3   Local power loss measurement methods

The power loss in electrical steels during AC magnetising process appears mainly in the form of heat, and the loss per magnetising cycle is proportional to the area of the B – H loop (see chapter 2). Therefore, the loss can be derived from the heat dissipated in a material or from the calculation of the area of the B-H loop.

5.3.1   Thermometric method

In the thermometric method, the heat generated by the steel sample is detected using thermometric sensors. The theory was explained by Gilbert [5.35]. If heat is generated at a point in a material under a steady-state condition, the initial

rate of the rise of the temperature at this point is proportional to the generated heat. Based on this theory, the power loss **P** of electrical steel can be expressed as [5.36]

$$p = c_p \frac{dT(t)}{dt} + k_{ext}[T(t) - T_0] \qquad (5.16)$$

where P is the thermal power loss has units of Joules (J), C_p is the specific heat of the test sample and has units of Joules per Kilogram per Kelvin (J/KgK) and dT is the change in temperature of the measured point over a period of dt seconds. K_{ext} is the heat transmission coefficient (to the surroundings) has unit of Watts per kilogram per Kelvin (W/kgK), and T_0 is initial temperature of material and surrounding before being magnetised.

For power loss localised measurements, Gilbert [5.35] suggested that the initial time taken to measure the rate of the temperature rise should be less than 10 seconds, above which the method rate of rise of temperature becomes non-uniform due to heat diffusion. This time should vary to some extent depend on thermal diffusion rate of the material.

Moses [5.38] measured power loss distribution in a stator core using thermistors. The initial temperature rise was recorded for a period of 20 seconds, and the experimental error was estimated to about ± 8 %.

Hamzehbahmani [5.39] compared local power loss measurement techniques and developed a system for loss measurement based on the thermometric method; the author declared that their system was mostly suitable for the measurement of local losses at regions where distorted flux was found (i.e. around bolt holes and near burr regions), where the techniques for the measurement of localised magnetic field and flux density may fail.

However, the thermometric method was reported to have poor accuracy at low flux density. The method suffers from low signal to noise ratio. In addition, the

measurement resolution is low for this method due to the thermal diffusion lead to large sensing area (0.5 to 1 cm^2).

5.3.2 B – H loop

The theoretical bases and equations regarding the B-H loop method for loss calculation are outlined in chapter 2. This section focuses on the previous related works on the method.

Moghaddam [5.40] built a remote sensor to measure localised loss as shown in figure 5.13. The flux density was obtained using a designed remote search coil and the magnetic field was obtained using a magnetoresistive sensor. The sample was magnetised locally by the magnetising yoke which was mounted to a stepper motor. The error of a single point power loss measurement was estimated to be $\pm$ 5-6%. The authors claimed that if the configuration could be made smaller, the system would be capable of measuring power loss within grains of grain oriented steels. As discussed previously, such localised magnetisation system measures power loss at fixed flux density and does not reflect variation of local flux density which realistically occurs in grain oriented electrical steel; thus, is not suitable for the investigation of local flux density variation.
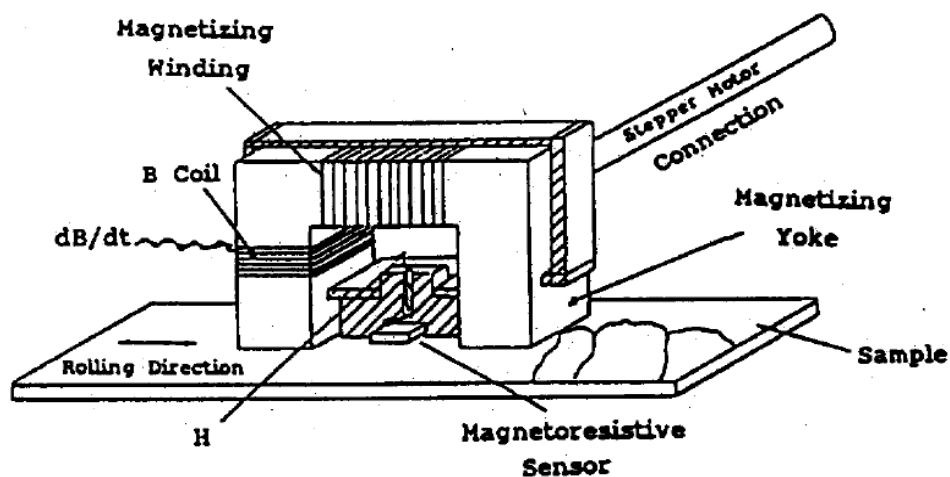
Figure 5.13 Illustration of the remote localised loss measurement sensor [5.40].

Enokizono [5.41-5.43] designed a two-dimensional loss measurement sensor, which consists of two pairs of orthogonally arranged needles with each pair

separated 15 mm apart and a 10 x 10 mm orthogonal H coil site in between the needles. The needles were loaded with springs to protect the specimens from contact damage during the magnetising vibration.

Senda [5.17] and [5.44] measured local power loss using a self-made probe shown in figure 5.14. A pair of tungsten needles 10 mm apart were arranged transverse to the sample rolling direction, and a Hall Effect sensor was placed between the needles.
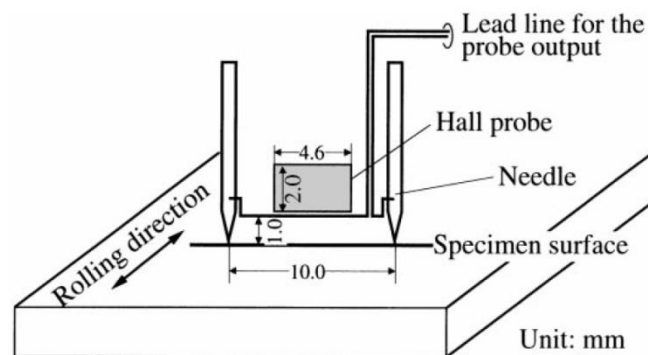
Figure 5.14 Illustration of the probe for local loss measurement [5.44].

In this investigation, a local loss measurement probe which consists of a pair of needles and an integrated Hall element was constructed for the measurement of local loss on grain oriented steel specimens. The output signals of B(t) and H(t) are substituted into equation 2.13 (see chapter 2) for the calculation of power loss. Further details regarding the signal processing are outlined in chapter 6.

References

[5.1]   D. Halliday, R. Resnick and K. S. Krane, "Physics", Wiley, New York, 4th Edition, vol. 2, pp. 784 – 785, (1992).

[5.2]   W. H. Hayt, "Engineering electromagnetics", McGraw-Hill, New York, 5th edition, pp. 312 – 313, (1989).

[5.3]   G. Loisos, "Novel flux density measurement methods of examining the influence of cutting on magnetic properties of electrical steels", Ph.D. thesis, Cardiff University, (2002).

[5.4]   D.J. Mapps, "Stress, power loss and domain structure in grain oriented silicon iron", Ph.D. Thesis, University of Cardiff, (1969).

[5.5]   F. Brailsford and V. R. Mazza, "Magnetic flux distribution in transformer laminations", Journal of the Institution of Electrical Engineers, vol. 8, pp. 552 – 553, (1962).

[5.6]   S. Tumanski, "The experimental verification of the condition of the magnetic material caused by different technological processes", Journal of Magnetism and Magnetic Materials, vol. 215 – 216, pp. 749 – 752, (2000).

[5.7]   S. Tumanski and M. Stabrowski, "The magnetovision method as a tool to investigate the quality of electrical steel", Meas. Sci. Technol, vol. 9, pp. 488 – 495, (1998).

[5.8]   S. Zurek, T. Meydan and A. J. Moses, "Analysis of twisting of search coil leads as a method reducing the influence of stray fields on accuracy of magnetic measurements", Sensors and Actuators, vol. 142, pp. 569 – 573, (2008).

[5.9]   G. Loisos and A. J. Moses, "Critical evaluation and limitations of localized flux density measurements in electrical steels", IEEE Transactions on Magnetics, vol. 37, pp. 2755 – 2757, (2001).

[5.10] H. Pfützner and G. Krismanić, "The needle method for induction tests: sources of error", IEEE Transactions on Magnetics, vol. 40, pp. 1610 – 1616, (2004).

[5.11] M. D. Wulf, L, Dupre, D. Makaveev and J. Melkebeek, "Needle-probe techniques for local magnetic flux measurements", Journal of Applied Physics, vol 93, pp. 8271 – 8273, (2003).

[5.12] E. Czeija and R. Zawischa, Austrian Patent 180990, (1955).

[5.13] L. H. Stauffer, U.S. Patent 2828467, (1958).

[5.14] R. E. Tompkins, L. H. Stauffer and A. Kaplan, "New magnetic core loss comparator", Journal of Applied Physics, vol. 29, pp. 502 – 503, (1958).

[5.15] F. J. Wilkins and A. E. Drake, "Measurement and interpretation of power losses in electrical sheet steel", Proc. IEE, vol. 112, pp. 771 – 785, (1965).

[5.16] W. Brix, K. A. Hempel and F. Schulte, "Improved method for the investigation of the rotational magnetisation process in electrical steel sheets", IEEE Transactions on Magnetics, vol. 20, pp. 1708 – 1710, (1984).

[5.17] W. Brix, K. A. Hempel and W. Schroeder, "Method for the measurement of rotational power loss and related properties in electrical steel sheets", IEEE Transactions on Magnetics, vol. 18, pp. 1469 – 1471, (1982).

[5.18] K. Senda, M. Ishida, K. Sato, M. Komatsubara and T. Yamaguchi, "Localised magnetic properties in grain-oriented electrical steel measured by needle probe method", Electrical Engineering in Japan, vol. 126, pp. 942 – 949, (1999).

[5.19] T. Nakata, K. Fujiwara, M. Nakano and T. Kayada, "Influence of yoke construction on magnetic characteristics of single sheet tester". Journal Japanese Society Applied Magnetism, vol. 13, pp. 371 - , (1989).

[5.20] G. Crevecoeur, L. Dupre, L. Vandebossche and R. Van de Walle, "Local identification of magnetic hysteresis properties near cutting edges of electrical steel sheets", IEEE Transactions on Magnetics, vol. 44, pp. 1010 – 1013, (2008).

[5.21] G. Crevecoeur, L. Duper, L. Vandenbossche and R. Van de Walle, "Reconstruction of local magnetic properties of steels by needle probe methods using space mapping techniques", Journal of Applied Physics, vol. 99, pp. 08H905-1 – 08H905-3, (2006).

[5.22] R. Boll and K. J. Overshott, "Sensors: Volume 5 Magnetic Sensors", VCH Publishers Inc., New York, p.206, (1989).

[5.23] R. G. Carter, "Electromagnetism for electronic engineers", 2nd edition, Chapman & Hall, London, (1992).

[5.24] H. Pfützner and P. Schönhuber, "On the problem of the field detection for single sheet testers", IEEE Transactions on Magnetics, vol. 27, pp. 778 – 785, (1991).

[5.25] A. J. Moses, "Recent advances in experimental methods for the investigation of silicon iron", Physica Scripta, vol. T24, pp. 49 – 53, (1988).

[5.26] T. Nakata, Y. Kawase and M. Nakano, "Improvement of measuring accuracy of magnetic field strength in single sheet testers by using two H Coils", IEEE Transactions on Magnetics, vol. Mag-23, pp. 2596 – 2598, (1987).

[5.27] H. Pfützner, "Application of hall sensors in comparison to other methods of field detection for investigations of electrical steel", Z. el. Inform. U. En. Techn., vol. 10, pp. 534 – 546, (1980).

[5.28] S. Tumanski, "A multi-coil sensor for tangential magnetic field investigations", Journal of Magnetism and Magnetic Materials, vol. 242 – 245, pp. 1153 – 1156, (2002).

[5.29] S. Tumanski and M. Stabrowski, "The magnetovison method as a tool to investigate the quality of electrical steel", Measurement Science and Technology, vol. 9, pp. 488 – 495, (1998).

[5.30] S. A. Macintyre, "Magnetic Field Measurement", CRC Press LLC, (1999).

[5.31] D. Evans and P. A. Reeve, "Automated high saturation B-H measuring equipment", IEEE Transactions on Magnetics, vol. 32, pp. 3045 – 3048, (1996).

[5.32] A. J. Moses and S. N. Konadu, "Some effects of grain boundaries on the field distribution on the surface of grain oriented electrical steels", International Journal of Applied Electromagnetics and Mechanics, vol. 13, pp. 339 – 342, (2002).

[5.33] O. Stupakov, "System for controllable magnetic measurement with direct field determination", Journal of Magnetism and Magnetic Materials, vol. 324, pp. 631 – 636, (2012).

[5.34] A. Khanlou, A. J. Moses, T. Meydan and P. Beckley, "A computerised on-line power loss testing system for the steel industry, based on the RCP

compensation technique", IEEE Transactions on Magnetics, vol. 31, pp. 3385 – 3387, (1995).

[5.35] A. J. Gilbert, "A method of measuring loss distribution in electrical machines", The Institution of Electrical Engineers, vol. 108, pp. 239-244, (1961).

[5.36] H. Hamzehbahmani, A. J. Moses and F. J. Anayi, "Opportunities and precautions in measurement of power loss in electrical steel laminations using the initial rate of rise of temperature method", IEEE Transactions on Magnetics, vol. 49, pp. 1264 – 1273, (2013).

[5.37] B. D. Ismail, "Investigation of flux and loss distribution in transformer cores assembled from amorphous powercore material", Ph.D. thesis, University of Wales College Cardiff, (1991).

[5.38] A. J. Moses and N. Tutkun, "Localised losses in stator laminations of an induction motor under PWM excitation", Journal of Materials Processing Technology, vol. 161, pp. 79 – 82, (2005).

[5.39] H. hamzehbahmani, A. J. Moses and F. J. Anayi. "Opportunities and precautions in measurement of power loss in electrical steel laminations using the initial rate of rise of temperature method", IEEE Transactions on Magnetics, vol. 49, pp. 1264 – 1273, (2013).

[5.40] A. J. Moghaddam and A. J. Moses, "Localised power loss measurement using remote sensors", IEEE Transactions on Magnetics, vol. 29, pp. 2998 – 3000, (1993).

[5.41] M. Enokizono, I. Tanabe and T. Kubota. "Localized distribution of two-dimensional magnetic properties and magnetic domain observation", Journal of Magnetism and Magnetic Mmaterials, vol. 196 – 197, pp. 338 – 340, (1999).

[5.42] M. Enokizono, M. Morikawa, K. Kawamura and J. Sievert. "Distribution of two-dimensional magnetic properties in three-phase induction motor model core", IEEE Transactions on Magnetics, vol. 32, pp. 4989 – 4991, (1996).

[5.43] T. Kanada, M. Enokizono, K. Kawamura and J. D. Sievert. "Distributions on localised iron loss of three-phase amorphous transformer model core by

using two-dimensional magnetic sensor", IEEE Transactions on Magnetics, vol. 32, pp. 4797 – 4799, (1996).

[5.44] K. Senda, M. Kurosawa, M. Ishida, M. Komatsubara and T. Yamaguchi. "Local magnetic properties in grain-oriented electrical steel measured by the modified needle probe method", Journal of Magnetism and Magnetic Materials, vol. 215 – 216, pp. 136 – 139, (2000).

Chapter 6

Experimental Apparatus

This chapter describes the apparatus used for observation of magnetic domain and the local loss measurement system used for the measurement of localised flux density, magnetic field and power loss of grain oriented electrical steels. The method for evaluation of uncertainty in the measurements is also outlined in this chapter.

6.1 Apparatus for the observation of magnetic domains of electrical steel samples.

6.1.1 Static domain imaging using magnetic domain viewer

A magnetic domain viewer based on the modified Bitter technique outlined in chapter 4 was used in this investigation for the study of grain structure and the static magnetic domain pattern of electrical steel specimens.

Figure 6.1 shows the magnetic domain viewer with 90 mm diameter observation area which was used in this investigation. This domain viewer consists of a circular-shaped clear plastic body, a build-in magnetic coil, a Bitter fluid injection port, lead wiring to an external DC power supply, a plastic film membrane and the Bitter fluid (a mixture of fine Fe_2O_3 particles, soap and distilled water).

The coil is wound along the ring-shaped groove of the viewer body as seen in figure 6.2. An external DC power supply is connected to the coil for the generation of a magnetic field of approximately 2.2 KAm^{-1} [6.1] perpendicular to the surface of the test specimen. Grain oriented electrical steel is rarely perfectly oriented; a small tilt angle is expected to form during the coil annealing process (also known as the secondary recrystallisation). Therefore, as shown in figure 6.2, magnetisation of one type domain (e.g. N-S domain) will rotate towards the surface plane and the other type domain (e.g. S-N domain) will rotate away from the surface plane. As a result, stray field profile of the viewing specimen is modified, more ferromagnetic particles are attracted by the S-N domains and less is attracted by the N-S domain. Thus, a black and white contrast is developed by the black ferromagnetic particles and the white background membrane, which indicates the anti-parallel bar domains of the grain oriented electrical steel.
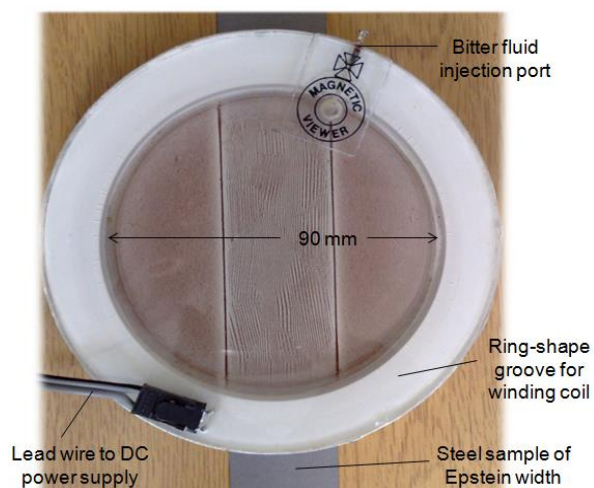

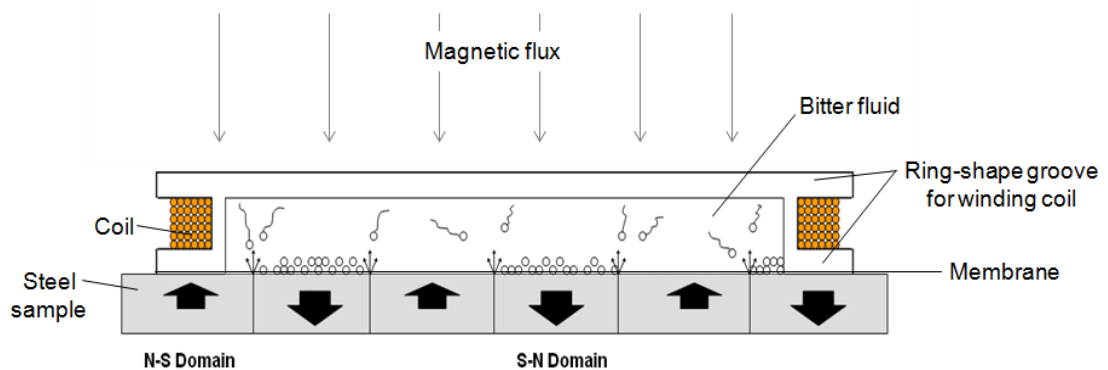**Figure 6.1** Photograph of the magnetic domain viewer which was used in this investigation.

Figure 6.2 Cross-section illustration showing the working principle of the magnetic domain viewer.

73

Application of the external field improves the Bitter pattern contrast. In addition, the contrast of the image was further boosted through the use of Photoshop Pro image editing software.

6.1.2   Dynamic domain imaging using Magneto-optical Kerr microscope.

Figure 6.3 shows the low magnification Kerr microscopy system used in this investigation. The system consists of three separate sections, the light source, magnetising and collection.

The light source section – this consists of a Schott KL1500 LCD light source, an optical cable and a plane polariser.

The magnetising section – this consists of an adjustable sample stage, a coil wound C-shape yoke of 20 mm pole separation spacing, a TTi 40 MHz arbitrary wave generator and an Amcron DC 300 A amplifier.

The collection section – this consists of a low magnification lens, a Kerr Effect analyser, a Photron fastcam MC1 camera and DpxView Pro camera software installed prior in the PC. Specification of the camera is shown in table 6.1.

Dimensions (camera head)	Weight (head)	Sensor type	Resolution	Frame rate	Recording memory	Trigger method
35 (W) x 35 (H) x 33.3 (D) mm	90 g	CMOS	512 x 512 pixels	2,000 fps (up to 10,000 with reduced resolution)	2 GB	Start, centre and end

Table 6.1 Manufacture specification of the Photon fastcam MC1 high speed camera [6.2].
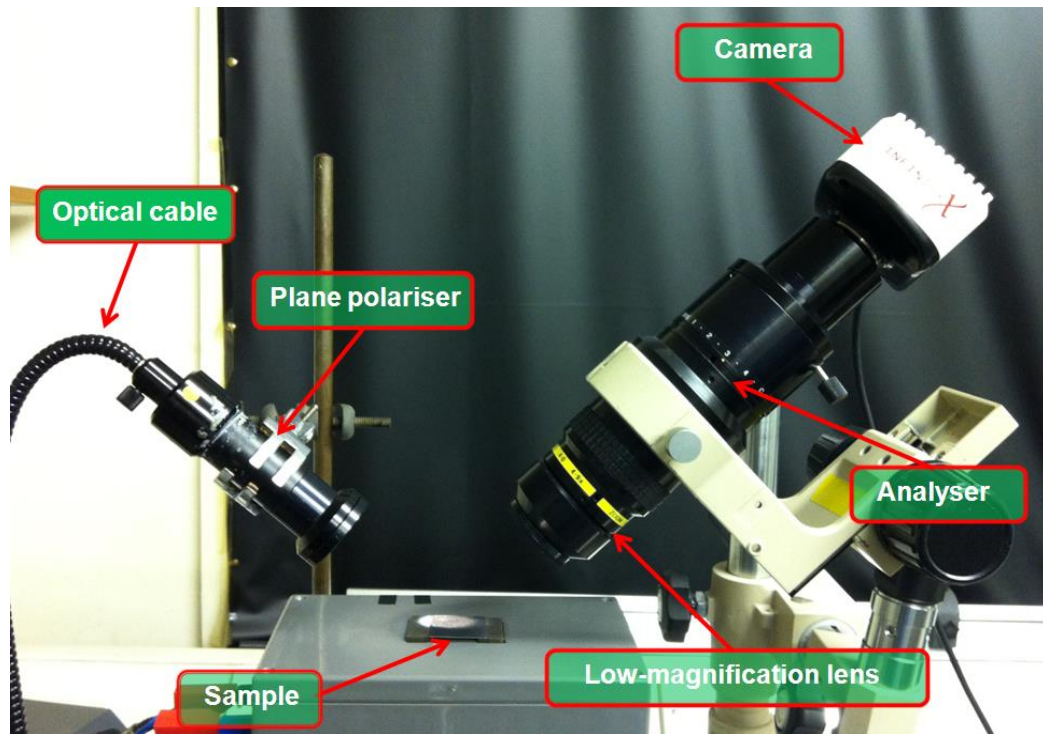
Figure 6.3 Photograph of the low magnification Kerr microscope.

A high intensity light beam was produced by the Schott KL1500 LCD light source, which was then focused and directed to the plane polariser using the optical cable shown on the left side of figure 6.3. The beam was then passed through the polariser to make polarised light which illuminates the test specimen. The reflected beam with a polarisation angle of $+\theta_k$ or $-\theta_k$ (outlined in chapter 4.4) travelled through the magnification lens and the analyser to form the Kerr contrast which was captured by the camera. During the observation, the angle of incidence/reflection was adjusted to approximately 50° to obtain optimum Kerr contrast [6.3].

To observe domain wall motion, a magnetic field waveform was produced by the TTi 40 MHz arbitrary wave generator, which was then fed into the Amcron DC 300A amplifier to gain the desired field strength. The magnetising field was applied to the test specimen through the coil wound C-shape yoke which sat underneath of the specimen.

6.2 Introduction to the system for the measurement of the local magnetic properties of the single strip electrical steel samples.

A computer-controlled AC magnetising and scanning loss measurement system was developed in the Wolfson Centre for Magnetics. The system is able to apply a global AC magnetising field to a single strip, Epstein size electrical steel specimen and measure its localised magnetic field, flux density and power loss in an area of up to 30 x 70 mm in the middle of the strip at a raster scanning resolution of up to 0.1 mm. It comprises three sub-systems: magnetising, measurement and positioning. The magnetising system magnetises the test sample at set magnetisation conditions, the measurement system is used to measure the globally induced magnetic flux density as well as detecting the localised magnetic flux density, magnetising field and power loss at the point where the sensor is located, and the positioning system is used to move the sensor between the measurement points.

Figure 6.4 shows how information is inter-exchanged in order to complete the measurement process. The positioning system communicates with the measurement system to identify whether the measurement has been finished and ready to relocate the sensor to the next measurement point. The measurement system feeds back the information regarding the flux density waveform to the magnetising system in order to control and accurately maintain the magnetisation conditions within the set tolerance (outlined in 6.2.1) so that each measurement is recorded at the same induced global magnetisation.
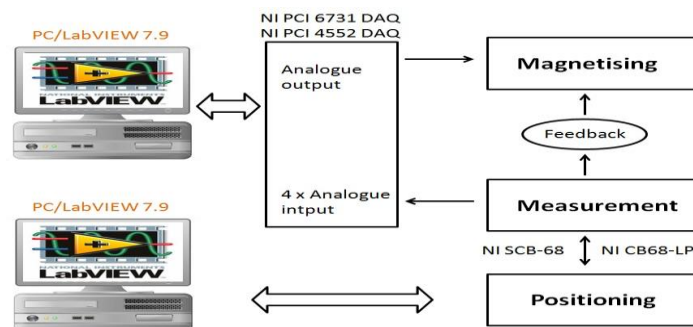

Figure 6.4 Schematic diagram of computer-controlled AC magnetising and scanning measurement system.

All systems were controlled through the computer controlled interface that utilised the laboratory virtual instrumentation engineering workbench (LabVIEW).

6.2.1 The magnetising system

A basic magnetising setup requires a signal generator to produce a constant AC waveform, an amplifier to increase the power of that waveform and a current carrying coil to generate a magnetic field.

However, such a simple system can often produce a varying field of unknown strength and a distorted waveform due to harmonic distortion in the system. In addition, if the coil was wrapped directly onto the sample there would be no space left for placing the measurement sensors. Therefore, an improved system for the magnetisation of single strip sample was constructed in this investigation, as illustrated in figure 6.5.
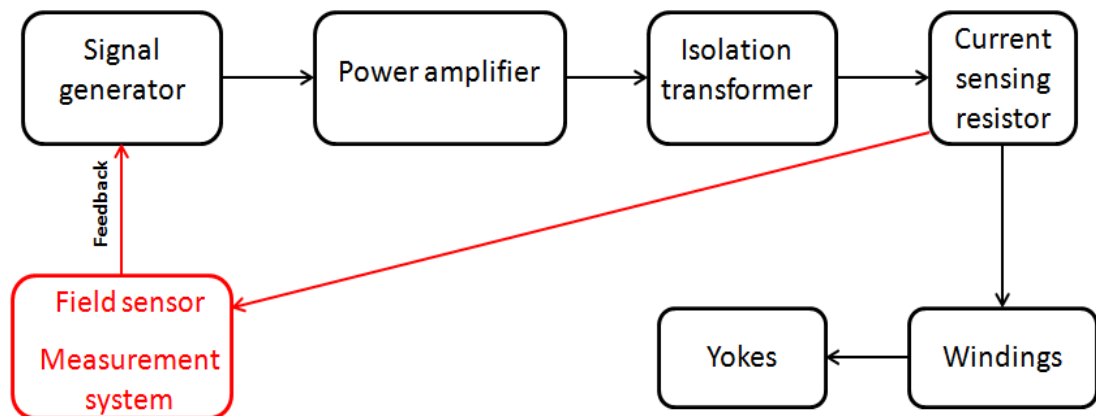
Figure 6.5 Flowchart showing the process of the magnetising system.

The magnetizing system shown in figure 6.5 consists of a personal computer (PC) with LabVIEW version 7.9 installed in advance, two data acquisition cards (DAQ) – NI PCI 6731 and NI PCI 4552, an AMRON DC 300 A series II laboratory power amplifier, an air-core isolation transformer, a 1 Ω current sensing resistor, and a double yoke apparatus having the configuration as seen in figure 6.6. Each yoke was made with laminated GO steels and with a wrapped coil of 200 turns. The dimension of the yoke is shown in figure 6.7.
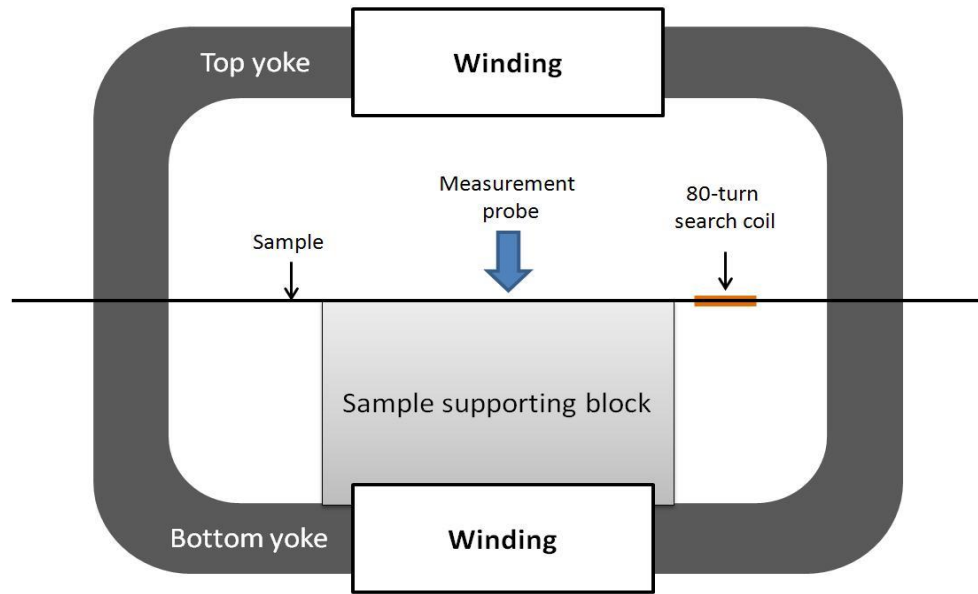
Figure 6.6 Schematic diagram of the magnetizing apparatus.
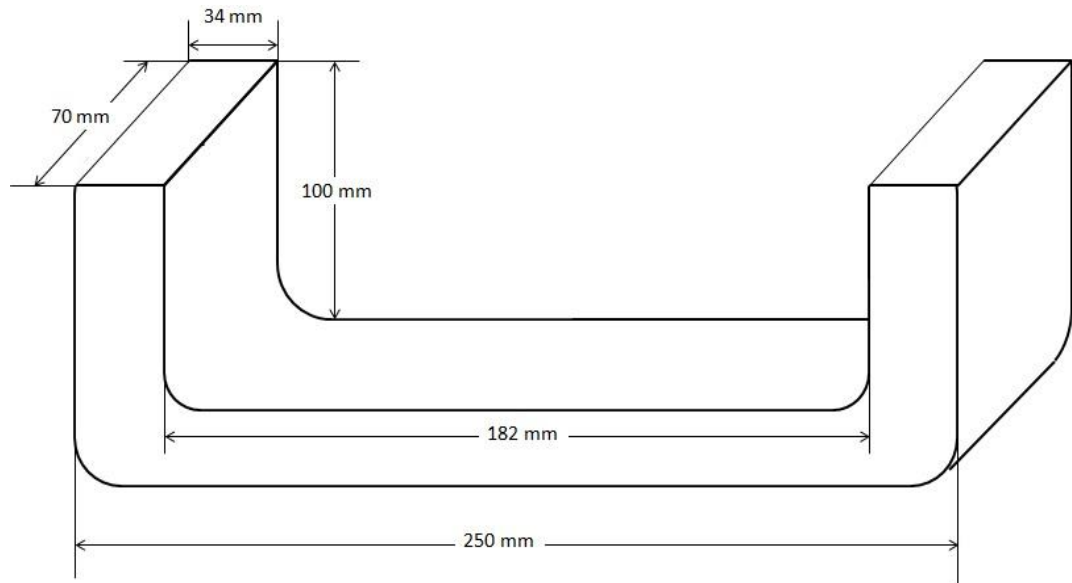
Figure 6.7 Schematic diagram showing the dimension of the yoke.

The magnetizing waveform and voltage were produced by the PC/ LabVIEW and NI PCI 6731 DAQ respectively, which were fed into the amplifier for the required field strength. The output voltage was passed through an air-core isolation transformer for the suppression of noise from the power supply. At this point, the voltage across the resistor of a known resistance was measured by the NI PCI 4552 DAQ which was used to calculate the current passing through the coil and to derive the field strength. The magnetizing field produced by the current carrying coil was passed through the specimen via the double yokes, thus creating space to enable

local measurements to be conducted. Moreover, the use of the double yoke configuration eliminates/cancels the in-plane eddy current formed at the poles of the yokes (discussed in chapter 5).

However, the field or flux density applied to the specimen cannot be derived by the field sensing resistor since the winding was not wrapped directly on the specimen. To solve this problem the overall flux density of the specimen was measured utilising a search coil that together constitutes the feedback (FB) system with the field sensing resistor. The information of the field collected by the FB system is used to compare it with the ideal field, and the differences will be adjusted by the NI PCI 6731 DAQ so that the measurement can be carried out within the set tolerance that was determined by the users via three main regulated control criteria displayed on the front panel on the PC. The three control criteria were the % error of peak flux density B_{peak} value, the total harmonic distortion (THD) and the form factor (FF) of the induced voltage in the search coil. The default values set for the three control criteria were 0.1%, 1.5% and 0.5% respectively. These were also upper limit values of the settings for all the measurements carried out throughout the investigations.

6.2.2   The measurement system

The measurement system comprises the LabVIEW program, an NI PCI 4552 DAQ, an 80 turn search coil, four transducers, a local loss measurement sensor and a Farnell stabilised DC power supply for operation of the local loss measurement sensor.

The 80 turn search coil was made by wrapping closely a single layer of 0.1 mm diameter wire on a plastic matrix of 31 (L) x 6 (W) x 0.5 (T) mm. The coil was placed next to the scanning area for measurement of the applied overall flux density.

A local loss measurement sensor was designed and calibrated for the measurement of the localised field H and flux density B, from which the power loss at the measurement point was calculated (see equation 2.12 and 2.13 in chapter 2).

The measurement probe consists of a square printed circuit board (PCB) containing two spring-loaded, 1.27 mm diameter phosphor bronze needles with an effective separation of 7 mm and a Honeywell SS495A linear Hall Effect sensor with an effective sensing span of 2 mm mounted between the needles, as illustrated in figure 6.8 (a). In addition, an orthogonal needle probe, that made of the same type of needles at the same 7 mm needle span as illustrated in figure 6.8 (b), was build for the measurement of component of flux density in both rolling direction (RD) and transverse direction (TD) in the test specimens in this investigation.
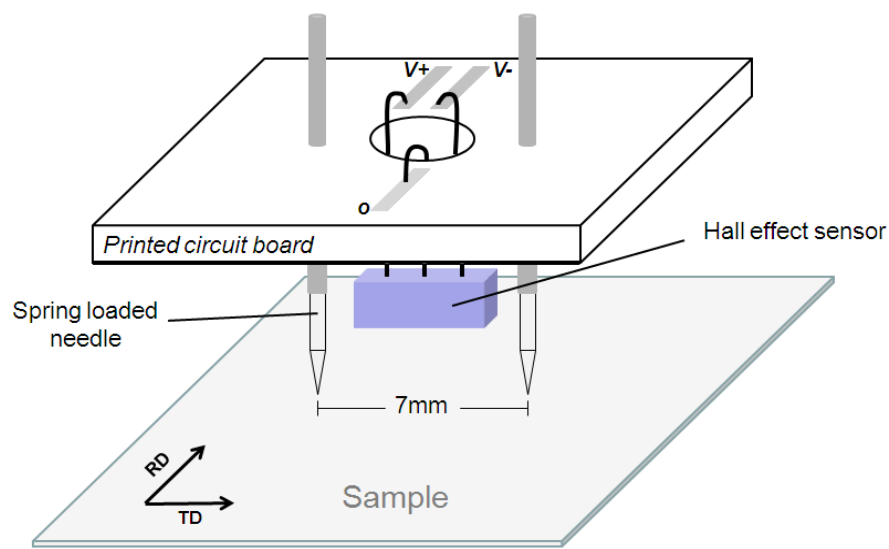
(a)
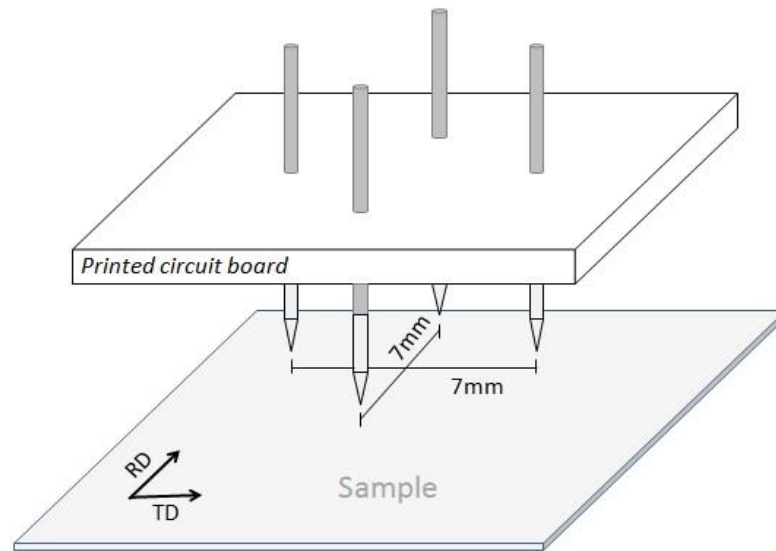
(b)

Figure 6.8 Illustration of the (a) localised loss measurement sensor and (b) orthogonal needle probe.

The design of making needles 7 mm apart is to provide the capability of measurement of localised flux density within grains of HGO steel with reasonable needle span to sample thickness ratio to meet the second assumption (see 5.1.2). Calibration of the needle probe is detailed in the later chapter 8.3, where the needle probe is compared with a single turn search coil for the measurement of localised flux density on a HGO steel.

During the measurement, the distance between the sensing element in the Hall Effect sensor and the sample surface was controlled by the positioning system and was maintained at approximately 0.5 mm above the test sample. The spring loaded needles were used to ensure continuous contact when the sample was vibrating during magnetisation to avoid the loss of signals. The instantaneous flux density B(t) was calculated from the instantaneous output voltage V(t) of the needle probe by using the equation derived from 5.13, as shown below

$$B(t) = \frac{V(t)}{2Af} \quad \text{(T)}$$

The tangential component of instantaneous field H(t) along the magnetisation direction was derived from the instantaneous output voltage V(t) of the linear Hall Effect sensor operated at 5 V input DC current. The equation is shown below

$$H(t) = CV(t) \text{ (A/m)}$$

where C is the scaling factor of the Hall effect sensor.

The localised loss measurement sensor was placed securely in an aluminium cantilever fixed on the positioning system, making it possible to scan the area of interest. For example, to scan an area of 10 x 10 mm on the surface of a test specimen with desired scanning resolution of 2 mm, as shown in figure 6.9. The sensor is set to measure localised B and H of the 36 points in the number order. It should be noted that each localised B measurement is an average of flux density in between the 7 mm needle span, and each localised H measurement is an average of

magnetising field over the 2 mm area where the Hall sensor is located. The results of measurements can be used to make contour map that showing the distribution of localised B and H over this 10 x 10 mm scanning area.
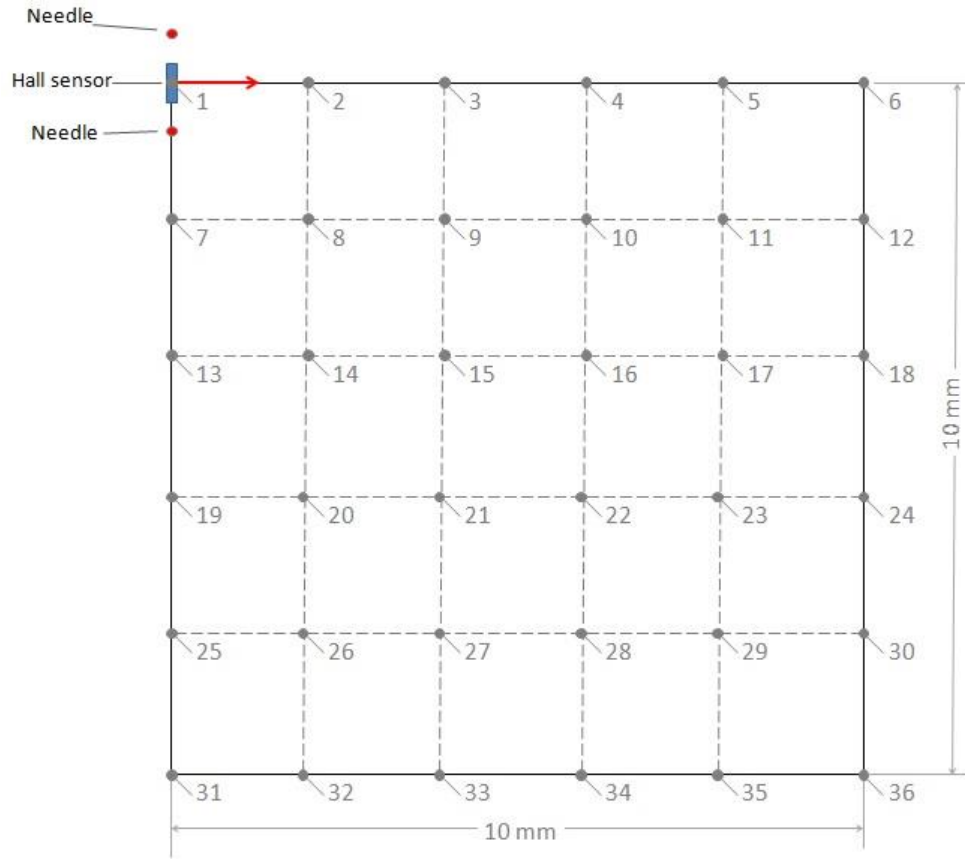
Figure 6.9 Illustration of the process of scanning B and H measurements using the localised loss sensor over a 10 x 10 mm surface area at 2 mm sampling intervals.

6.2.3   The positioning system

The positioning system consists of a PC/LabVIEW program, two interface units (NI SCB-68 and NI CB68-LP), a Parker Daedal cross roller series positioner and a self-made aluminium cantilever with a sensor holder at its free end shown in figure 6.10. The positioning system was a completely separate system and only communicated with the measurement system through a bridge created by the interface units. Therefore, when scanning a specimen, the correct VIs (the 'Scanning local-loss' VI for measurement and 'Scanning position' VI for positioning) must run on both PCs simultaneously.

Lead wire exit

Loss probe holder

Aluminum cantilever

3D view

280 mm

20 mm

40 mm

65 mm

Side view

37 mm

20 mm

30 mm

80 mm

Bottom view
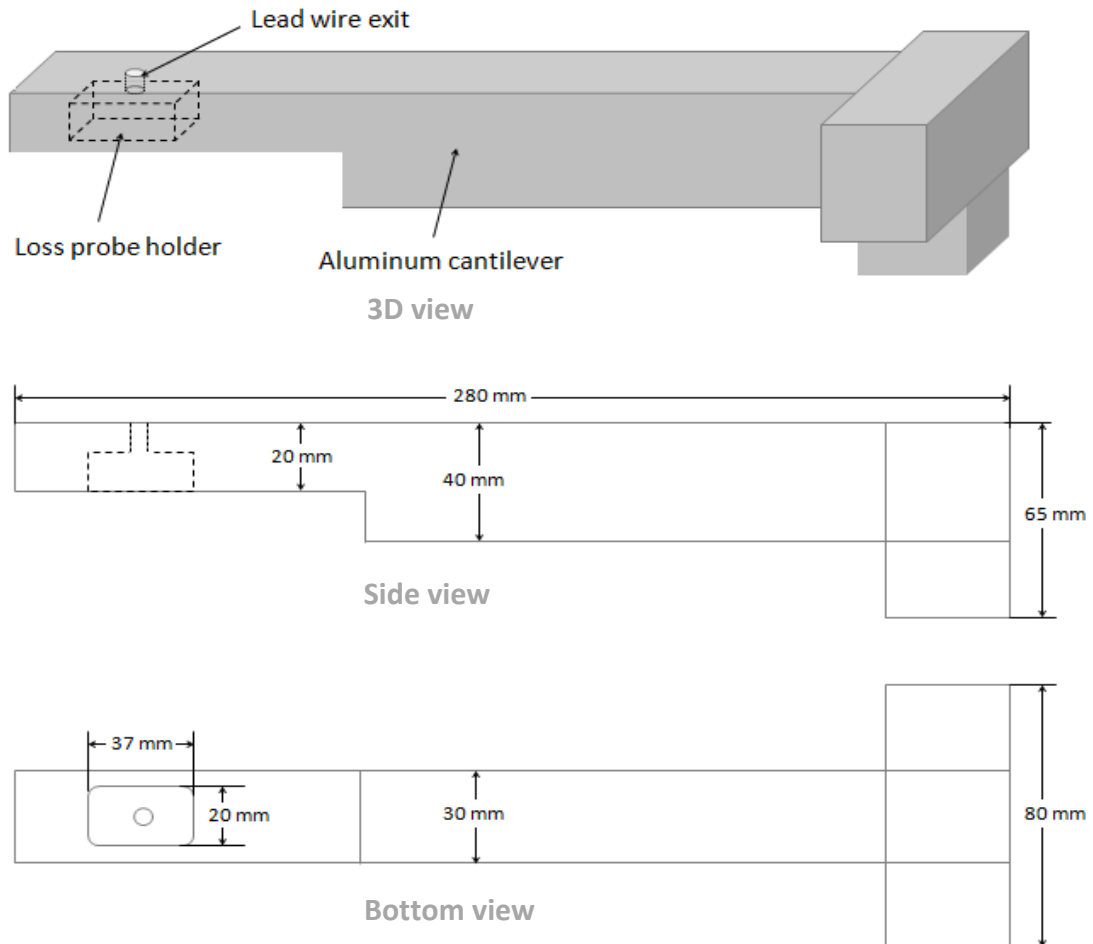
Figure 6.10 Dimension of the cantilever.

The Paker positioner is able to move in the three axes labelled X, Y and Z on the stepper motors and the VI program was set to raster scan samples automatically from left to right and top to bottom. The sampling rate or scanning resolution can be set using the dx and dy controls on the VI's front panel. The starting position, point 0 as indicated in the scanning position VI, can be chosen by the users through a separate VI program. Once the measurement is completed at the first point, the cantilever/sensor is lifted by the Z motor, and then moved to the next point and lowered to the same height so that the measurement can be repeated; this process continues until the required number of moves has been performed.

A dataflow diagram showing the measurement procedure is shown in figure 6.11. To start the test, the loss measurement VI reads the information regarding the three criteria (% error of peak flux density value, THD and FF) for the overall flux

density waveform that needs to be generated. Next, the B waveform is generated through the VI and NI PCI 6731 DAQ card, which is measured by the 80 turn search for feedback the actual B waveform induced on the test specimen. If any of the three criteria were out of the set tolerance, then the magnetising voltage is adjusted by the VI to meet the tolerance. Otherwise, the localised measurements should start taking place. An averaging of 15 continuous localised measurements were carried out for each measurement point to minimise the effect of any noise distortion hence improve the measurement repeatability [6.4]. The criteria are constantly monitored by the feedback system until the averaging process has finished and saved. The positioning system then moves the sensor to the next point and averages the results. The process is repeated until the measurement of the last point has been completed. The measurement data was finally saved in a spread sheet.
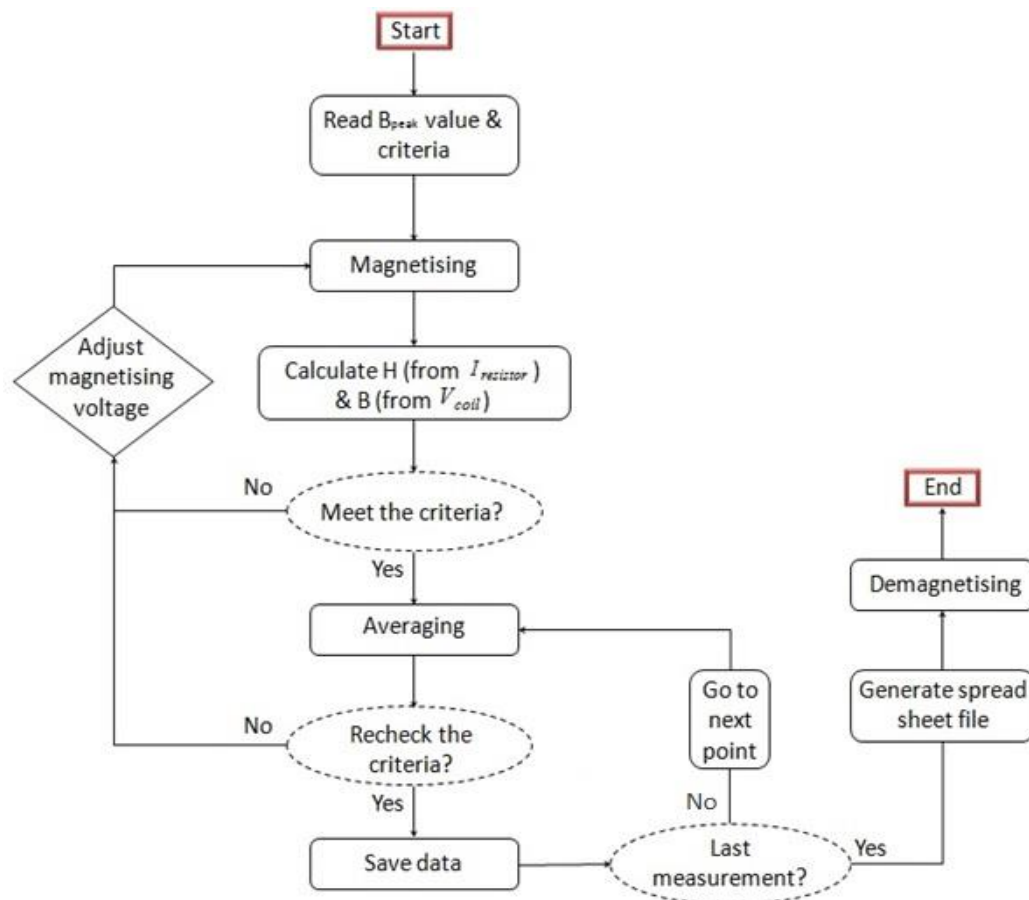
Figure 6.11 Flowchart of VI program for measurement of local magnetic properties.

6.3   Uncertainty analysis

Measurement uncertainty is an evaluation of the interval of the result of the measurement that describes how far the true value may differ from the result. Analysis of the measurement uncertainty provides a level of confidence to a measurement result.

In this investigation, all values of uncertainty were evaluated based on the method stated in UKAS M3003 [6.5]. The sources of uncertainty need to be converted into the same unit and at the same level of confidence before merging; this was done by using the standard uncertainties u. There are two types of evaluation for estimating the u values: 'type A' and 'type B' evaluations. Type A is a statistical method (e.g. from repeated measurements) whereas type B is a systematic method (e.g. from past experience of the measurements, published certificates, specifications provided by manufacturer and etc.).

In general, the estimated output quantity y, or the measurand, is affected by a number (n) of influence quantities x by the mathematical relationship given as

$$y = f(x_1, x_2, \dots x_n) \tag{6.1}$$

For type A evaluation, the standard uncertainty $u_A(y)$, is derived from standard deviation s by the following equation

$$u_A(y) = \frac{s}{\sqrt{n}} \tag{6.2}$$

where s is expressed as

$$s = \sqrt{\frac{\sum_{i=1}^{n}(q_i - \bar{q})^2}{n-1}} \tag{6.3}$$

and q_i is the measured value of y and $\bar{q}$ is the arithmetic mean of y. $\bar{q}$ is expressed as

$$\bar{q} = \frac{1}{n}\sum_{i=1}^{n} q_i \tag{6.4}$$

For type B evaluation, the components of uncertainty are represented by the standard uncertainties of the measurement input x_i and the output standard uncertainty $u_B(y)$ is expressed as

$$u_B^2(y) = c_1{}^2 u^2(x_1) + c_2{}^2 u^2(x_2) + \cdots + c_n{}^2 u^2(x_n) \tag{6.5}$$

where c_i $(c_1, c_2, …, c_n)$ is the sensitivity coefficient associated with each input x_i and is the partial derivative of the model function with respect to the input. Thus,

$$c_i = \frac{\partial y}{\partial x_i} \tag{6.6}$$

In the case of magnetic measurements the exact function relationship of the measurement is unknown, i.e. c_i cannot be derived mathematically so c_i is estimated by means of experimental method, from determination of $\partial y/\partial x_i$ by changing the value of x_i.

The uncertainty after summation in quadrature of individual standard uncertainties as calculated by type A and type B evaluation is the combined uncertainty $u_c(y)$, and is expressed as

$$u_c(y) = \sqrt{u_A^2(y) + u_B^2(y)} \tag{6.7}$$

The combined uncertainty estimated from the above equation is considered at confidence level of 68%. This uncertainty can be expanded at other levels of confidence by multiplying the coverage factor k. Most commonly, the expended uncertainty U is given at confidence level of 95%, by the expression

$$U(y) = k_{95} u(y) \tag{6.8}$$

Thus, the final result of the measurement of $y(y_i)$ can be represented as

$$y = y_i \pm U(y) \tag{6.9}$$

For type A evaluation, uncertainty is estimated by the arithmetic mean of n independent measurements. The number of degrees of freedom v_i is $n - 1$. On the other hand, v_i of type B evaluation is often infinity since its value has very high degree of variability. The effective degree of freedom v_{eff} of the combined standard uncertainty is demand for determination of the coverage factor k from the t-distribution table. E.g. when $v_{eff} \to \infty$, $k_{95} = 2$.

Table 6.2 shows the uncertainty budget of the local B$_{peak}$ measurement. Sources of uncertainty of those estimated from manufacture specification were the expanded uncertainties obtained by multiplying $k_{95} = 2$. Thus, these values were divided by two before merging to unify the level of confidence with other contributions listed in the table. Sources of uncertainty of those estimated from the measurement apparatus were classified into rectangular distribution, with the associated divisor of $\sqrt{3}$.

Sources of uncertainty	Value $\pm\%$	Type of distribution	Divisor	c_i	$u(x_i)\pm\%$	v_i or v_{eff}
Repeatability of local B$_{peak}$ measurement (Type A evaluation)	0.100	Normal	2	1	0.0500	2
Accuracy of NI PCI-6731 DAQ	0.023	Normal	2	1	0.0115	∞
Frequency setting	0.010	Normal	2	1	0.0050	∞
Mass measurement	0.010	Normal	2	1	0.0050	∞
Needle span measurement	0.005	Normal	2	1	0.0025	∞
Sample density	0.007	Rectangular	$\sqrt{3}$	1	0.0040	∞
Sample length	0.082	Rectangular	$\sqrt{3}$	1	0.0017	∞
B wave form	0.100	Rectangular	$\sqrt{3}$	1	0.0577	∞
Accuracy of the positioning system	0.150	Normal	2	1	0.0750	∞
Combined standard uncertainty		Normal			0.1080	∞
Expanded uncertainty (Declared at the confidence level of 95%)		Normal $k_{95} = 2$			0.2160 (apx. 0.22)	

Table 6.2 Uncertainty budget of localised B$_{peak}$ values of all test samples measured by needle probe.

The basis of evaluation of sources of uncertainty in table 6.2 is detailed below.

- Repeatability of local B_{peak} measurement. An experiment was conducted to find the repeatability of localized B measurement at different level of global applied B, 1.1 T, 1.5 T and 1.7 T. It was set by repeating measurement three times at five selected points of each of the three test samples of HiB steel. The highest repeatability was calculated by means of using the highest difference between the values of the three measurements taken at the same point divided by the smallest value of the three measurements. As shown in table 6.3, the highest repeatability of all measurements is given by $\pm$ 0.1%, this value is used for all evaluations in the entire investigation.

Global B		Meas 1	Meas 2	Meas 3	Repeatibility
1.1 T	Point 1	1.074	1.075	1.075	±0.09%
	Point 2	1.102	1.102	1.103	±0.09%
	Point 3	0.998	0.998	0.998	±0.00%
	Point 4	1.089	1.089	1.089	±0.00%
	Point 5	1.132	1.133	1.132	±0.09%
1.5T	Point 1	1.617	1.616	1.616	±0.06%
	Point 2	1.695	1.695	1.695	±0.00%
	Point 3	1.305	1.304	1.305	±0.08%
	Point 4	1.491	1.491	1.491	±0.00%
	Point 5	1.553	1.553	1.552	±0.07%
1.7T	Point 1	1.578	1.578	1.578	±0.00%
	Point 2	1.679	1.678	1.679	±0.06%
	Point 3	1.338	1.338	1.338	±0.00%
	Point 4	1.802	1.801	1.802	±0.06%
	Point 5	1.730	1.730	1.730	±0.00%

Table 6.3 Repeatability of localised B_{peak} measured using the needle probe.

- Accuracy of NI PCI-6731 DAQ. The accuracy range of voltage output at $\pm10V$ is $\pm2.24mV$ according to the manufacture specifications. This gives accuracy range in percentage is $\pm0.023\%$.

- Frequency setting. $\pm 0.01\%$ variation is given by the base clock accuracy of the DAQ.

- Sample mass measurement. All samples were weight utilizing an Avery Berkel balance with smallest division of 0.01 g. An average value of three measurements was used for each sample, providing a calculated expanded uncertainty of approximately $\pm 0.01\%$ for all samples.

- Needle separation distance. The distance between two needle tips was measured by moving sample stage with division of distance of 0.01 mm under an optical microscope. The measurement was repeated five times and produced a calculated expanded uncertainty of $\pm 0.005\%$.

- Sample density. The density of GO steel given by the manufacture is 7650 Kg/m^3. Assuming the accuracy of the data is at ± 0.5 Kg/m^3, then the relative accuracy in percentage is ± 0.007.

- Sample length. The assumed length of an Epstein sample is 305 mm. The actual length of the test sample was measured utilizing a metal ruler with division of 0.5 mm. Thus, the last digit of the reading can be estimated at half of the division which provides an accuracy of ± 0.25 mm, giving relative accuracy of 0.082%.

- B waveform control. B_{peak} and form factor were set through LabVIEW control at $\pm 0.1\%$ for all experiments conducted in the investigation.

- Accuracy of the positioning system. The manufacture provided specification of repeatability of 'Parker cross roller series' is ± 3.0 µm. The scanning resolution of all measurement is set to be 2 mm. Therefore, the accuracy of the measurement utilising this positioning system is $\pm 0.15\%$.

Sources of uncertainty	Value $\pm\%$	Type of distribution	Divisor	c_i	$u(x_i)\pm\%$	v_i or v_{eff}
Repeatability of local H$_{peak}$ measurement (Type A evaluation)	0.2600	Normal	2	1	0.13000	2
Accuracy of NI PCI-6731 DAQ	0.023	Normal	2	1	0.0115	∞
Frequency setting	0.010	Normal	2	1	0.0050	∞
Accuracy of the positioning system	0.150	Normal	2	1	0.0750	∞
Accuracy of the Hall effect sensor	1.040	Normal	2	1	0.5200	∞
Accuracy of the input voltage	0.100	Normal	2	1	0.0500	∞
Combined standard uncertainty		Normal			0.5437	∞
Expanded uncertainty (Declared at the confidence level of 95%)		Normal $k_{95}=2$			1.0874 (apx. 1.09)	

Table 6.4 Uncertainty budget of localised H$_{peak}$ values of all test samples measured by Hall Effect sensor 50 Hz sinusoidal magnetisation.

The basis of evaluation of sources of uncertainty in table 6.4 is detailed below.

- Repeatability of local H$_{peak}$ measurement. An experiment was conducted to find the repeatability of localized H$_{peak}$ measurement at different level of global applied B, 1.1 T, 1.5 T and 1.7 T. It was set by repeating measurement three times at five selected points of each of the three test samples of HiB steel. The uncertainty of repeatability at the worst point is $\pm$ 0.26%. This value is therefore suitable for all cases evaluation.

- Accuracy of the Hall Effect sensor. When operated at $V_{supply} = 5$ V, the typical linearity span of 'Honeywell' SS495A1 Hall sensor given by manufacture specification is $\pm 1\%$ and typical temperature error null drift is $\pm 0.04\%$. Thus, the estimated accuracy of the Hall Effect sensor is the summation of the two values.

- Accuracy of the power supply. An operating voltage of 5 V was applied to the Hall Effect sensor utilising a Farnell stabilised power supply. The output value was checked against a Mastech MY-67 multi-meter with accuracy of ±0.1 % given by manufacture.

Sources of uncertainty	Value $\pm\%$	Type of distribution	Divisor	c_i	$u(x_i)$ $\pm\%$	v_i or v_{eff}
Repeatability of local P measurement (Type A evaluation)	0.82	Normal	2	1.5	0.62	2
H measurement	1.09	Normal	2	1	0.60	∞
B measurement	0.22	Normal	2	1	0.15	∞
Combined standard uncertainty		Normal			0.88	∞
Expanded uncertainty (Declared at the confidence level of 95%)		Normal $k_{95} = 2$			1.76	

Table 6.5 Uncertainty budget of localised P values of all test samples measured by Hall effect sensor 50 Hz sinusoidal magnetisation.

The uncertainty of repeatability at the worst point of all measurements was $\pm 0.82\%$. This value was used for all cases of evaluation. C_i of localised P measurement of 1.5 was obtained by reviewing the relationship between B and P over the studied B field range (1.0 to 1.7 T) in this investigation. The ratio of dB/dP increases as increasing overall applied flux density as shown in figure 6.12. The highest ratio was approximately equal to 1.5 and was used in this investigation.
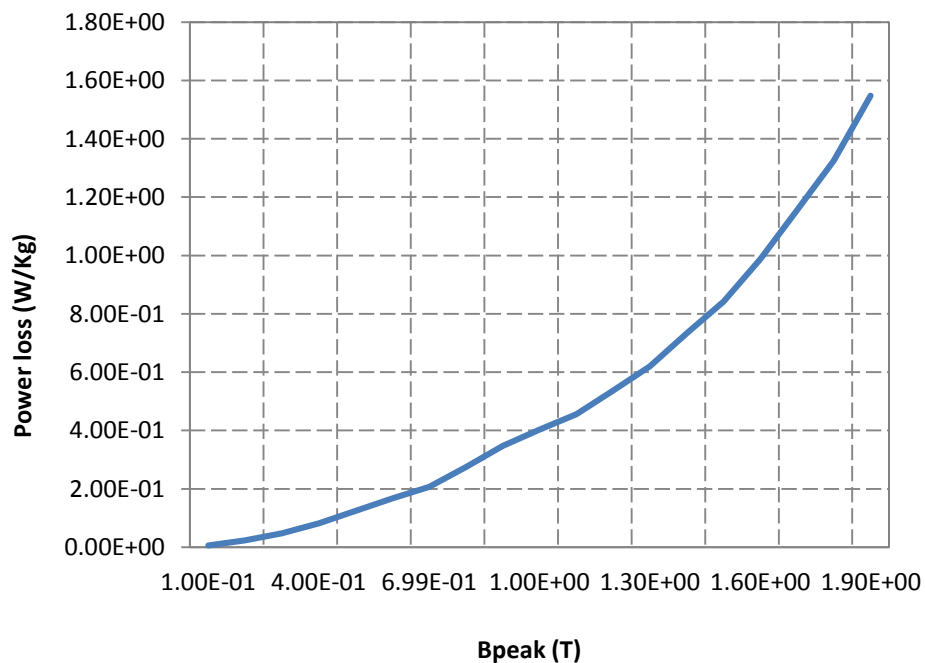

Figure 6.12 Relationship between power loss of HGO steel and overall applied flux density measured using a single strip tester.

Sources of uncertainty	Value $\pm\%$	Type of distribution	Divisor	c_i	$u(x_i)\pm\%$	v_i or v_{eff}
Repeatability of local B$_{peak}$ measurement (Type A evaluation)	0.100	Normal	2	1	0.0500	2
Accuracy of NI PCI-6731 DAQ	0.023	Normal	2	1	0.0115	∞
Frequency setting	0.010	Normal	2	1	0.0050	∞
Mass measurement	0.010	Normal	2	1	0.0050	∞
Cross sectional area measurement	0.010	Normal	2	1	0.0050	∞
Sample density	0.007	Rectangular	$\sqrt{3}$	1	0.0040	∞
Sample length	0.082	Rectangular	$\sqrt{3}$	1	0.0017	∞
B wave form	0.100	Rectangular	$\sqrt{3}$	1	0.0577	∞
Combined standard uncertainty		Normal			0.0782	∞
Expanded uncertainty (Declared at the confidence level of 95%)		Normal $k_{95} = 2$			0.1563 (apx. 0.16)	

Table 6.6 Uncertainty budget of localised B$_{peak}$ values measured using search coil.

References

[6.1]   X. Xu, A. Moses, J. Hall, P. William and K. Jenkins, "A comparison of magnetic domain images using a modified Bitter pattern technique and the Kerr method on grain-oriented electrical steel", IEEE Transactions on Magnetics, vol. 47, pp. 3531 – 3534, (2011).

[6.2]   Available online at www.downloads.techimaging.com/docs/Fastcam_MC1_HW_Manual_Rev100en.pdf, last accessed on 3rd Nov. 2013.

[6.3]   O. Hoshtanar, "Dynamic domain observation in grain-oriented electrical steel using magneto-optical techniques", PHD Thesis, Cardiff University, (2006).

[6.4]   S. Zurek, P. Marketos, P. I. Anderson, and A. J. Moses, "Influence of digital resolution of measuring equipment on the accuracy of power loss measured in Epstein frame," Przegląd Elektrotechniczny (Electrical Reviews), Vol. R. 83, pp. 50-53, (2007).

[6.5]   UKAS M3003, 'The expression of uncertainty and confidence in measurement', 2nd edition, (2007).

Chapter 7

Specimen Selection and Preparation

7.1 Selection of test specimens

Epstein specimens of 305 mm x 30 mm for the study of local magnetic properties were cut from a square sheet of 500 x 500 mm using a mechanical guillotine. All test material was provided by Cogent Power Ltd. in Newport, UK, and it is a type of commercial HiB steel with manufactures specifications are shown in table 7.1. The polarisation at H = 800 A/m (or $B_{H=800}$) shown in table 7.1 is often used by electrical steel manufactures to describe magnetic property of their products. Material with higher value of $B_{H=800}$ usually shows lower measured power loss.

Product code	Thickness (mm)	Maximum specific loss (W/Kg) at 1.7 T, 50 Hz	Typical specific loss (W/Kg) at 1.7 T, 50 Hz	Polarisation (T) at H = 800 A/m (50 Hz)
M111-30P	0.30	1.11	1.08	1.93

Table 7.1 Typical specifications provided by the manufacture. [7.1]

Apart from the commercial specimens listed above, additional Epstein size 0.3 mm thick, poorly oriented electrical steel was prepared in the laboratory to have an extremely poor texture. It was use in this investigation for the study of the effect of grain misorientation on the variation of local magnetic properties.

Table 7.2 shows the specifications of all Epstein specimens studied in this investigation, including seven commercial HiB specimens (coded H1 – H7) and one poorly oriented specimen (P1). Assuming specimens contain round grains, the average grain diameter D in table 7.2 is calculated from equation below

$$D = 2 \times \sqrt{\frac{A}{N\pi}}$$

where A is the surface area of the Epstein specimen (305 mm x 30 mm) and N is number of grains in the specimen assessed using both visual inspection and Orb domain viewer inspection.

The yaw angle, which is the in-plane deviation angle of the grain orientation [001] from the RD of the specimen, was measured by assessing the deviation angles of bar domains observed using the domain viewer. The specimens were decoated and stress relief annealed prior for all experiments carried out in this investigation (annealing procedure is outlined in 7.2). The power loss values shown in table 7.2 were measured thereafter using a single strip tester which is calibrated with respect to a standard Epstein square. Relatively higher power loss values are shown in table 7.2 in comparison with the manufacture specification, which is due to removal of the insulation coatings that provide beneficial effect on the overall power loss of the steel. It can be considered that the thickness of coatings is uniform so removal of the coatings will have no significant effect on the distribution of localised magnetic properties.

Specimen	Average grain diameter D (mm)	Average yaw angle deviated from RD (°)	Power loss$_{1.7T/50Hz}$ (W/Kg)	$B_{H=800}$ (T)
H1	10.0	3	1.23	1.92
H2	10.8	3	1.25	1.90
H3	10.3	3	1.27	1.88
H4	9.8	3	1.25	1.90
H5	10.4	3	1.26	1.90
H6	10.1	3	1.20	1.92
H7	9.9	3	1.25	1.90
P1	12.3	18	2.40	1.55

Table 7.2 Specifications of the Epstein specimens.

7.2　Preparation of test specimens

7.2.1　Preparation of Epstein strips for local loss measurement.

Coating removal – To ensure needle signal quality, the insulation coating of all test specimen was removed in a HCL bath of 38% concentration. During the process of chemical reaction, constant inspection was involved to avoid over-etching of the test specimen. Once the coating layer was removed, the specimen was soaked in an Acetone bath of 99% concentration to wash away the remaining acid. After which specimen was rinsed with Kemet cleaning fluid CO42 and dried up using clean paper towel to prevent it from further oxidation.

Stress relief annealing – Annealing is required to remove stresses that are added in the steel during material handling. The process was carried out after the coating had been removed on both surfaces of specimen. A PC-controlled Elite vacuum tube furnace with a set programme shown in table 7.3 was used for stress relief anneal of all test specimens. To prevent specimen oxidation, a minimum pressure of less than 10^{-5} mbar was maintained using the build-in turbo pump throughout the entire annealing process.

Segment	Program	Temperature ($^{\circ}$C)	Heating Rate ($^{\circ}$C / hour)
1	Heating up	Room temperature – 810	250
2	Duration	810 $^{\circ}$C for 1 hour	0
3	Cooling down	810 $^{\circ}$C – room temperature	-50

Table 7.3 Annealing programme for stress relief annealing of electrical steel specimens.

7.2.2　Preparation of specimens for Kerr microscope observation.

Specimens for Kerr microscope observation were metallurgical prepared to a mirror surface finishing. The procedure consists of grinding and polishing which was carried out using the Struers magnetic disc (MD) machine. The specifications of the corresponding grinding and polishing discs used in the metallurgical preparation are

listed in table 7.4, in which discs 1 & 2 are grinding discs and discs 3 & 4 are polishing discs.

No.	Disc code	Disc diameter (mm)	Roughness (μm)	Abrasive fluid
1	MD-Piano 600	300	15.3	Water
2	MD-Largo	300	9	Water + Largo diamond suspension
3	MD-Dac	300	9-3	DP-Lubricant + Dac diamond suspension
4	MD-Nap	300	≤1	DP-lubricant + Nap diamond suspension

Table 7.4 Specifications of the grinding and polishing discs for preparation of the specimens for Kerr microscope examination.

Sharp corners and edges of the specimens were removed using a silicon carbide paper prior the metallurgical preparation as to protect the preparation discs from scratches. For an easy grip, specimens to be prepared were pasted onto pre-made sample holders using high strength, double sided tape.

Specimens after metallurgical preparation were heated up in a laboratory furnace at 130 $^{\circ}$C to soften the tape so that the specimens could be separated from their holders. Specimens thereafter were stress relief annealed using the method outlined in 7.1 for the removal of residual stresses which were added by the mechanical grinding process.

Reference

[7.1]   http://www.cogent-power.com/unisil-h/unisil-h-guaranteed-magnetic-properties/, last accessed on 8th Feb 2014.

Chapter 8

Results and Discussion

8.1 Introduction

Domain observation is frequently involved throughout the entire investigation in the study of magnetic characteristic of test specimens presented in this chapter. Static domain patterns were observed for assessing the grain orientation of test specimens and the domain wall spacing of the domain scribed specimen. Dynamic domain observations were carried out in the study of domain wall movement; and to help improve the understanding of localised non-uniform magnetisation in grain oriented electrical steels.

The domain viewer and magneto-optical Kerr microscope were used for observing domain structures. A comparative study was carried out as described in 8.2 to explain differences in the domain pattern on the same specimen under the same conditions observed using these techniques.

The needle probe for measurement of localised flux density is outlined in chapter 6. A test to assess the accuracy of the needle probe on measurement of localised flux density is described in 8.4.

Components of localised flux density in rolling and transverse directions of a HiB specimen, measured using an orthogonal needle probe, are presented in 8.5.

The transverse flux density is compared with rolling flux density so that the effect of transverse flux density on power loss of HiB steel could be quantified.

Localised flux density at different levels of magnetic induction was measured using the needle probe on a HiB specimen and is presented in 8.6 and the influence of induction level on the degree of variation of flux density is discussed.

Localised flux density, magnetic field and power loss was measured in the commercial HiB specimen and the laboratory produced poorly oriented specimen using the local loss measurement system outlined in chapter 6. The results are displayed in 8.8 and the effect of grain misorientation on the distribution of localised magnetic properties is discussed.

Localised magnetic flux density of specimen H7 before and after scribing were measured using the local loss measurement system and is presented in 8.9 and the influence of domain refinement on the distribution of localised magnetic flux density could be analysed.

8.2 Differences in observed magnetic domain structures found using domain viewer and magneto-optical Kerr techniques

Differences between magnetic domain patterns on the surface of specimen H1 were obtained using the domain viewer and the magneto-optical Kerr microscope. Both techniques are widely used for observation of magnetic domain pattern on electrical steels but such differences have not been reported previously.

The sample whose surface was observed was a 25 mm square HiB steel cut from H1. The sample was decoated, metallurgical prepared as described in chapter 7 and stress relief annealed prior the domain observation. The grain boundary was not found through optical observation after the sample was chemically etched. An EBSD analysis was carried out at Tata Steel Swinden Technology Centre, UK to study the crystallographic texture of the test sample and to prove the existence of the grain boundary.

Surface domain structure of the prepared sample was observed using the domain viewer and Kerr microscope respectively. Due to the observation limitation of the Kerr microscope, the Kerr observation was carried out by means of scanning sample surface under the microscope.

Figure 8.1 shows the typical anti-parallel bar domain patterns obtained using the domain viewer and the Kerr microscope on the demagnetised sample. The Bitter domain pattern shows a discontinuity in the domain contrast typical of the effect of grain boundary oriented transverse to the RD of the specimen. The Kerr image shows continuous domain magnetisation over the 8 mm x 6 mm area where the possible effect of a grain boundary was found in the Bitter image. No evidence of a grain boundary in the surrounding surface was found using the Kerr microscope. The same number of domains (17 black domains and 17 white domains) was observed using both techniques.
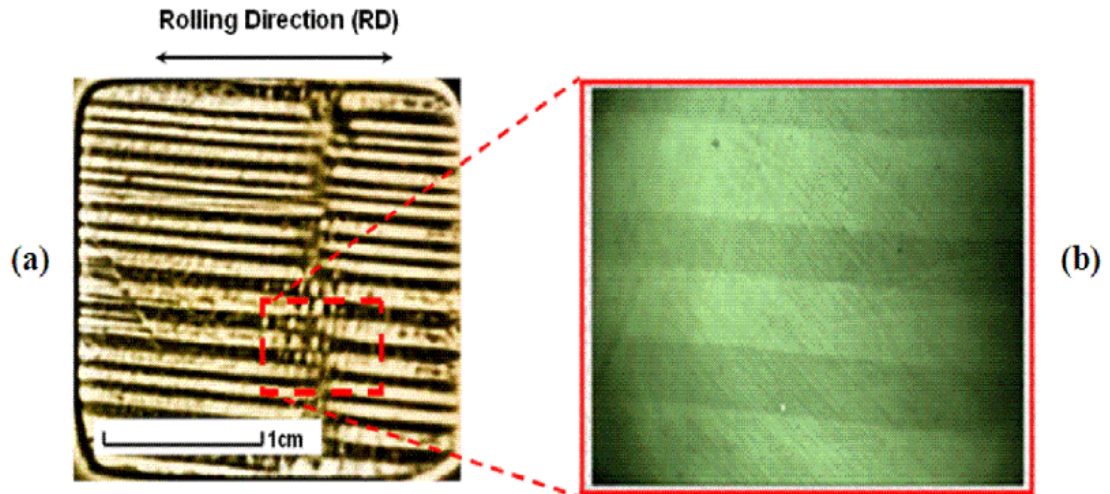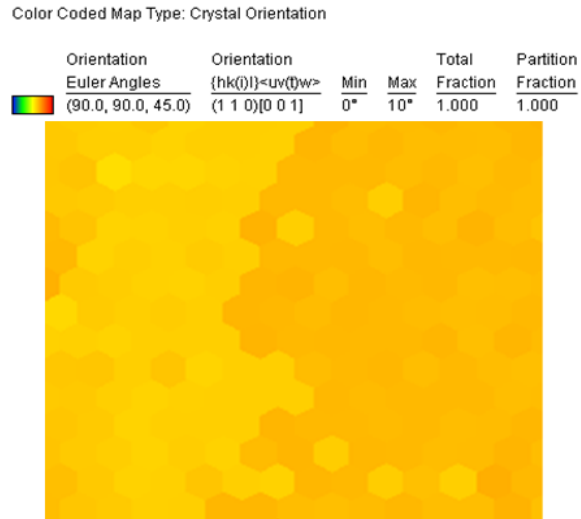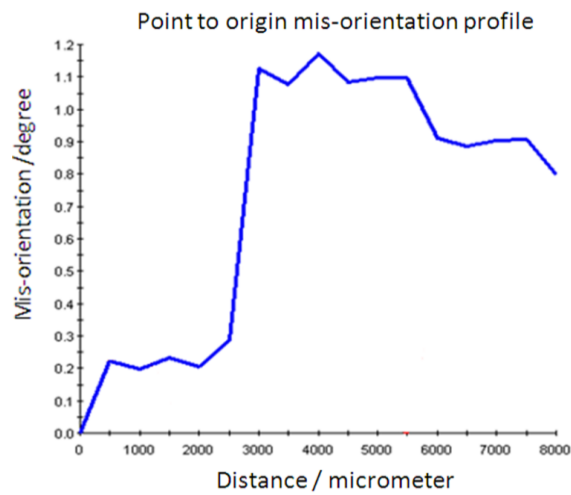
Figure 8.1 (a) Bitter domain image of the whole surface of the 25 x 25 mm specimen observed using the domain viewer, (b) the corresponding Kerr image in the area located inside the dash box [8.1].

In order to confirm that the vertical magnetic field applied in the domain viewer was not the cause of the different images, a vertical DC field of the same strength (approximately 2.2 KAm^{-1}) as used in the domain viewer was applied to the test specimen using a current conducting coil during the Kerr microscope observation. No change of domain contrast was observed.

Figure 8.2 shows the crystallographic texture of the sample obtained from EBSD analysis on the same area as presented in the 8 mm x 6 mm area covered by Kerr image shown in figure 8.1b. The colour-coded map reveals a grain boundary indicated by the lighter and darker yellow boundary, which consistent with that seen in the dash box in figure 8.1a. The misorientation profile shows that the relative misorientation angle between two crystals were less than 1°.

	Orientation Euler Angles	Orientation {hk(i)l}<uv(t)w>	Min	Max	Total Fraction	Partition Fraction
	(90.0, 90.0, 45.0)	(1 1 0)[0 0 1]	0°	10°	1.000	1.000

(a)

Point to origin mis-orientation profile

(b)

Figure 8.2 (a) EBSD colour-coded map shows crystal orientation of the area included in the Kerr image of figure 8.1b, (b) misorientation profile scanned along the transverse direction in (a) [8.1].

In this case, two observation techniques have clearly presented inconsistent information regarding grain boundary and domain magnetisation. However, the number of domains and domain alignment were observed the same using both techniques.

A simple model showing crystal orientation and domain magnetisation of the adjacent grains is illustrated in figure 8.3. As shown in figure 8.3a, the easy magnetising axes [001] indicated by the cubes are slightly deviated with respect to

the surface plane and with respect to each other, as a result, leading to a leakage field on the surface of the specimen shown in figure 8.3b. When an external DC field is applied perpendicular to the surface plane, magnetic dipoles indicated by arrows in figure 8.3b are rotating toward the direction of the field. Therefore, leading to dipoles in one type of domains to coherently rotate towards the surface plane and dipoles in the other type domain to coherently away from the surface plane, since the contrast from the domain viewer is based on the strength of the surface leakage field. As a result, a reversal in domain contrast is developed in the domain viewer. No reversal in Kerr image contrast was observed, since the Kerr effect senses the magnetisation parallel to the surface of the specimen and the overall magnetisation continuous across the grain boundary with and without the presence of the vertical DC field.
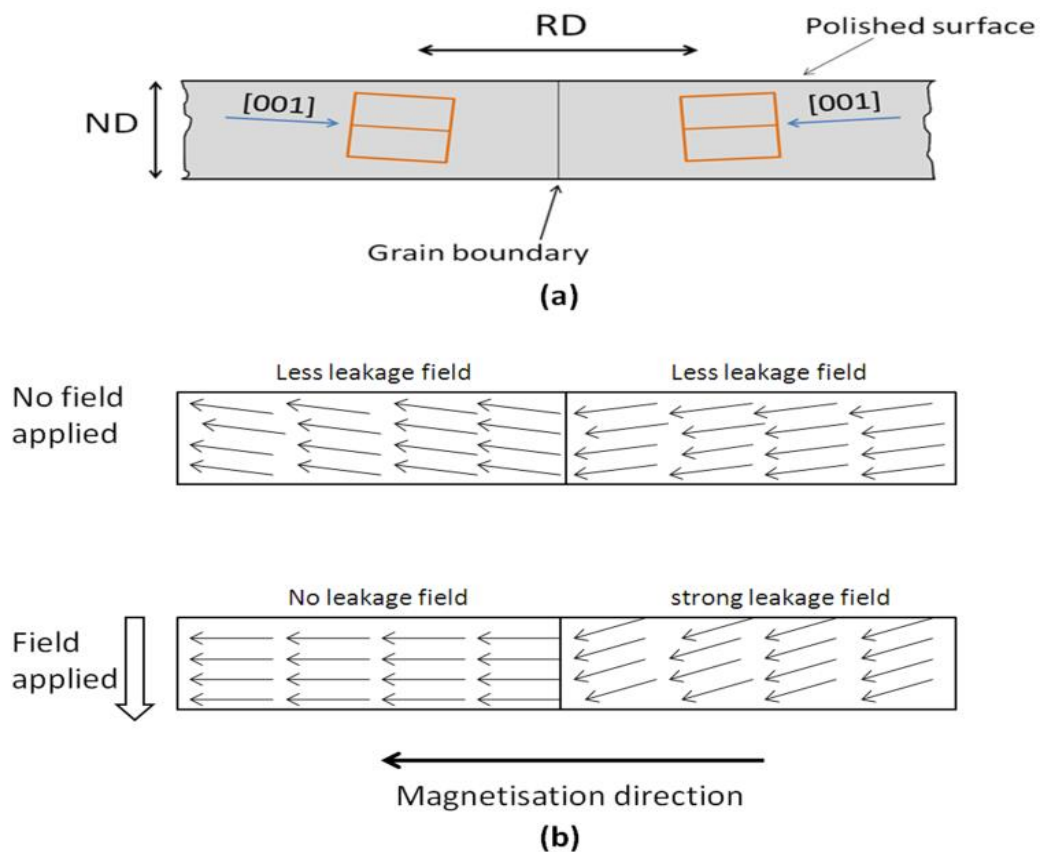

Figure 8.3 Cross sectional view of the test specimen with crystallographic cubes indicating the crystal orientation and arrows indicating the orientation of magnetic dipoles.

8.3 Domain wall movement at grain boundary in sample of grain oriented electrical steels.

An observation of domain wall movement at the small angle grain boundary was carried out using the real time dynamic Kerr microscope system to study the behaviour of dynamic domain on the surface of the sample whose static domain pattern and crystallographic texture was studied in 8.2.

Domains in mismatched grains are often difficult to be clearly presented simultaneously under the Kerr microscope, because the quality of Kerr image depends on how well the plane of incident/reflection light is aligned with the direction of domain magnetisation. Thus, the sample containing small angle grain boundary was selected in this study.

Dynamic domain study was carried out using the dynamic Kerr microscope outlined in chapter 6 at 50 Hz triangular flux density magnetisation. The use of triangular magnetisation was to apply an overall constant dB/dt in the sample for the study of uniformity of localised domain wall motion. The peak flux density at surface domain saturation, measured using single turn search coil wound across the entire cross section of the sample, was 1.20 T. It should be mentioned that eddy current led to domain wall bowing will cause domain wall move faster at the surface than in the middle, thus surface domain saturation occurs at lower flux density compared to the overall saturation flux density ($\sim$2.1 T) of the specimen.

Domain wall motion over the 6 mm x 6 mm area at the grain boundary was captured using the high speed camera at a recording speed of 2000 frames per second and resolution of 512 x 512 pixels (equivalent to 40 frames per magnetising cycle). Prior presenting the dynamic images, it should be mentioned here that dynamic domain pattern can be significantly different from static domain pattern due to domain reconfiguration at power frequency.

The video clip was processed through the LabVIEW vision assistant 7.1 video analysis software for contrast enhancement. This software allows the video to be saved into groups of individual images which were then edited with analysis tools

105

provided in the software. In this experiment, background subtraction and contrast improvement functions were used for improving the image contrast.

Domain pattern captured over 6 mm x 6 mm area at one instant time at 50 Hz magnetisation using the high speed camera is shown in figure 8.4. The black and white strips represent the anti-parallel bar domains whose magnetisation direction is indicated by the red arrows. At this instant time, surface domain saturation occurred in the left grain thus uniform contrast is seen. Grain boundary is identified by the disjointed bar domains and is indicated by the red line. The enlarged image shows that the grain boundary is not a straight line but is in zigzag shape.
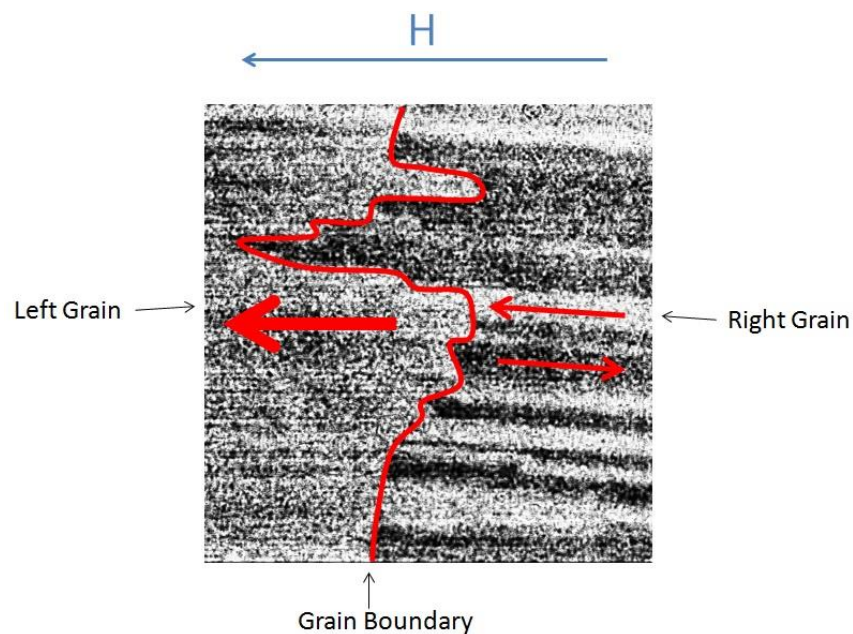
Figure 8.4 Image captured at 50 Hz magnetisation over 6 mm x 6 mm area where grain boundary is found using domain viewer.

Figure 8.5 shows a sequence of domain images captured at time interval of 0.001 second in one complete magnetising cycle at 50 Hz triangular magnetisation. Their corresponding moment of image capture is shown on the triangular waveform below. The direction of domain magnetisation is indicated by the red arrows.
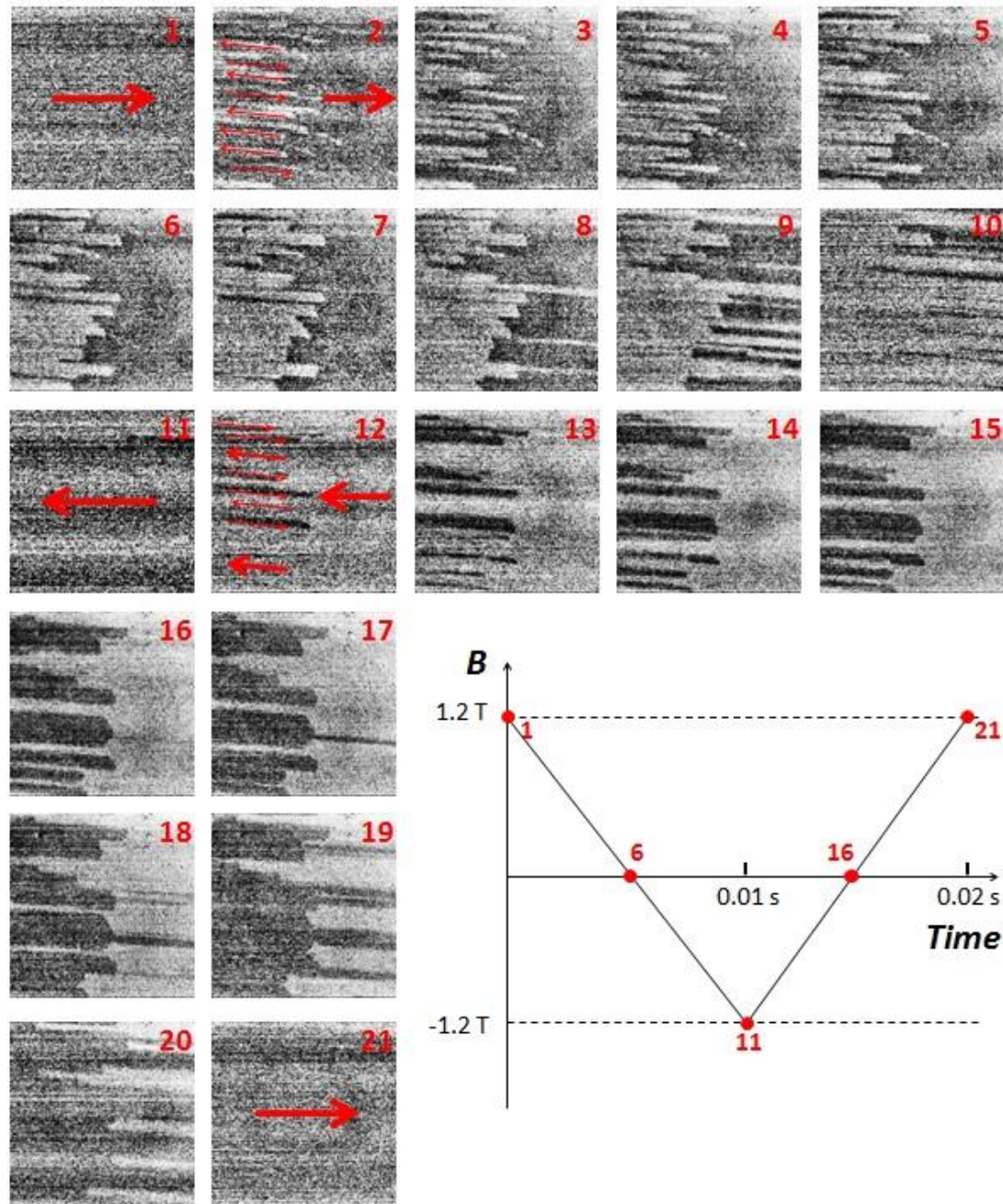

Figure 8.5 Kerr images showing the process of domain wall movement at 50 Hz triangular magnetisation and 1.20 T peak flux density, and area of view is 6 mm x 6 mm at the location where the small angle grain boundary is found in the 25 mm square sample studied in 8.2.

The dynamic domain pattern in figure 8.5 is far more complex than the static domain pattern presented in figure 8.1b. It is seen that the number of domain walls increased substantially under the AC magnetisation. The relationship between magnetisation frequency and domain wall spacing of sinusoidal magnetisation is given by equation 3.1, by substituting frequency 50 Hz into the equation; the estimated number of domain walls is calculated to be seven times more than that of the static domain pattern. In this investigation, the maximum number of domain walls observed over the viewing area is counted to be 25 bar domains as shown in image 3 of figure 8.4, which is just over four times more than that of the static domain walls shown in figure 8.1b. This is because dB/dt of the triangular magnetisation is believed to be lower than the peak dB/dt of the sinusoidal magnetisation, thus, less number of 180° domain walls need to be produced for reducing the average wall speed.

It is found that domain walls are not moving homogeneously at the grain boundary; the reasons for the inhomogeneous wall movement are outlined in chapter 3. The 90° surface closure domains are not emerged in the process of AC magnetisation as the inclination angles in both grains are considerable small. Domain walls exhibit higher mobility in the left grain than that in the right grain as the surface domain saturation occurred earlier in the left grain than that in the right grain. Such grain to grain inconsistent wall movement is not expected to occur at small angle grain boundary of closely oriented grains, and could not be fully explained in this investigation, which will be the subject of future investigation.

Flux closure domains are not observed at the grain boundary of the discontinued domain magnetisation, hence free magnetic poles are exposed leading to creation of a demagnetising field. Further discussion on the influence of the demagnetising field is carried out in 8.8. The study confirms the inhomogeneous domain walls movement and the existence of the localised demagnetising field when the steel is subjected to AC magnetisation.

8.4   Evaluation of needle probe analysis of flux density in HiB electrical steel.

Previous studies outlined in chapter 5 showed that the accuracy of the needle probe technique can be affected by the inhomogeneous nature of the test material. For grain oriented electrical steels, flux density measurement obtained using needle probe and search coil can be differ by more than 10 % [8.2]. Therefore, experiments were set up to test the accuracy of the bespoke needle probe for measurement of localised flux density in commercial HiB specimens.

8.4.1   Comparison of flux density measurement using the needle probe on opposite surfaces of a HiB specimen.

In needle probe measurement, it is assumed that the flux density is symmetrically distributed with respect to the centre line of the cross sectional area of the test specimen so that needle measurement need only be conducted on one side of specimen. However, the flux density may not be consistent through the thickness of grain oriented steel due to the material is considered to have higher level of inhomogeneity compared with non-oriented electrical steel. Therefore, needle probe measurements obtained from opposite surfaces of a HiB specimen were compared.

Specimen H2 was selected, decoated and annealed prior to measurement. The specimen was magnetised using the local loss measurement system outlined in chapter 6 at sinusoidal flux density at 50 Hz and peak flux density of 1.50 T. The localised peak flux densities in a 64 mm rolling direction (RD) x 20 mm transverse direction (TD) area in the centre of the Epstein strip shown in figure 8.6 were raster scanned using the needle probe at 2 mm sampling intervals. This corresponds to a total sampling point of 363 in the scanning area. After the measurements were completed, the specimen was turned upside down and the experiment was repeated over an identical area of the other surface of the specimen.
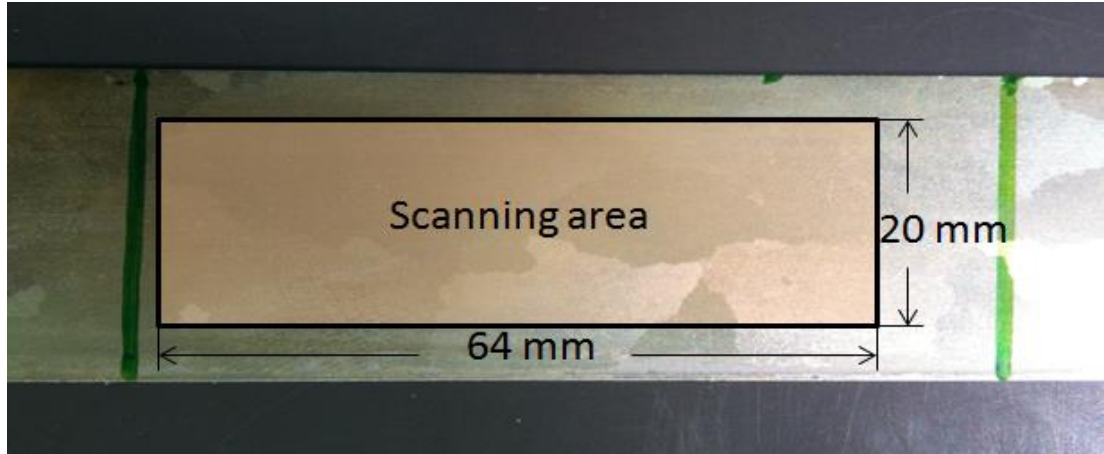
Figure 8.6 Photograph of the scanning area of the H2 strip.

Figure 8.7 shows distribution of localised peak RD component of flux density measured on opposite surfaces of H2 at sinusoidal magnetisation of 50 Hz and overall applied peak flux density of 1.50 T. It can be seen that distribution patterns obtained on both surfaces of the specimen are similar. At over peak flux density of 1.50 T, the average of flux density measurements derived from 363 localised measurements is 1.52 T and 1.51 T on two surfaces respectively shown in table 8.1, which corresponding to a difference of 0.7 % and 1.3 %.

Figure 8.8 shows percentage difference between needle measurements obtained on opposite surfaces of the test specimen, derived from,

$$\% \text{ difference } = \frac{B_{top} - B_{bottom}}{B_{top}} \times 100$$

B_{top} is localised peak flux density value from needle probe measurement obtained on top surface of the specimen and B_{bottom} is the corresponding localised peak flux density value from needle probe measurement obtained on bottom surface of the specimen. The percentage difference between needle probe measurements obtained on opposite surfaces varies across the scanning area from -13 % to 10 %. Most regions show small differences, the average difference derived from 363 sampling point is 1.9 % shown in table 8.1. Regions showing higher differences are randomly distributed, there is no correlation found between distribution of differences and grain boundary pattern. The result presented here indicates that flux density induced in two sides of the commercial HiB specimen may vary slightly.

Thus, to improve the accuracy of NP method on measurement of flux density, it is recommended to use the average flux density measured in opposite sides of the grain oriented steel.
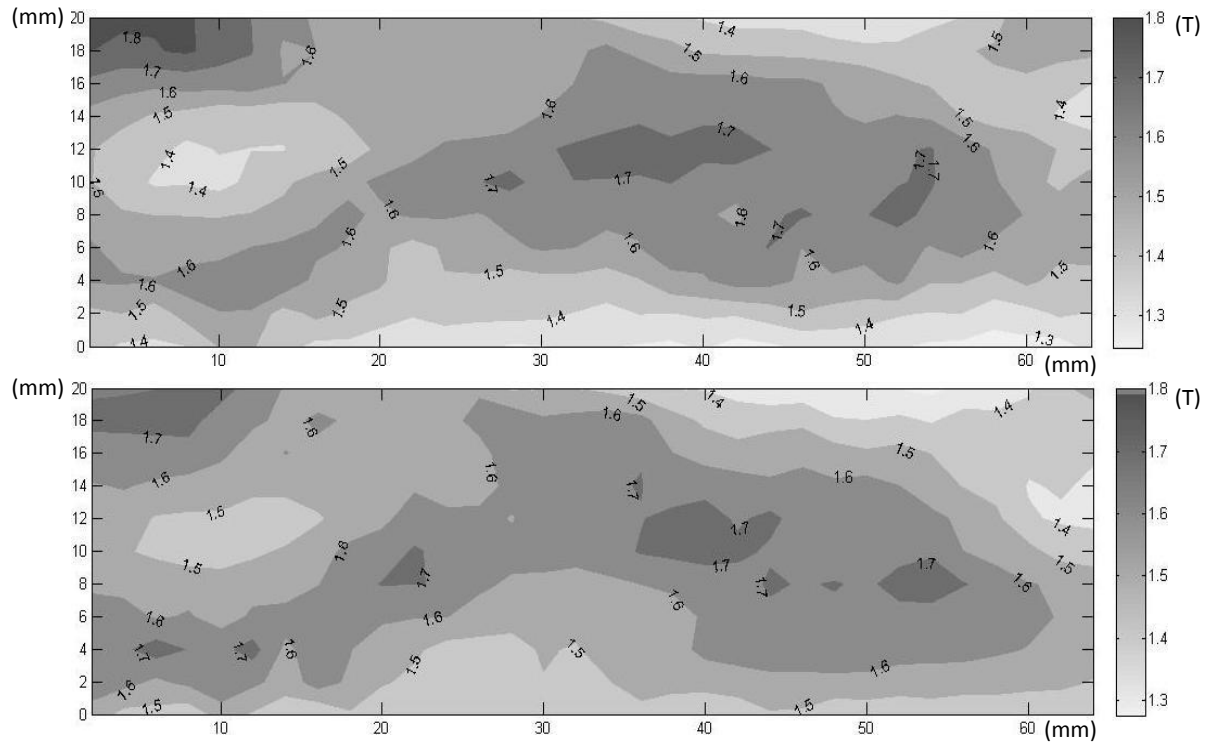

Figure 8.7 Distribution of localised peak RD component of flux density obtained using the needle probe on opposite surfaces of a commercial specimen.
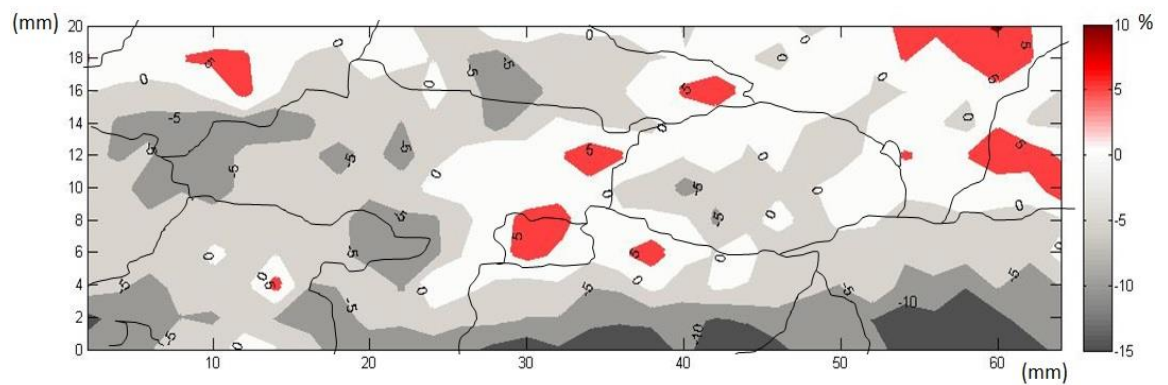

Figure 8.8 Percentage differences between localised peak flux density values obtained on opposite surfaces of a commercial HiB specimen, and grain boundary outlines are superimposed on the contour map.

	Average of localised peak flux density	Average of difference between top and bottom measurements
Top surface	1.52 T	1.9 %
Bottom surface	1.51 T	

Table 8.1 Average localised flux density and percentage difference between needle measurements obtained on top and bottom surfaces of the HiB specimen.

8.4.2 Comparison of localised flux density measurement using the needle probe and search coil methods.

In this part of the experiment, a direct comparison of flux density measurement using the needle probe and single turn search coils was carried out on localised regions of a HiB specimen.

Specimen H3 was decoated and annealed prior to the measurement. Six areas in the central section of the Epstein strip shown in figure 8.9 were selected. The areas are evenly distributed across the diagonal of the central section; each measurement position is separated by 10 mm (in the RD) and 3 mm (in the TD) from its nearby position(s). The black dots indicate the point where needles and search coil holes were located.
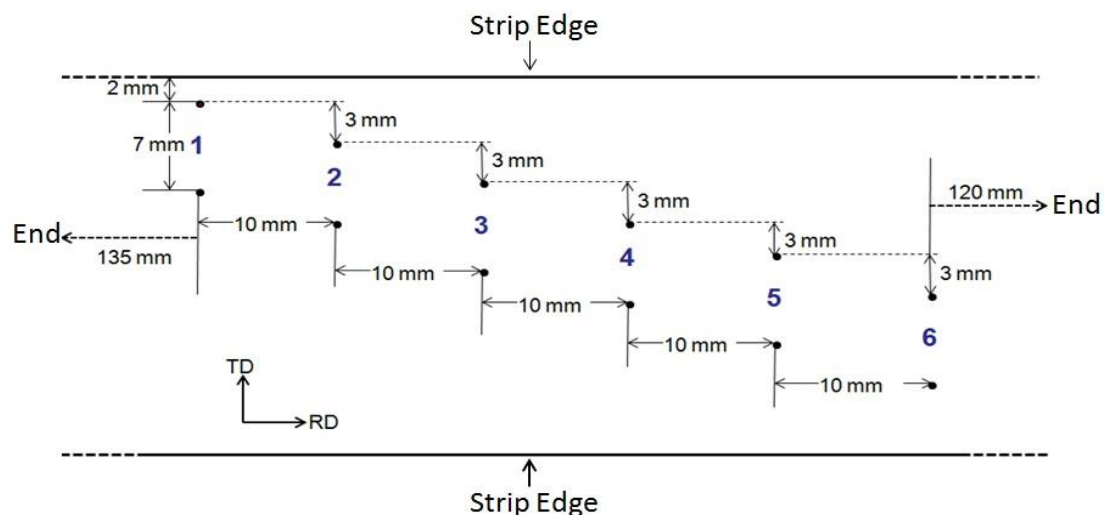

Figure 8.9 Positions of the localised needle probe and search coil measurements on the H3 strip.

The specimen was magnetised using the local loss measurement system at sinusoidal flux density at 50 Hz and peak flux density of 1.50 T. Localised flux density measurements at the six positions marked in figure 8.9 were made using the NP on

one surface of the specimen. The specimen was then turned over and the measurements were repeated over the corresponding areas on the other surface. Next, 0.5 mm diameter holes were drilled at each needle contact point. Single turn search coils of 0.2 mm diameter enamelled copper wire were wound through each pair of holes so that the localised flux density could be measured at each of the needle probe measurement positions. It should be noted that the effective distance enclosed by the SC is the same as that of the NP as described in chapter 5. Finally, the search coil wires were removed and the specimen was stress relief annealed to remove the residual stresses caused by drilling, new search coil wires were wound thereafter at each position and the same measurements were repeated.

Localised flux density measurements obtained using needle probe and search coil method respectively at the six local areas on the HiB specimen at 50 Hz and peak flux density of 1.50 T are compared in table 8.2. The percentage differences in measurements before and after anneal was calculated from,

$$\% \text{ difference in SC measurements} = \frac{B_{\text{after anneal}} - B_{\text{before anneal}}}{B_{\text{after anneal}}} \times 100$$

The percentage differences in NP and SC measurements was calculated as,

$$\% \text{ difference in NP and SC} = \frac{B_{\text{NP}} - B_{\text{SC after anneal}}}{B_{\text{NP}}} \times 100$$

Position	Measurements obtained using NP	Measurements obtained using SC			% difference between NP and SC after anneal
		Before anneal	After anneal	% difference	
1	1.48 T	1.38 T	1.52 T	9.2	-2.7
2	1.53 T	1.36 T	1.54 T	11.7	-0.7
3	1.59 T	1.65 T	1.61 T	-2.5	-1.3
4	1.37 T	1.53 T	1.38 T	-10.9	-0.7
5	1.30 T	1.42 T	1.29 T	-10.1	0.8
6	1.55 T	1.71 T	1.53 T	-11.8	1.3

Table 8.2 Comparison of localised flux density measurement obtained using the NP and SC methods on the HiB specimen at 50 Hz and peak flux density of 1.50 T.

The result shows that the stress caused by drilling holes has a substantial influence on localised flux density measurement using the SC when 0.5 diameter holes were drilled at 7 mm span. Annealing removes elastic residual stress introduced by drilling process, but cannot fully restore domain structure as the new flux closure domains are formed and the remaining plastic stress may continue to cause distortion on flux path. Therefore, the technique is still considered as a destructive method for measurement of localised flux density. In this study, holes of 0.5 mm diameter were drilled for minimising the effect of drilling on accuracy of SC measurement since the smallest drill available was 0.5 mm.

The percentage difference between flux density measured using NP and those measured after annealing using SC varies between -2.7 % to 1.3 %. It is note that the measurement uncertainties for both methods are estimated small, $\pm$0.22 % for NP and $\pm$0.16 % for SC. Thus, the effect of uncertainty on the comparison is neglected.

The results here show that through averaging flux densities derived from opposite surfaces in NP measurement and stress relief anneal the specimen after drilling holes in SC measurement, the two methods are able to provide consistent measurements on grain oriented electrical steel.

8.5 2-D measurement of local magnetic flux density using the orthogonal needle probe.

The components of flux density in both RD and TD in commercial HiB steel were measured using the orthogonal needle probe and were compared with each other to study the influence of the TD component of flux density on distribution of localised flux density.

Specimen H4 was decoated and annealed prior to the experiment. The specimen was magnetised using the local loss measurement system at sinusoidal flux density magnetisation of 50 Hz and peak flux density of 1.50 T. An area of 64 mm (RD) x 20 mm (TD) in the centre of the strip shown in figure 8.10 was raster scanned using the ONP at 2 mm sampling intervals. The measurement was repeated on the identical area of both surfaces and average was plotted as contour distribution maps.

Figure 8.11 shows the distribution of the components of localised flux density measured using the ONP in the rolling and transverse directions and the resultant. The resultant flux density $B_{resultant}$ was calculated from the components using the equation below,

$$B_{resultant} = \sqrt{B_{rolling}^2 + B_{transverse}^2}$$

where $B_{rolling}$ is the RD component of flux density and $B_{transverse}$ is the TD component of flux density.

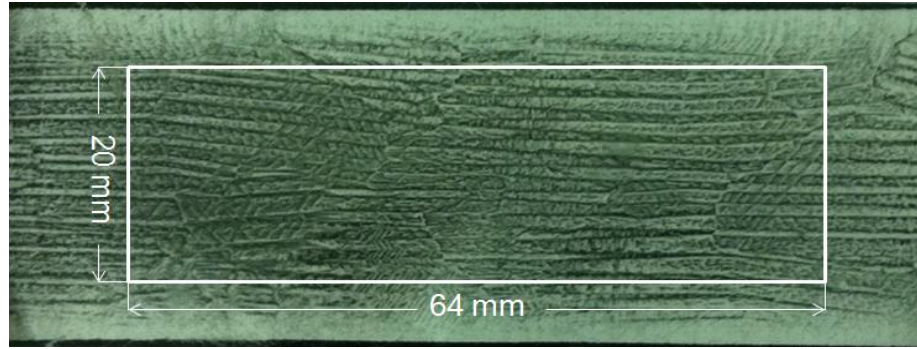**Figure 8.10** Bitter domain pattern obtained using the domain viewer over the centre section of the H4 strip.
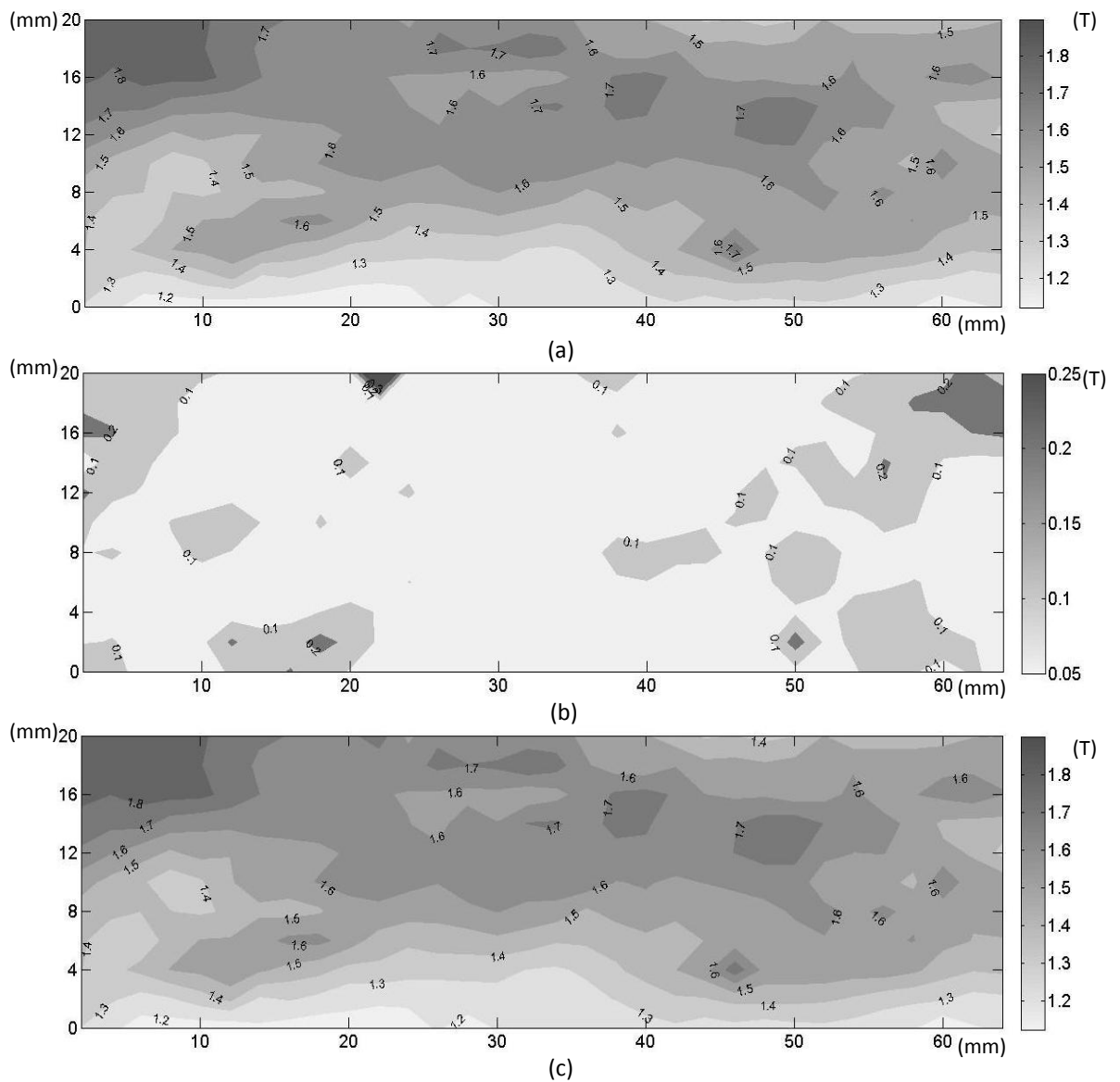

(a)

(b)

(c)

Figure 8.11 Distribution of localised flux density at sinusoidal magnetisation of 50 Hz and overall peak flux density of 1.50 T over the same region of specimen H4 shown in the box in figure 8.10. (a) RD component of flux density, (b) TD component of flux density and (c) resultant flux density.

Table 8.3 shows average localised flux density measurements derived from 363 localised measurements for components of flux density measured in RD and TD and the resultant flux density.

Average RD component of flux density	Average of TD component of flux density	Average resultant flux density
1.51 T	0.13 T	1.52 T

Table 8.3 Average localised flux density.

At overall peak flux density of 1.50 T, RD component of localised flux density is found to vary in a range from 1.18 to 1.82 T, TD component of localised flux density is found to vary in a range from 0.05 to 0.25 T. The average of components of localised flux density measured in RD and TD is 1.51 T and 0.13 T respectively shown in table 8.3, the TD component of localised flux density is found equivalent to 8.6 % of the RD component of localised flux density.

Figure 8.11a and 8.11c show distributions of RD component of localised flux density and the resultant localised flux density respectively. Very similar trends in flux distributions are seen between these two distribution maps. The average localised resultant flux density increased by less than 0.01 T or 0.6 % compare to that of measured in RD alone. The result shows that the TD component of flux density is relatively small and distributed more uniformly compared to that of the RD component. For the study of distribution of localised flux density in HiB steel, it is not necessary to take into account of the TD component of flux density.

Further study on TD component of flux density is presented in 8.7, where the TD component of flux density in a poorly oriented specimen is compared with a HiB specimen to study the correlation between grain misorientation on TD component of flux density.

8.6 Influence of induction level on distribution of flux density.

In this part of the investigation, localised flux density is measured using the needle probe on a HiB specimen at low induction (1.00 T) and power inductions (1.50 and 1.70 T) to study the influence of induction level on the distribution of localised flux density.

Specimen H5 was decoated and annealed prior to the experiment. The specimen was magnetised using the local loss measurement system at sinusoidal flux density magnetisation of 50 Hz and peak flux density of 1.00 T. The localised peak RD component of flux densities in a 50 mm (RD) x 20 mm (TD) area in the centre of the strip shown in the red box in figure 8.12 were raster scanned using the needle probe at 2 mm sampling intervals. This corresponds to a total sampling point of 286 in the scanning area. After the measurements were completed, the specimen was turned over and the experiment was repeated over an identical area of the other surface of the specimen. The experiment was repeated at 1.50 T and 1.70 T.
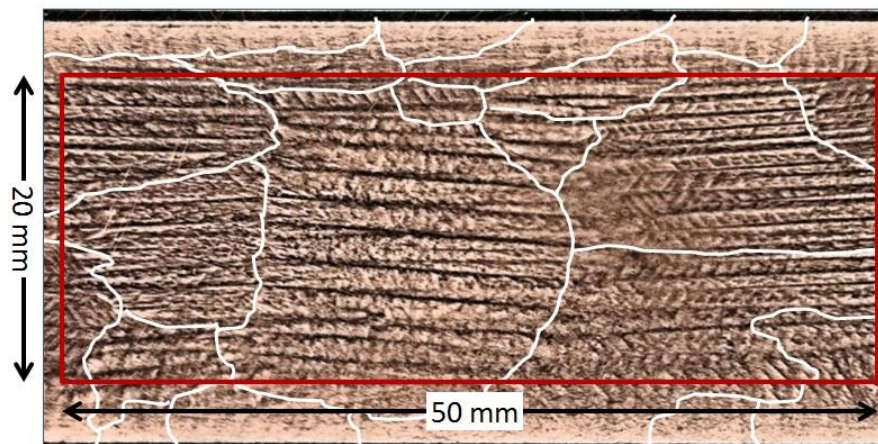

Figure 8.12 Bitter domain pattern of the centre of the H5 specimen obtained using domain viewer, and grain boundary outlines are superimposed over the domain image.

Figure 8.13 shows the distributions of localised rolling flux density obtained using the needle probe at different levels of inductions. At overall applied peak flux density of 1.00, 1.50 and 1.70 T, the averages of localised flux density measurements derived from 286 sampling points are 1.04, 1.54 and 1.74 T respectively shown in table 8.4, which correspond to a difference of 4.0 %, 2.7 % and 2.4 %.
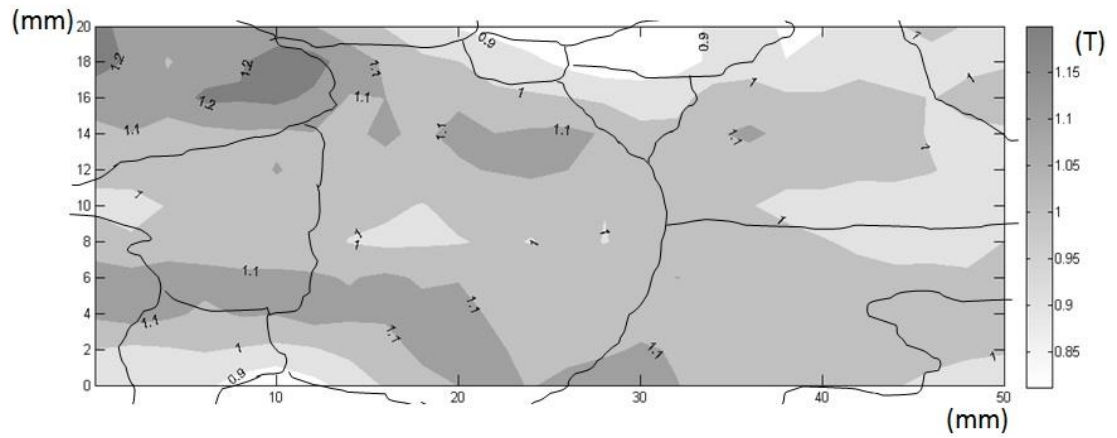
(a) 1.00 T
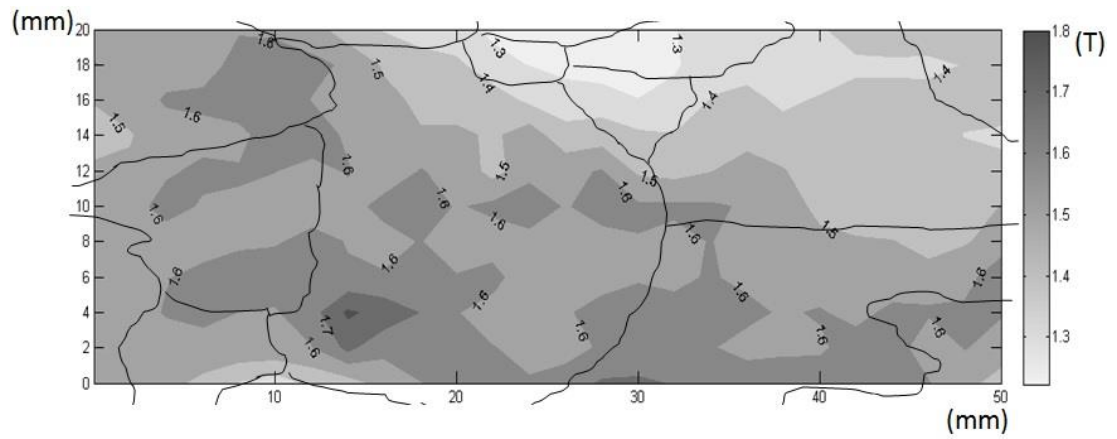
(b) 1.50 T
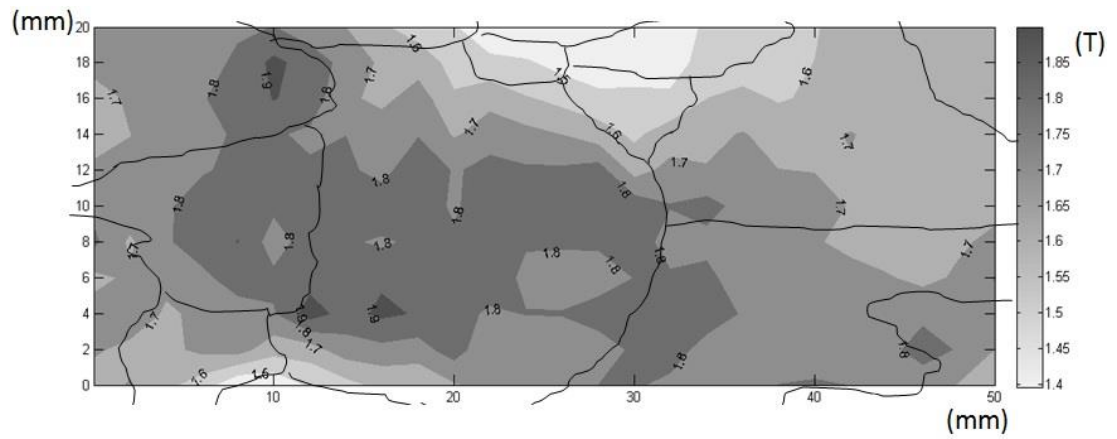
(c) 1.70 T

Figure 8.13 Distribution of peak RD component of flux density at sinusoidal magnetisation of 50 Hz and overall peak flux density of 1.00 T, 1.50 T and 1.70 T over the same region of specimen H5 shown in the box in figure 8.12, and grain boundary outlines are superimposed on each contour map.

	$B_{overall}$=1.00 T	$B_{overall}$=1.50 T	$B_{overall}$=1.70 T
Average of local flux density	1.04 T	1.54 T	1.74 T
Standard deviation of local flux density	7.9 %	10.6 %	11.8 %

Table 8.4 Average and standard deviation of localised flux density measurements.

It can be seen in figure 8.13 that increase in induction level leads to change in characteristic of distribution of flux density. At lower flux density (1.00 T), as outlined in chapter 3, flux tends to distribute along the RD of the specimen and forms the elongated patterns. This is because less number of domain walls is involved in the magnetisation process compare with at higher induction level, domain walls are likely to move simultaneously on either side of grain boundary as a result of minimisation of magnetostatic energy at grain boundaries. At higher induction level (1.5 and 1.7 T), the magnetostatic energy profile is changed due to domain wall refinement and banding of the 180° main domain walls, domain wall mobility is dominantly influenced by magnetocrystalline anisotropy energy. Therefore, flux tends to distribute more according to grain boundary outlines to avoid relatively poorly oriented grains. As a result, lead to higher degree of variation of localised flux density as indicated by the standard deviations shown in table 8.4.

Localised flux density at each sampling point measured at lower induction level was subtracted from that of at higher induction level in Excel spreadsheet. It is found that all localised flux density increases with increasing the induction level, the rate of increasing varies from area to area. This means that the overall increase in induction level is mainly accomplished by substantial increase in flux density in partial areas.

Figure 8.14 shows percentage surface area of steel of flux density range. The figure shows that localised flux densities exhibit normal distribution, which means that localised flux densities measured in most areas of the steel are close to the applied induction. Increase induction level is found to broaden the range of the distribution as a result of change in characteristic of distribution of flux density and substantial increase in localised flux density.
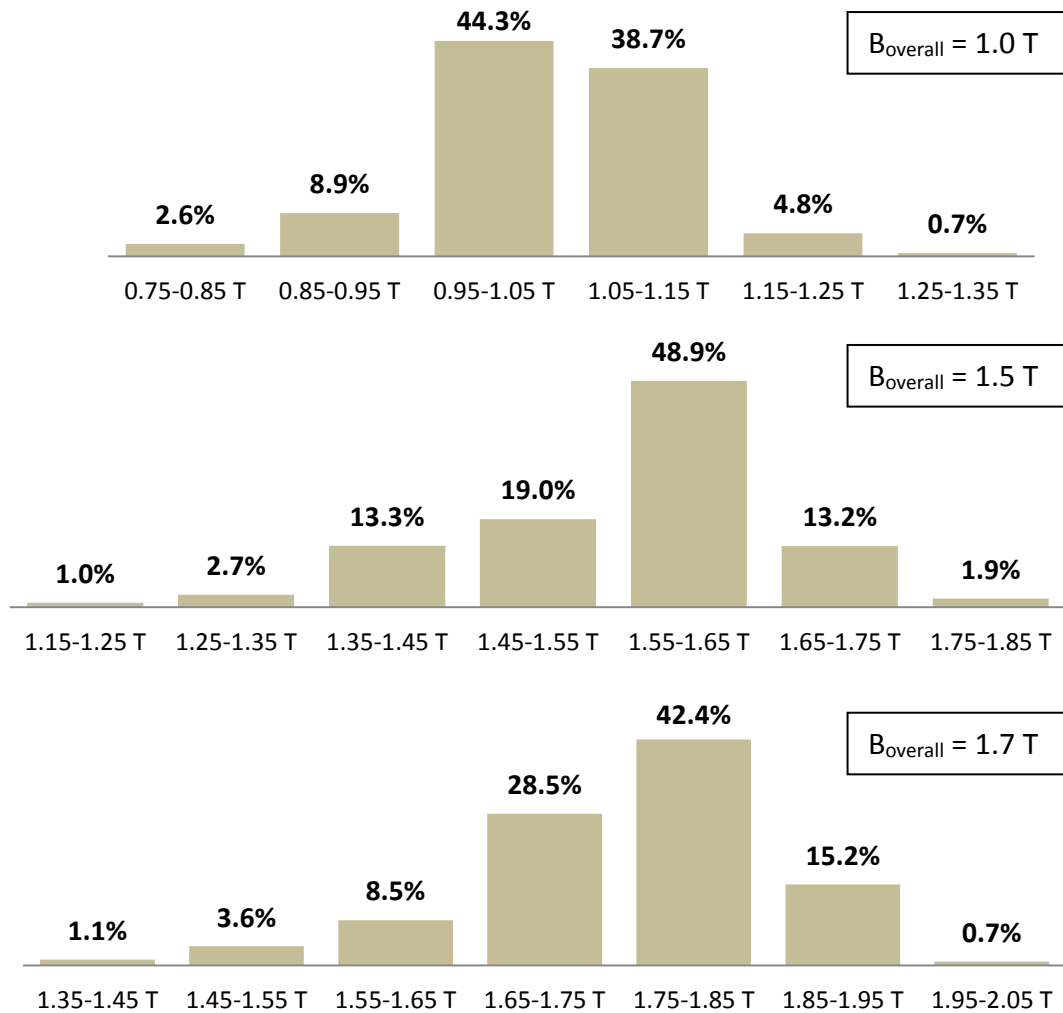
Figure 8.14 Bar charts showing percentage surface area of steel of flux density range.

8.7 Effect of grain misorientation on variation of localised magnetic flux density, magnetising field and power loss on grain oriented electrical steels.

In this part of the investigation, localised magnetic flux density, magnetising field and power loss of a commercial HiB specimen (H6) and a laboratory prepared poorly oriented specimen (P1) are obtained using the local loss measurement system. Results of the study of the effect of grain misorientation on the distribution of localised magnetic properties are compared.

8.7.1 Localised magnetic flux density, magnetising field and power loss measurements

Specimen H6 and P1 were decoated and annealed prior to the experiment. H6 is a commercial HiB steel with average grain misorientation of 3° and P1 is a laboratory prepared poorly oriented steel with average grain misorientation of 18°.

The specimens were magnetised individually using the local loss measurement system at sinusoidal flux density magnetisation of 50 Hz and peak flux density of 1.10 T. A higher value of flux density would have been applied, but the poorly oriented P1 could not be magnetised sinusoidally within the set THD of 1.5 %. A 60 mm (RD) x 16 mm (TD) area in the centre of each strip shown in figure 8.15 and 8.17 was raster scanned using the local loss sensor at 2 mm sampling intervals. This corresponds to a total sampling point of 279 in the scanning area. After the measurements were completed, the sensor was rotated by 90° and the experiment was repeated over the same area so that TD component of magnetic properties can be measured. Next, the specimens were turned over and the experiment was repeated over an identical area of the other surface of each specimen.

Figure 8.16 and 8.18 show the distributions of localised resultant flux density, magnetising field and power loss obtained using the local loss sensor at sinusoidal

magnetisation of 50 Hz and overall peak flux density of 1.10 T measured in H6 and
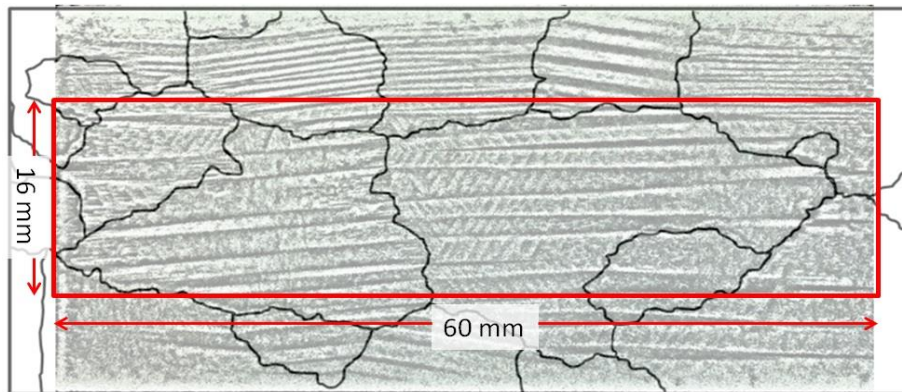
P1 respectively.

Figure 8.15 Grain boundary outlines superimposed on Bitter domain pattern showing the scanning area on H6.
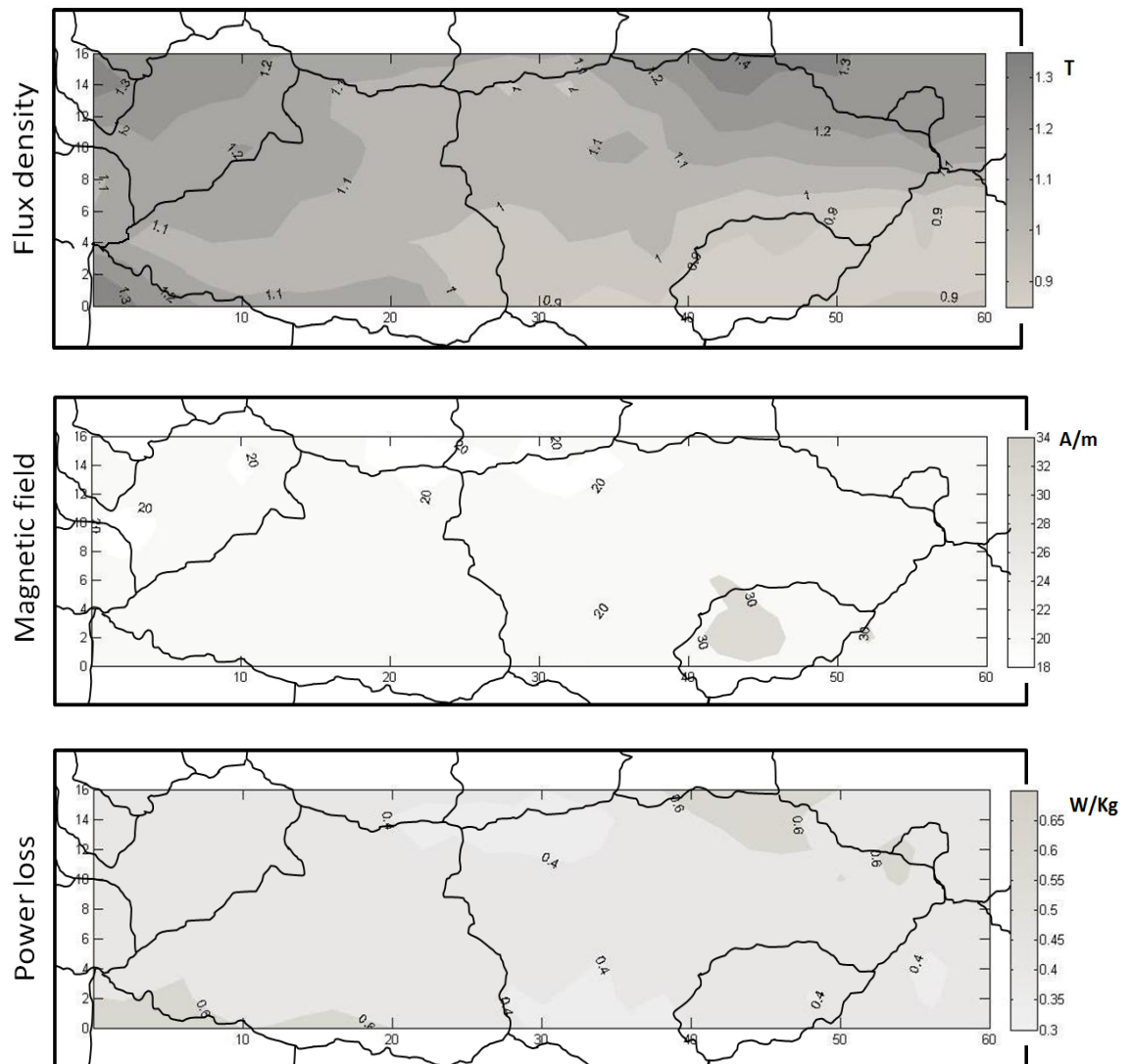

Figure 8.16 Distribution of peak resultant flux density, magnetising field and power loss at sinusoidal magnetisation of 50 Hz and overall peak flux density of 1.10 T over the same region of H6 shown in the box in figure 8.15, and grain boundary outlines are superimposed on each contour map.
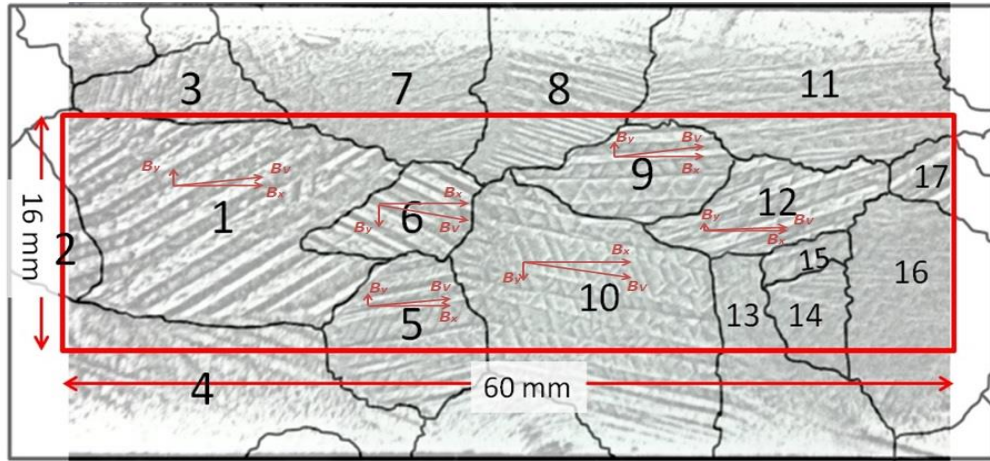
Figure 8.17 Grain boundary outlines superimposed on Bitter domain pattern showing the scanning area on P1.
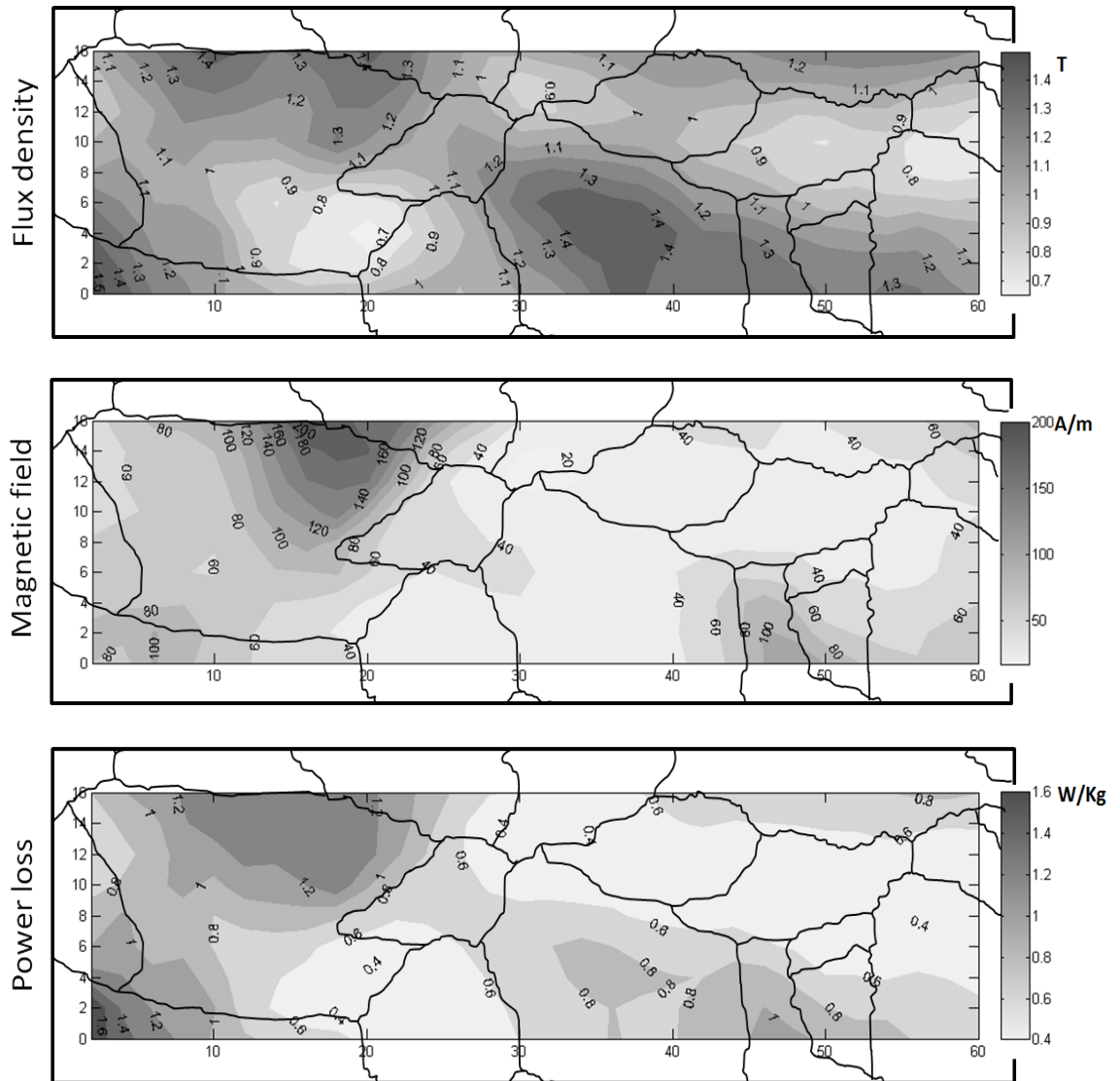

Figure 8.18 Distribution of peak resultant flux density, magnetising field and power loss at sinusoidal magnetisation of 50 Hz and overall peak flux density of 1.10 T over the same region of P1 shown in the box in figure 8.17, and grain boundary outlines are superimposed on each contour map.

Table 8.5 shows average of localised flux density, magnetising field and power loss derived from localised measurements of 279 sampling points in H6 and P1, and table 8.6 shows their corresponding standard deviations.

Specimen code	Average localised B	Average localised H	Average localised P
H6	1.09 T	23 Am^{-1}	0.48 WKg^{-1}
P1	1.12 T	58 Am^{-1}	0.81 WKg^{-1}

Table 8.5 Average of localised resultant magnetic flux density, magnetising field and power loss.

Specimen code	Standard deviation of localised B measurements	Standard deviation of localised H measurements	Standard deviation of localised P measurements
H6	8.2 %	410 %	4.8 %
P1	19.0 %	3500 %	27.9 %

Table 8.6 Standard deviation of localised magnetic properties.

Table 8.7 shows yaw angle of grains shown in figure 8.17 obtained by measuring the deviation angle of the 180° bar domains from RD of the specimen using a protractor, and average B_x (RD) and B_y (TD) of corresponding grains and B vectors and vector angles derived from both B_x and B_y components. The correlation between yaw angles and B vector angles are not obviously seen at most of grains, this is mainly because the combination of 7 mm needle separation and 2 mm scanning resolution are not sufficient to verify the relationship between yaw angles and B vector angles in HGO steel. It is believed that an improved correlation should be obtained if a shorter needle span and increased scanning resolution was used, which should be considered for the future work.

Grain No.	Yaw angle °	Average Bx (T)	Average By (T)	B vector (T)	B vector angle °
1	31.00	1.08	0.15	1.09	7.83
5	16.50	0.97	0.14	0.98	8.54
6	31.50	1.08	0.27	1.11	14.55
8	16.50	1.01	0.28	1.05	16.51
9	2.50	1.05	0.14	1.05	7.55
10	12.00	1.30	0.21	1.32	9.40
11	8.50	1.24	0.06	1.24	2.74
12	16.50	0.92	0.07	0.93	4.29
13	6.50	1.31	0.21	1.32	9.29
14	4.50	1.22	0.17	1.23	8.04
15	15.00	0.95	0.09	0.95	5.44
16	6.50	1.04	0.15	1.05	8.53
17	36.00	0.92	0.10	0.93	6.13

Table 8.7 Yaw angles and B vector angles of grains shown in figure 8.17.

The resultant magnetic flux density, magnetising field and power loss contour maps shown in figure 8.16 and 8.18 show that all the measured localised magnetic properties in the poorly oriented P1 exhibit wider distribution range compare to that of H6. At overall peak flux density of 1.10 T, the localised resultant magnetic properties in P1 varies from 0.65 to 1.55 T, 20 to 200 A/m and 0.4 to 1.6 W/Kg, and in H6 varies from 0.75 to 1.35 T, 18 to 34 A/m and 0.3 to 0.7 W/Kg. In addition, substantial increase in standard deviation of localised magnetic properties measurements were calculated for P1 compared to H6 shown in table 8.6. The results show that the degree of variation of localised flux density, magnetising field and power loss increases with increasing average of grain misorientation angle.

It is considered that flux distributes itself in a such way to reduce overall energy of the system. In H6, flux tends to distribute along RD as result of minimisation of magnetostatic energy as discussed in 8.6. In P1, flux tends to distribute more according to the grain outlines compared to that of H6. Grains with easy axes closer to the RD or direction of the field are easier magnetised than deviated grains as described by magnetocrystalline anisotropy energy outlined in chapter 2. As a result, grains with small yaw angle should exhibit higher flux densities than those with larger yaw angle. The relationship between average resultant flux density measured within individual grains of P1 and the yaw angles of

the individual grains is shown in figure 8.19. The trend line shows that the average resultant flux density in individual grains decreases with increasing yaw angle. The relationship between average flux density and yaw angle was not obvious as the calculated correlation coefficient for the trend line was -0.26. This is because that the distribution of flux density is not only influenced by grain orientation but also the local grain arrangement. At the bottom right corner of grain 1, where grain boundary is shared with grain 4, 5 and 6 shown in figure 8.17, the lowest flux density was measured compared to the other area shown in figure 8.18. This is considered due to an enhanced effect of large yaw angle and mismatched grain arrangement. A detailed study is presented in 8.7.2, where the DC domain wall movement in grain 1 was observed while investigating the large variation of flux density within the grain.
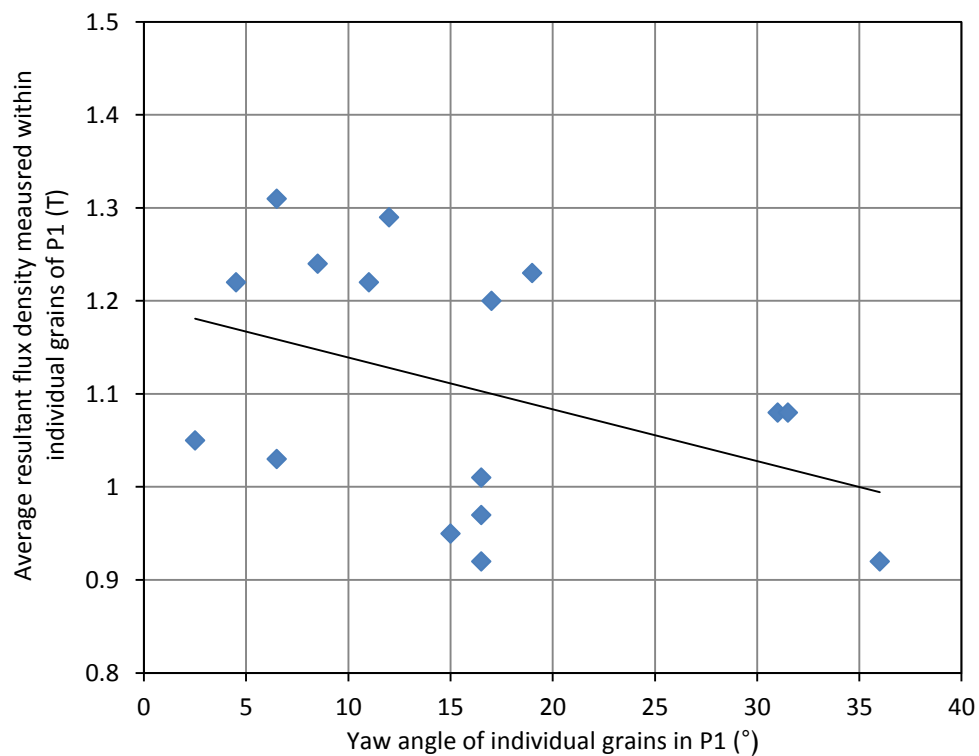

Figure 8.19 Relationship between localised resultant flux density measured within grains of P1 and yaw angles of the grains.

The variation of localised magnetising field can be explained by the existence of the localised demagnetising field. The result of domain observation presented in 8.3 shows that creation of flux closure domains did not occur at grain boundary of

discontinued 180° domains, which indicates that there is a demagnetising field as a result of exposure of free magnetic pole at grain boundaries. In H6, the 180° domain walls mostly move simultaneously in adjacent grains as indicated by the elongated distribution pattern as discussed in 8.6. Consequently, this lead to a lower demagnetising field at grain boundaries, thus the surface magnetising field measured on H6 varies considerably less than that on P1. In P1, flux distributes more according to grain outlines, which means that the correlation of 180° domain wall movements in adjacent grains is not as close as that in H6 as a result of the increased grain misorientation and grain mismatch angle. This increases the localised demagnetising field, which in combination with the higher field strength needed for excitation P1 to the same induction level than that for H6 (indicated by the average of localised magnetising field shown in table 8.5), causes the higher degree of variation of localised magnetising field.

Comparison of flux density, magnetising field and power loss distribution patterns shown in figure 8.16 and 8.18 indicates that the localised loss distribution is influenced by both flux density and magnetising field. The average of localised power loss of 0.48 and 0.81 W/Kg is calculated for H6 and P1 respectively shown in table 8.5. The high loss value measured in P1 is believed mainly due to the great average resultant localised flux density and magnetising field and larger degree of their variations occur in the poorly oriented specimen.

Figure 8.20a and 8.20b show the distribution of the TD component of flux density measured over the same area shown in the boxed areas in figure 8.15 and 8.17 respectively. Obviously, the TD component of flux density in P1 shows greater magnitude and higher level of variation than that in H6. The average of the localised TD component of flux density of P1 is more than double that of H6 shown in table 8.8, and the corresponding standard deviation reveals that the degree of variation of the TD component of flux density in P1 is almost twice as high as that in H6. The results confirm that there is definite correlation between the TD component of flux density and the average grain misorientation.

Figure 8.21 shows the relationship between the average TD component of flux density measured within individual grains of P1 and the yaw angles of the individual grains. Despite the large scattered data, which is believed to be caused by the local variation of the resultant flux density, the average TD component of flux density in individually grains increases with increasing yaw angle as indicated by the best-fit trend line. This confirms that the TD component of flux density is mainly a result of change in y component of flux density due to movement of the 180° domain walls parallel to the [100] directions of individual grains.
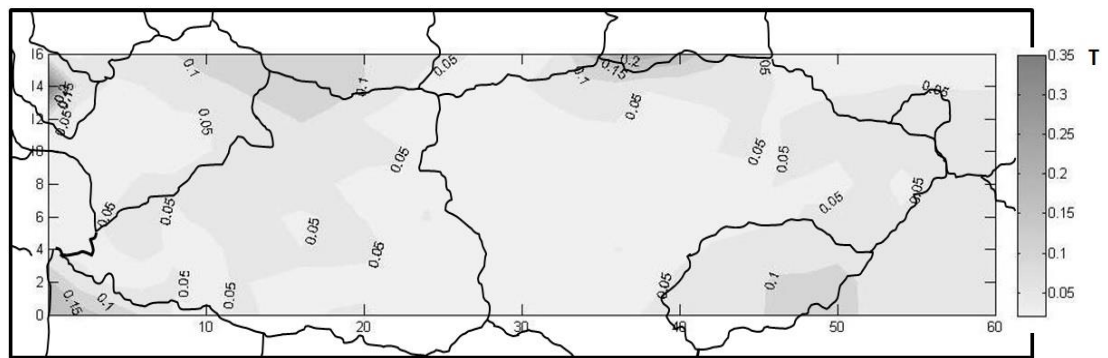
(a) H6
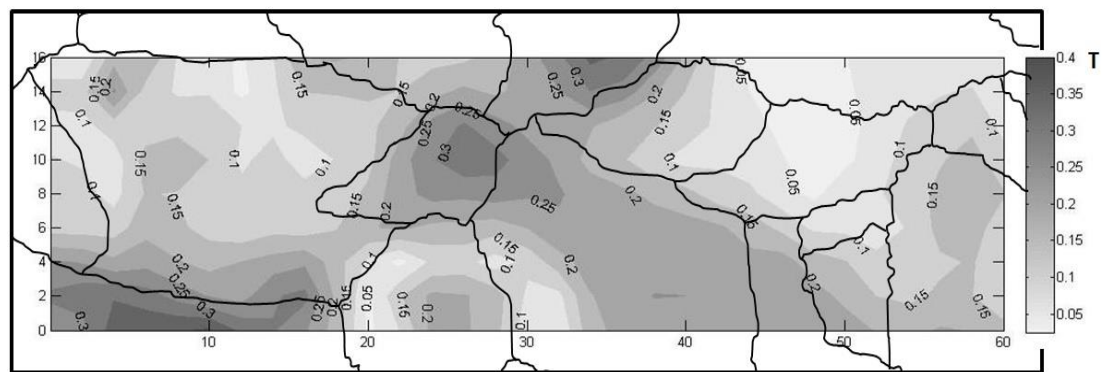
(b) P1

Figure 8.20 Distribution of peak TD component of flux density at sinusoidal magnetisation of 50 Hz and overall peak flux density of 1.10 T, and grain boundary outlines are superimposed on each contour map.

Specimen code	Average localised TD component of flux density	Standard deviation
H6	0.06 T	4.5 %
P1	0.16 T	8.0 %

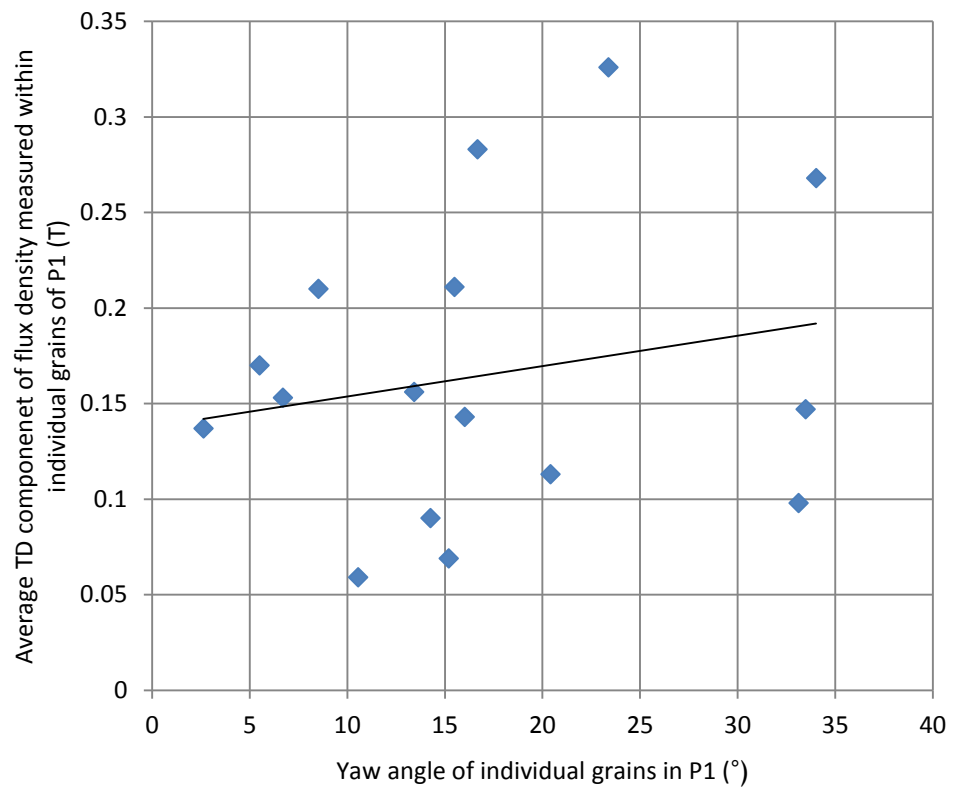**Table 8.8** Average localised TD component of flux density and standard deviation.

Figure 8.21 Relationship between localised TD component of flux density measured within grains of P1 and yaw angles of the grains.

8.7.2 Correlation between domain wall movement and local variation of flux density

In this part of the investigation, an attempt to observe domain wall motion of the grain showing large in-grain variation of flux density was made to see if a correlation between the domain wall motion and localised flux density distribution exists in grain oriented steel.

A 30 x 30 mm area covering grain 1 of P1, whose grain outlines and static domain pattern and distribution of localised resultant flux density is shown in figure 8.17 and 8.18 respectively, was selected for this part of the investigation. A incremented DC field was applied along RD direction of the strip and the change in domain wall positions in this area was observed using the domain viewer. To magnetise the Epstein strip, a single yoke which has a pole separation distance of 290 mm and an enwrapping 140 turns current carrying coil was used. During the experiment, the domain pattern in the incremented DC field, whose corresponding field strength is shown in table 8.9, was captured as shown in figure 8.22. The sequence of domain images simulates domain wall movement under AC magnetisation.

Table 8.9 shows the corresponding magnetising field applied to the specimen while an input DC current is flowing in the coil. This is calculated from

$$H = \frac{NI}{l_s}$$

where N is number of turns of the coil on the yoke, I is the coil current, and l_s is the mean free path of the specimen. In this case the mean free path is approximately equal to the pole separation distance of the yoke. The corresponding flux density values shown in table 8.9 are flux densities induced in the specimen while the 50 Hz sinusoidal magnetising field was applied.

Input current (A)	Magnetising field (A/m)	Magnetic flux density (T)
0.00	0	0.00
0.05	24	0.70
0.10	48	1.05
0.15	72	1.24
0.20	96	1.31
0.25	120	1.35

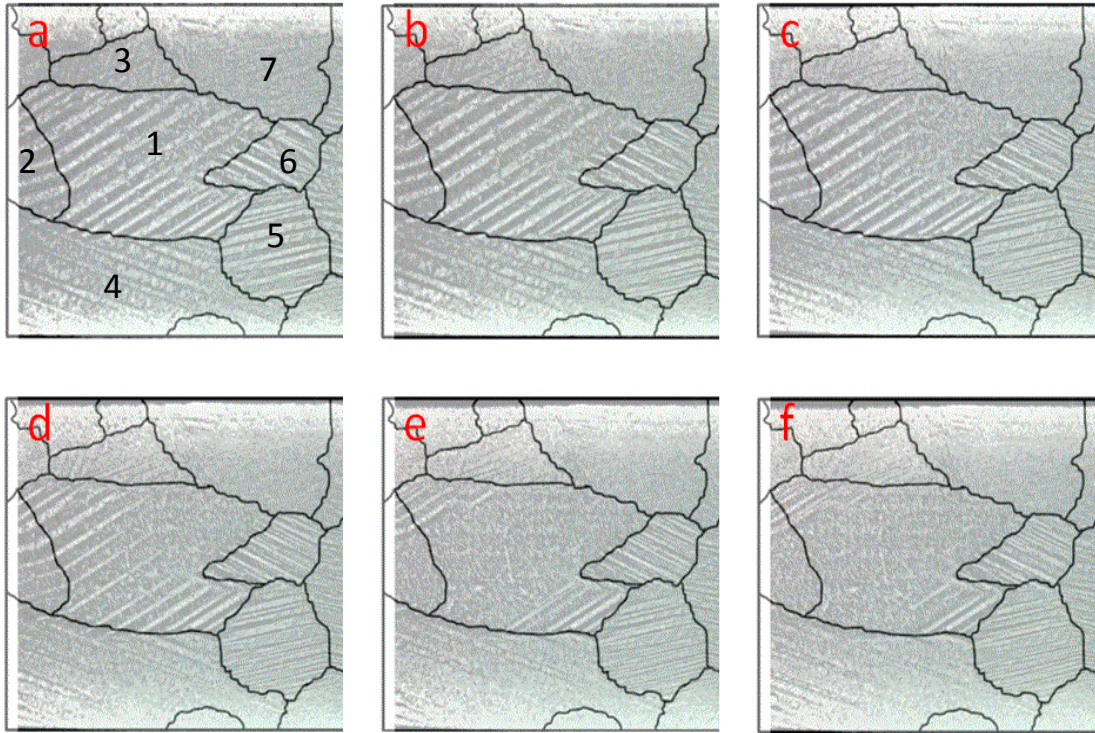**Table 8.9** The corresponding magnetising field and flux density at the input currents.

Figure 8.22 Static domain patterns obtained using the domain viewer showing domain wall position in an incremented DC field, and the area of view is 30 mm x 30 mm covering grain 1 of P1. (a) 0.00 T, (b) 0.70 T, (c) 1.05 T, (d) 1.24 T, (e) 1.31 T and (f) 1.35 T. The direction of RD and DC field is along the horizontal axis.

The sequence of DC domain patterns shown in figure 8.22 simulates domain wall movement in an increasing magnetising field from 0 to 120 A/m or 0 to 1.35 T. Domains within grain 1 respond differently to the external field. At lower fields (see figure 8.22 b and c), domains in the top right corner start to reconfigure by growing black domains whose RD components of magnetisation are aligned in the field direction, and domains in the rest of the area in grain 1 remain almost unchanged. On further increase of field (see figure 8.22 d), domains that are in connection with grain 2 and 3 start to reconfigure. At higher fields (see figure 8.22 e and f), only a

small fraction of domains at the bottom right corner remains unchanged while the rest of the area in grain 1 are being magnetised as a single black domain. Comparing the DC domain patterns presented in figure 8.22 and distribution of localised resultant flux density shown in figure 8.18. It is found that the area showing early domain reconfiguration exhibit higher flux density compared to other areas, and the area showing the least domain reconfiguration throughout the magnetisation process exhibits the lowest flux density. This result shows that there is strong correlation between characteristic of domain wall movement and distribution of localised flux density.

The large in-grain variation of flux density found in grain 1 is believed to be influenced by local grain arrangement and grain geometry. When an external magnetising field is applied in the RD direction of the specimen, it can be assumed that 180° domain walls in relatively less deviated grains are more mobile than those in largely deviated grains, thus domain walls in the surrounding grains 2 to 7 are expected respond differently in the applied external field. In the vicinity of the grain boundary between grain 1 and 2, assume domain walls in the relatively less deviated grain 2 moves first under the applied field, then free magnetic poles are exposed at the boundary, which increases the magnetostatic energy. The rise of magnetostatic energy is then lowered by moving the corresponding domain walls in grain 1 to match with walls in grain 2. In this case, the higher flux density measured within grain 1 in the vicinity of the grain boundary is mainly due to the interaction of domain walls of the adjacent grains. At the bottom right corner of the grain 1, where the least domain wall movement are observed, wall migration is less energetically favourable in this area as it can lead to significant increase in magnetostatic energy due to large grain mismatch angles. In addition, due to the grain geometry, demagnetising field factor at both top left corner and bottom right corner is higher compared to the middle section of the grain. This should also lead walls at corners move less active than in the middle of the large grain as observed in figure 8.22.

8.8 Effect of domain refinement on distribution of local magnetic flux density of HiB electrical steel.

Domain refinement is an important method for reducing power loss of HiB electrical steels. In this part of investigation, localised flux density of a HiB specimen before and after domain refinement was measured using the local loss measurement system to study the effect of domain refinement on the distribution of localised magnetic flux density.

Specimen H7 was decoated and annealed prior to the experiment. Domain wall spacing of the specimen was then refined by means of ball scribing using a weighted ballpoint pen at 90º to the RD on one surface of the specimen. The ball scribing was carried out at intervals of 12 mm, 6 mm and 3 mm respectively. Magnetic domain patterns before and after ball scribing were inspected using the domain viewer and as shown in figure 8.23, the average domain wall spacing shown in table 8.10 was derived from,

$$\text{Average of wall spacing} = \frac{\text{width of the speicmen x 3}}{\text{Number of domains counted in three columns}} \text{ (mm)}$$

The overall power loss and average of AC relative permeability of the specimen before and after ball scribing were measured using a single strip tester at sinusoidal magnetisation of 50 Hz and a range of peak flux density from 1.00 T to 1.70 T. Results are shown in figure 8.24 and 8.25 respectively. The localised RD component of flux density before and after ball scribing was measured using the local loss measurement system at sinusoidal flux density magnetisation of 50 Hz and peak flux density of 1.70 T. To avoid the influence of high surface leakage field produced by free magnetic poles at the scribed grooves on the accuracy of NP, the scribed surface of the specimen faced downwards and the localised peak RD component of flux density in a 60 mm (RD) x 20 mm (TD) area in the centre of the strip and on the other surface was raster scanned using the NP at 2 mm sampling intervals.
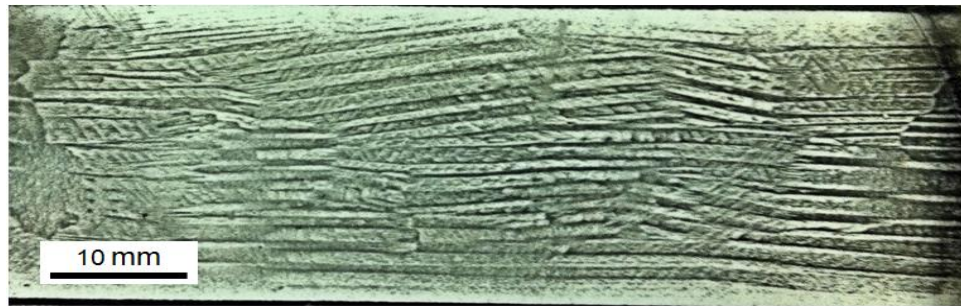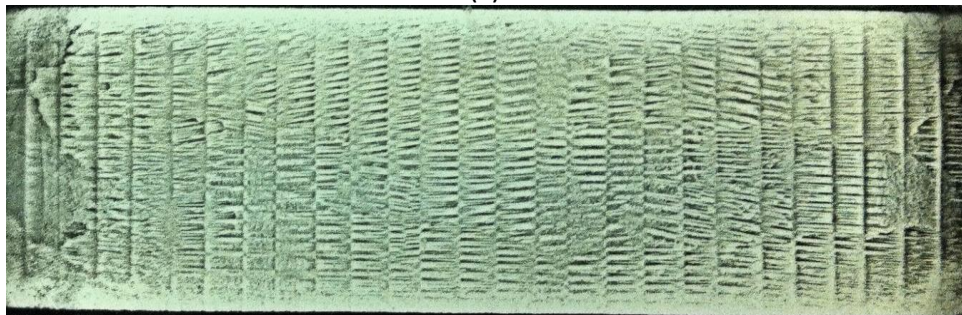
(a)
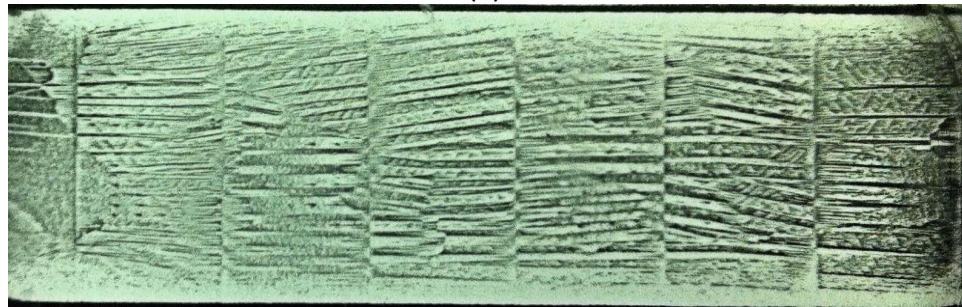
(b)
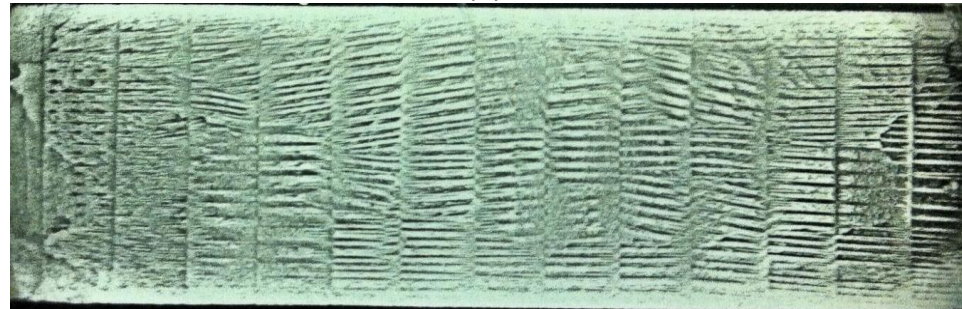
(c)

(d)

Figure 8.23 Magnetic domain patterns obtained using the domain viewer over the centre area of H7

(a) Unscribed, (b) 12 mm scribed, (c) 6 mm scribed and (d) 3 mm scribed.

Scribe spacing (mm)	Average domain wall spacing (mm)
Un-scribed	0.96
12	0.85
6	0.55
3	0.36

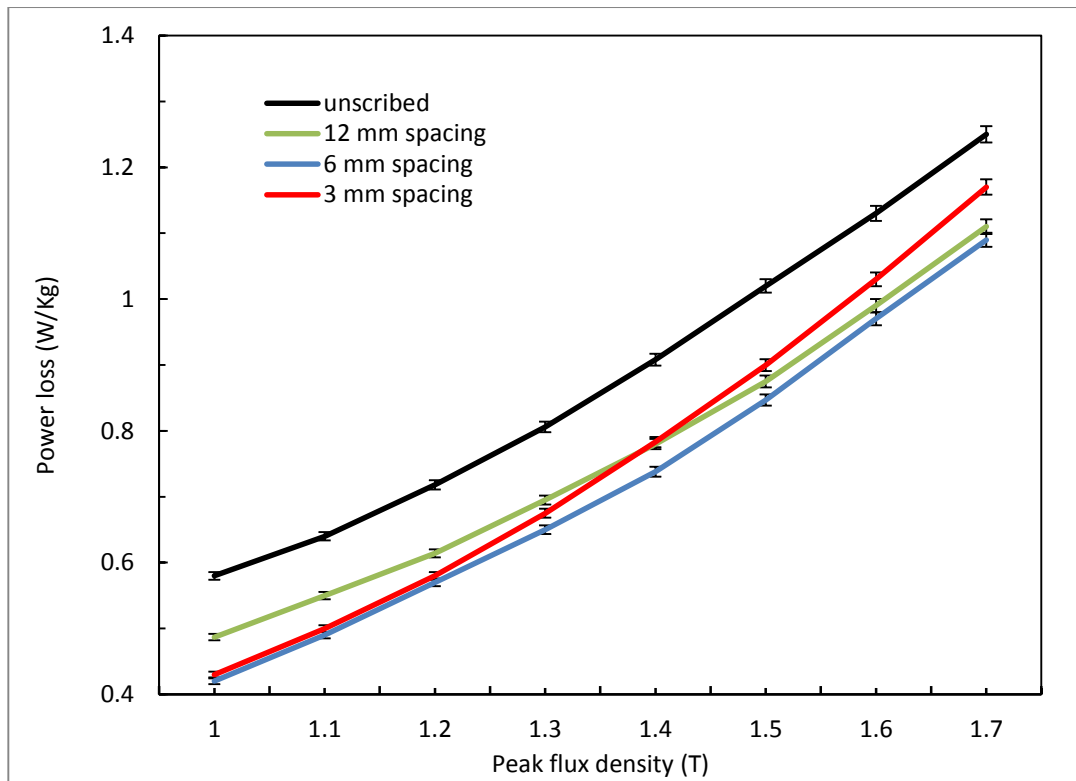**Table 8.10** Average domain wall spacing.

Figure 8.24 Relationship between power loss and flux density.
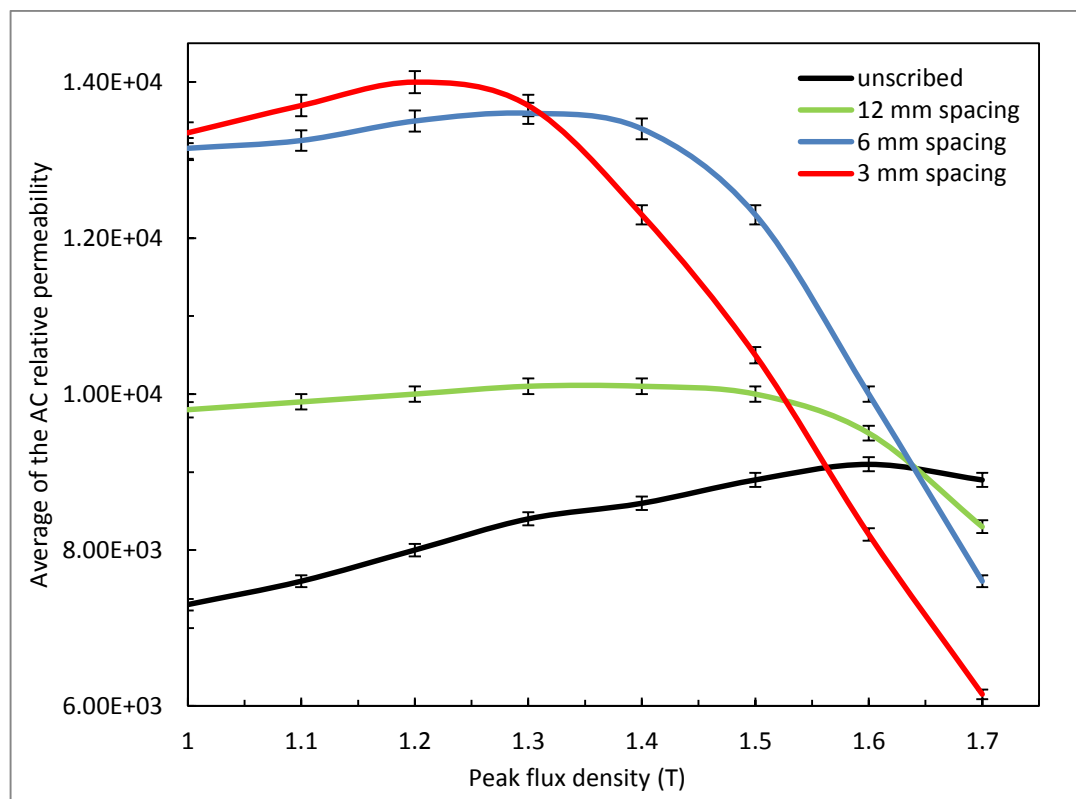

Figure 8.25 Relationship between average of the AC relative permeability and flux density.

Figure 8.24 shows the relationship between overall power loss and peak flux density for the specimen before scribing, and after scribing at 12 mm, 6 mm and 3 mm spacing respectively obtained using the single strip tester. It is seen that the specimen after scribing exhibit reduced power loss compared to that of before domain scribing, the highest loss reduction over the entire studied flux density range of 1.00 to 1.70 T is found at 6 mm spacing. At peak flux density below 1.20 T, the loss curves of the 6 mm and 3 mm spacing show similar trends and loss values, but at peak flux densities above 1.20 T, the slope of the 3 mm curve exhibits sharper increase than that of other curves. Above 1.4 T, the 3 mm curve overtakes 12 mm curve and the loss of the 3 mm spacing becomes the highest of all scribing spacing.

Figure 8.25 shows the relationship between the average of the AC relative permeability and the peak flux density for the specimen before scribing and after scribing at 12 mm, 6 mm and 3 mm spacing respectively obtained using the single strip tester. All curves exhibit similar trends, the average of the AC relative permeability increases with increasing flux density, then decreases at higher flux density, but the change in trend occurs at different peak flux density values. The change in trend occurs at a lower peak flux density in the specimen after scribing than before scribing. At lower flux densities (< 1.20 T), the averages of the AC relative permeability of the specimen after domain scribing is higher than that before scribing, and increases with decreasing scribing spacing. At higher flux densities (>1.65 T), the averages of the AC relative permeability of the specimen after scribing is lower than before scribing, and decreases with decreasing scribing spacing.

Domain refinement by means of ball scribing reduces AC power loss of electrical steel as a result of decreasing the eddy current loss due to decreasing the mean free path of domain walls as shown in table 8.10. However, the method of domain scribing introduces residual stresses which act as domain wall pinning and increases hysteresis loss. At lower flux density, domain walls propagate shorter distance hence encounter fewer pinning sites. At higher flux density, domain walls propagate longer distance and have to encounter more pinning sites leading to

increased hysteresis loss and decreased permeability compared to that at lower flux density. Excessive scribing in a confined area (i.e. domain scribing at 3 mm spacing) leads to reasonable decrease of eddy current loss but substantially increase in hysteresis loss. Therefore, the optimum loss reduction is found to be at the moderate 6 mm spacing.

Figure 8.26 shows the distribution of the RD component of flux density of specimen H7 before and after scribing obtained using NP on one surface of the specimen. Comparison of the contour maps indicates that there is an obvious change in flux distribution. No correlation is found between scribing line positions and flux distribution. The specimen after scribing shows a narrower flux density distribution range as indicated by the percentage area of steel of flux density range shown in figure 8.27. The standard deviation of the localised flux density measurements decreases with decreasing scribing spacing as shown in table 8.11. The results indicate that domain scribing improves the uniformity of flux density distribution.
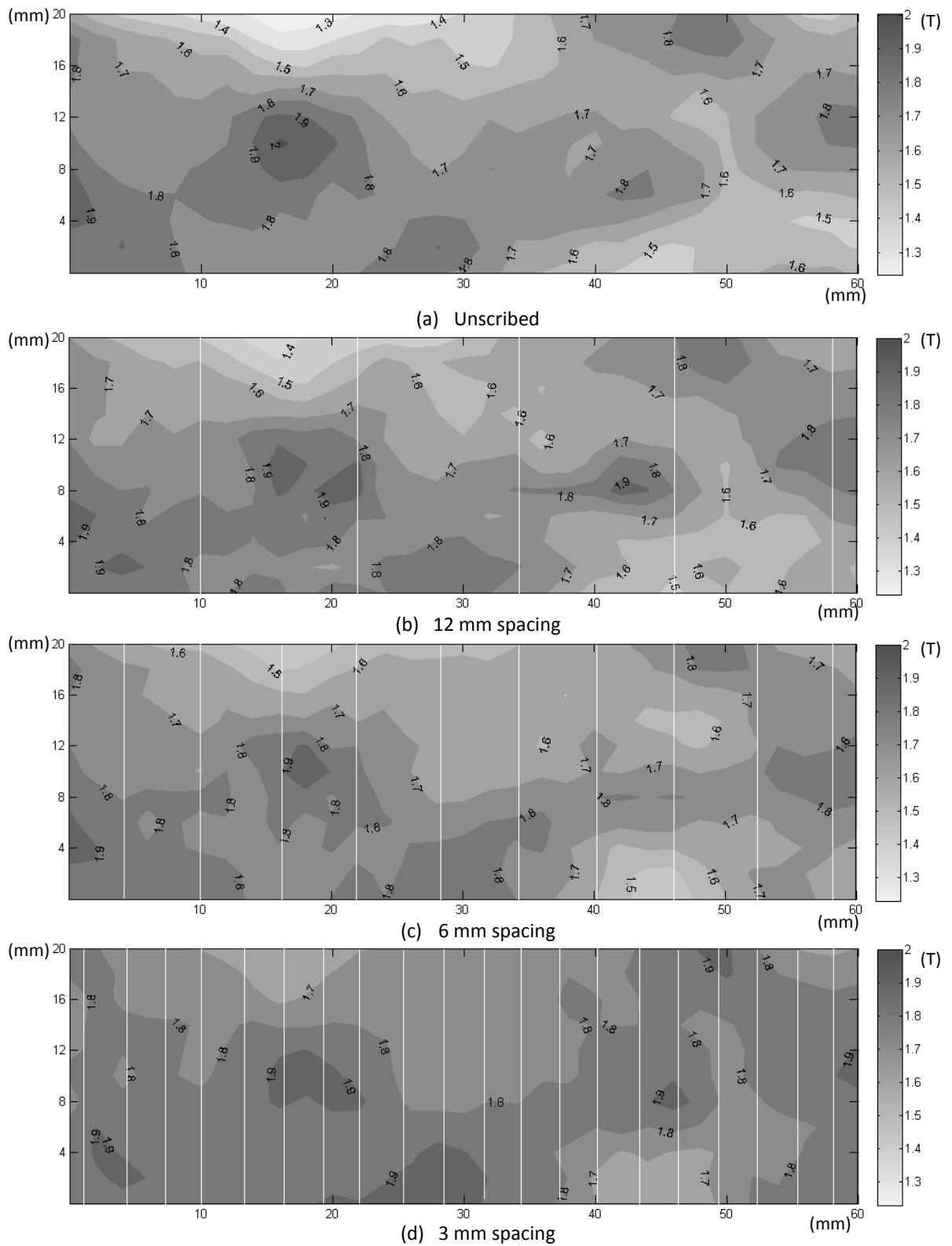
Figure 8.26 Distribution of peak RD component of flux density obtained using NP at sinusoidal magnetisation of 50 Hz and overall peak flux density of 1.7 T over 60 mm x 20 mm area on the other surface which is opposite to the scribing surface of H7, and scribe line positions are shown by the white lines.
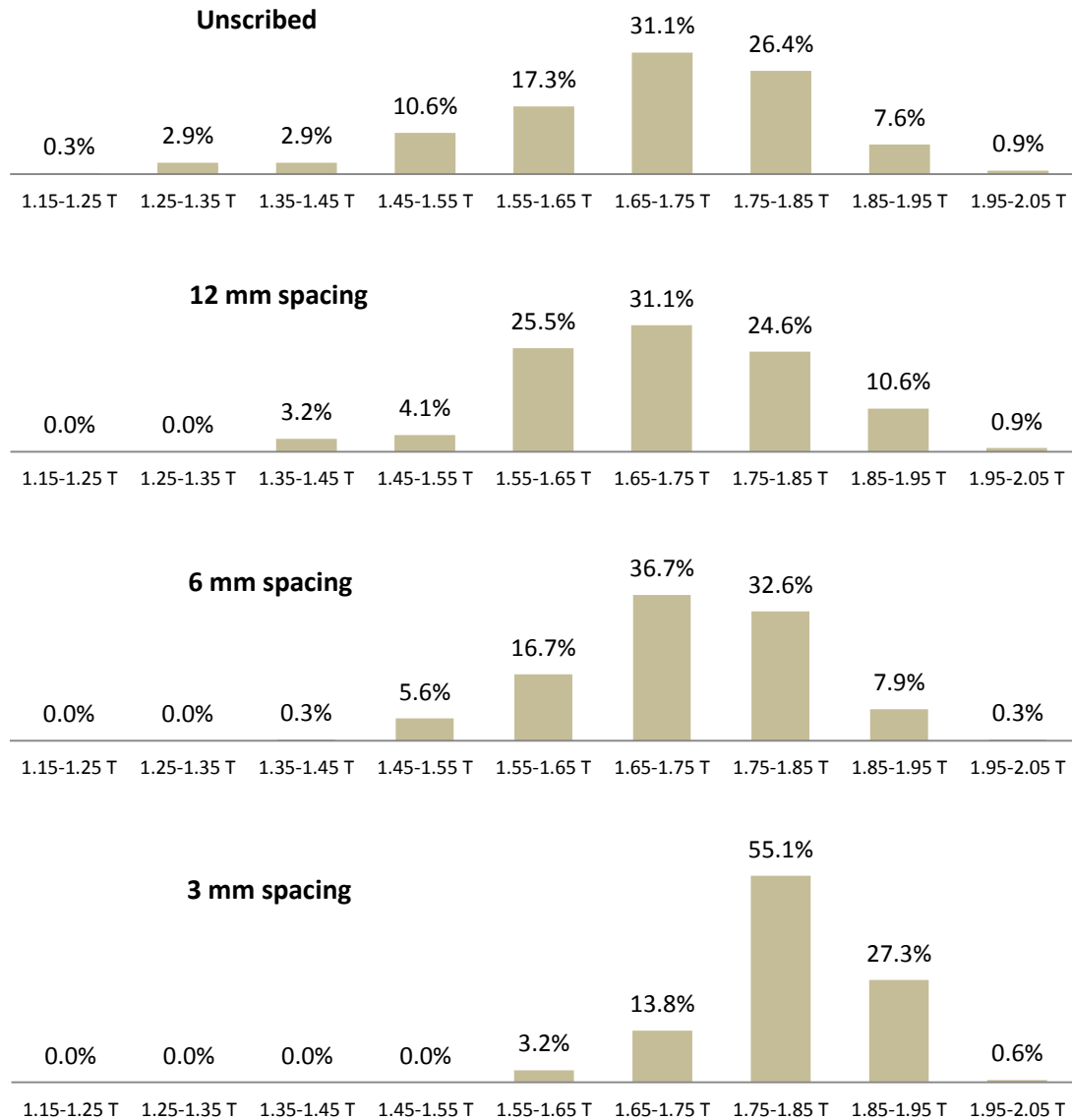
Figure 8.27 Bar charts showing percentage area of steel of flux density range.

	Unscribed	12 mm spacing	6 mm spacing	3 mm spacing
Average of localised B	1.68 T	1.71 T	1.72 T	1.81 T
Standard deviation of localised B	14 %	12 %	10 %	7 %

Table 8.11 Average and standard deviation of local flux density measurements.

A substantial increase in the average localised flux density is found in the specimen after scribing at 3 mm spacing shown in table 8.11. At peak overall flux density of 1.70 T, the average localised flux density measurements derived from 341 localised sampling points is 1.81 T, which correspond to a difference of 6.5 %. Such a large difference between overall flux density and averaged localised flux density is not found for the other scribing spacing as studied here. It should be noted that in this part of the investigation, localised flux density results were obtained from single surface NP measurements, the average difference between NP measurements obtained on a single surface and the average of both surfaces of HiB steel is estimated to be less than 1.9 % (see in 8.4). Even taking into account the 1.9 % difference, the difference of 6.5 % is still considerably high compared to the 2.4 % measured on the other HiB specimen at the same overall peak flux density as outlined in 8.6. This difference is assumed to be caused by non-uniform distribution of flux density in the thickness direction of the specimen due to non-uniform distribution of applied stresses as a result of scribing with the weighted ballpoint pen.

Figure 8.28 shows a simple illustration of the stress profile of the after scribed specimen based on the results obtained by Fukawa [8.3]. It can be seen that compressive stress is distributed mainly around the scribe traces as indicated by C_1 zone and below C_1 zone on the other side as indicated by C_2 zone; tensile stress as indicated by T zone is distributed mainly to the remaining volume of the material. It can be assumed that 180° domain walls in tensile zone are more mobile than those in compressive zones, because when grain oriented steel is subjected to tensile stress the increase of 180° domains at expense of the surface 90° domains becomes energetically favourable due to shift of the magnetic easy axis towards the direction of applied stress [8.4], while subjected to compressive stress the decrease of 180° domains at growth of the surface 90° domains becomes energetically favourable. Therefore, steel under tensile stress are easier magnetised that under compressive stress since magnetisation in the presence of an AC field applied parallel to the RD is mainly by 180° wall motion parallel to the easy direction.

Excessive scribing in a confined area leads to increased stress polarisation in the direction of the specimen's thickness as shown in figure 8.28b, which increases the differences in flux density induced in either side of the steel.
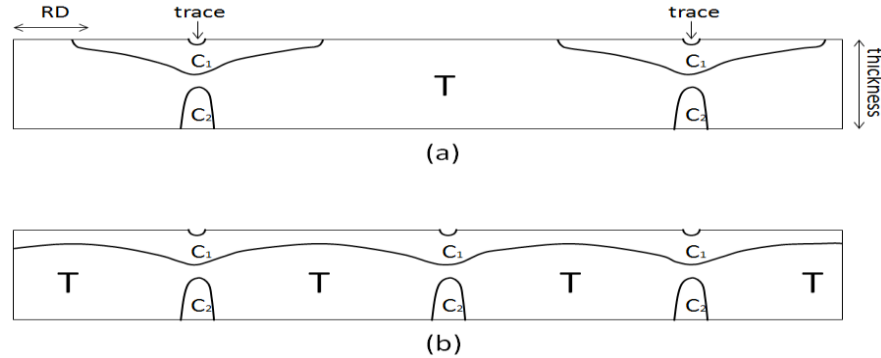

Figure 8.28 Illustration of stress distribution in domain scribed specimen.

To verify the proposed theory, the specimen after scribing at 3 mm spacing was turned over and localised peak RD component of flux density in the 60 mm x 20 mm identical area on the scribed surface was raster scanned using the local loss measurement system at the same overall magnetisation of 50 Hz and peak overall flux density of 1.70 T. The distribution of flux density obtained using the NP in the scribing side and non-scribing side of the specimen scribed at 3 mm spacing are compared in figure 8.29. It can be seen that the flux densities obtained at identical area are relatively smaller using the scribing side compared to those using the non-scribing side. Localised flux density is found to vary in a range from 1.35 T to 1.75 T and from 1.65 T to 2.05 T using the scribing and non-scribing side respectively for the measurement, and the corresponding averaged localised flux density is 1.56 T and 1.81 T as shown in table 8.12. The results confirm that there is a large difference in flux density induced in either side of the specimen scribed at 3 mm spacing. This increases the degree of non-uniformity of distribution of localised flux density, which together with the increased hysteresis loss is considered to be the reasons for the higher loss found in the 3 mm spacing shown in figure 8.24.

Further research could be carried out by observing dynamic domain on both surfaces of the steel after scribing to improve understanding of the influence of applied stress on the dynamic domain configuration, and to look for any correlation

between characteristics of dynamic domain wall movement and localised flux density.
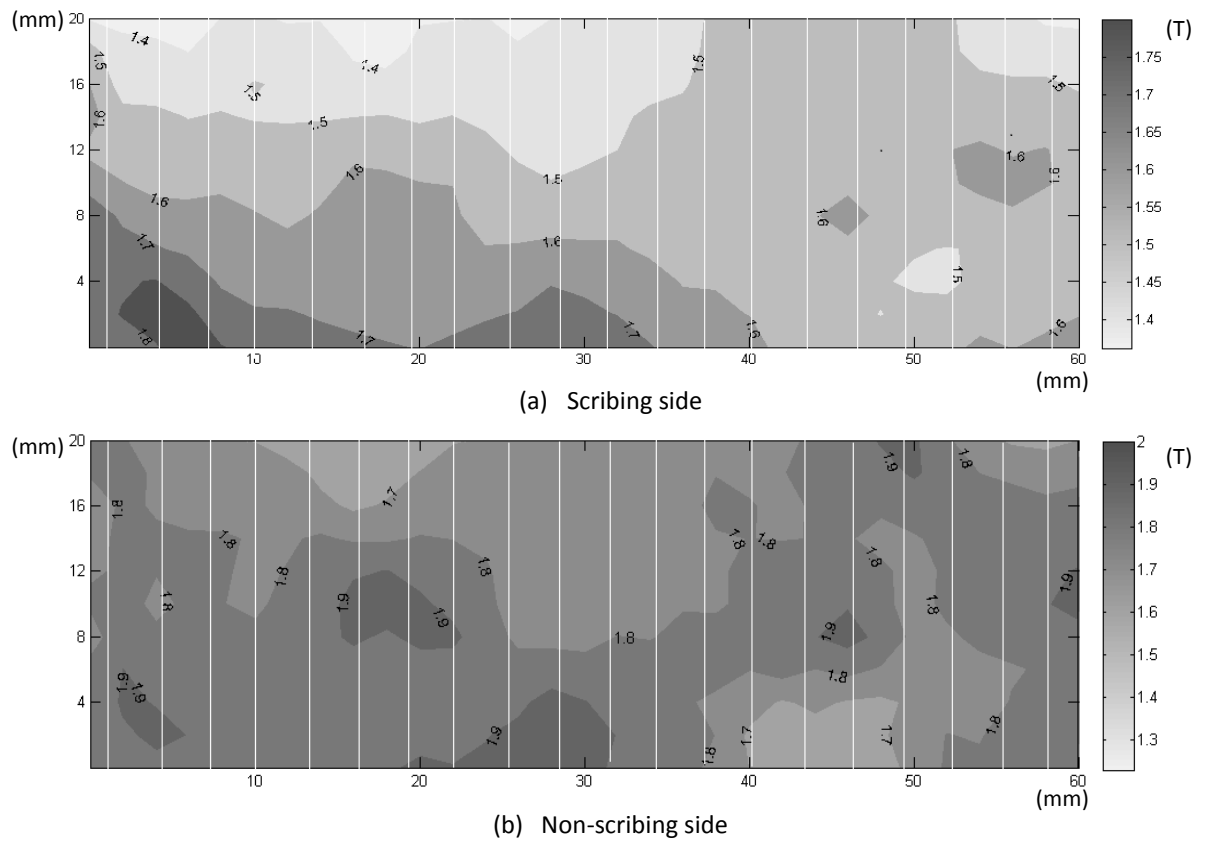

(a) Scribing side

(b) Non-scribing side

Figure 8.29 Distribution of peak localised RD component of flux density measured in identical area in both sides of the specimen scribed at 3 mm spacing.

	Scribing side	Non-scribing side
Average of local flux density	1.56 T	1.81 T

Table 8.12 Average of localised flux density.

References

[8.1]   X. Xu, A. Moses, J. Hall, P. William and K. Jenkins, "A comparison of magnetic domain images using a modified Bitter pattern technique and the Kerr method on grain-oriented electrical steel", IEEE Transactions on Magnetics, vol. 47, pp. 3531 – 3534, (2011).

[8.2]   G. Loisos and A. J. Moses, "Critical evaluation and limitations of localized flux density measurements in electrical steels", IEEE Transactions on Magnetics, vol. 37, pp. 2755 – 2757, (2001).

[8.3]   K. Fukawa and T. Yamamoto, "Domain structures and stress distribution due to ball-point scratching in 3% Si-Fe single crystals with orientation near (110)[001]", IEEE Transactions on Magnetics, vol. 18, pp. 963-969, (1982).

[8.4]   T. W. Krause, L. Clapham, A. Pattantyus and D. L. Atherton, "Investigation of the stress-dependent magnetic easy axis in steel using magnetic Barkhausen noise", Journal of Applied Physics, vol. 9, pp. 4242 – 4252, (1996).

Chapter 9

Conclusions

Both domain viewer and magneto-optical Kerr microscope can provide important information with regard to magnetic domain configuration and crystal orientation of grain oriented electrical steel. The domain viewer is found more sensitive to small angle grain boundary than the Kerr microscope. However, the image contrast cannot be relied upon to determine the absolute direction of domain magnetisation since it is an indirect domain observation method. The Kerr microscope is found more sensitive to domain magnetisation than the domain viewer, but the equally important small angle grain boundary was not observed using the Kerr microscope since the overall magnetisation continues across the boundary. This finding would be useful in providing accurate analysis on domain images obtained using any stray field sensitive method and the magnetisation polarisation method.

The real time dynamic domain patterns captured using the Kerr microscope showed that the 180° walls are not moving homogeneously and consistently at the vicinity of the grain boundary under AC magnetisation, which proves the existence of the local non-uniform magnetisation.

A local loss measurement sensor, which comprises a Needle Probe (NP) and Hall Effect sensor, was made for measurement of localised magnetic flux density, magnetising field and power loss of grain oriented electrical steel. The uncertainties

of flux density, magnetising field and power loss measurements are evaluated to be ± 0.22 %, ± 1.09 % and ± 1.76 % respectively. Flux density measured using NP and search coil respectively at identical positions on a high permeability grain oriented steel (HiB) were in good agreement, which gives a high degree of confidence in the localised flux density measurements.

Localised flux density of grain oriented electrical steel are found to vary greatly under AC magnetisation of 50 Hz. Increasing induction level or grain misorientation changes the characteristic of distribution of flux density. At a lower induction and grain misorientation, magnetostatic energy dominates flux distribution, flux tends to distribute along rolling direction of the specimen as in this way to minimise the magnetostatic energy. At a higher induction or grain misorientation, both magnetostatic and magnetocrystalline anisotropy energy dominate flux distribution, flux tends to distribute more according to grain outline compared to that at lower induction and grain misorientation, as a result, leading to increased degree of variation of flux density. A strong correlation between domain configuration and localised flux density distribution is found showing the main causes of the variation of flux density are due to the grain misorientation and the local grain arrangement. The transverse component of flux density is detected and is found increases with increasing grain misorientation.

The variation of localised magnetising field is found to be influenced by the localised demagnetising field that is generated by free magnetic poles at grain boundaries of the discontinued magnetisation.

Comparison of localised flux density, magnetising field and power loss distribution maps showed that the distribution of localised power loss is strongly influenced by both the localised flux density and magnetising field.

Domain refinement by means of ball scribing on one surface of HiB steel at 90° to the RD is found to influence the characteristic of flux density distribution. At 12 mm and 6 mm scribing spacing, result showed that the ball scribing can improve the uniformity of distribution of localised flux density and reduce the overall power

loss of the steel. At 3 mm scribing spacing, result inferred that the stress polarisation due to the ball scribing could lead to obvious uneven distribution of flux density in the direction of the specimen's thickness and increased power loss.

Future investigation

This investigation has indentified the need for future research in helping to improve the understanding of the causes of the non-uniform magnetisation:

- The future work would be to repeat the investigation on conventional grain oriented steel or different degree of misoriention steel to quantify the influence of misorientation on variation of localised magnetic properties of electrical steels.

- Dynamic domain observation at 50 Hz on both surfaces of the domain refined steel should be investigated to look for any correlation between the characteristic of domain wall movements and the differences in flux density induced in either side of the steel.